Comparative Study of Non-Tracking and Low Concentrating Photovoltaic Systems Using Low-cost Reflectors

By

Sylvester Hatwaambo

A thesis submitted to the University of Zambia in fulfillment of the requirement for the award of the Doctor of Philosophy in Physics of the University of Zambia.

The University of Zambia
2009

Declaration

I, the undersigned, hereby declare that the work presented in this thesis represents my own work and that it has not been submitted and not being currently submitted in part or whole for the award of a degree at any other University

Signature: .....Date: 28/07/2009

APPROVAL

This Thesis of SYLVESTER HATWAAMBO is approved as fulfilling the requirements for the award of the degree of DOCTOR OF PHILOSOPHY IN PHYSICS by the University of Zambia.

Name and Signature of Examiners Date

External Examiner

1. Name..Prof. Tom Otiti.....
   Signature..Tom Otiti..... 27/2/2009

Internal Examiners

2. Name..Bjorn Karlsol.....
   Signature..... 27/2/2009

3. Name..Prem Jain.....
   Signature..... 3/06/2009

4. Name..Prof E.A. Tyrm.....
   Signature..... 3/06/09

ABSTRACT

The traditional high concentrating photovoltaic systems have proved to be expensive as they use high grade silicon solar cells, highly specular reflecting materials and require tracking arrangements which are equally expensive. The problem of un-even illumination creates heat-sinks which have not been solved in high concentrating systems. This thesis addresses the problem of un-even illumination in low concentrating photovoltaic systems using low cost reflecting materials for low-cost electricity. The large module cells are replaced by small string modules and the highly specular materials are replaced with low-cost diffuse materials.

Concentrating sunlight onto a solar module has an effect of hot-spot formation which reduces the fill factor and hence the efficiency of the photovoltaic system. To address this problem, diffuse reflectors with rolling marks either parallel or perpendicular to the plane of the module were tested in low concentrating photovoltaic systems. The changes in the fill factor were monitored as different reflector materials were replaced within concentrator geometries.

It was experimentally shown that diffuse reflectors gave better fill-factor than specular reflectors. It was further demonstrated that diffuse reflectors with rolling grooves aligned parallel to the plane of the module gave better fill-factor than

diffuse reflectors with rolling grooves aligned perpendicular to the plane of the module surface. In particular, the power increased by a factor of 2 in all reflector materials studied but the drop in the fill factor was 28% for rolling marks parallel to the plane of the module as compared to 30% for rolling marks perpendicular to the plane of the module. The parallel rolling marks (horizontal grooves) gave improved fill factor. Probably the rolling marks scattered the solar flux within the concentrator geometry at large angles and hence evenly illuminated the solar cell module area. The vertical grooves on the other hand had low angle scattering of the solar flux and could not spread the solar flux along the plane of the module. The vertical orientation of the grooves had similar performance as specular reflectors. Furthermore, the performance of the CPC geometry with semi-diffuse aluminium foil was under estimated due to construction errors as compared with anodized aluminium which gave a better performance as it was used as the base material.

It was also verified that anodized aluminium, miro and rolled aluminium foil respectively, were the best reflector materials that withstood the environmental conditions. However, due to its low cost, the rolled aluminium foil was preferred for use in low concentrating photovoltaic systems.

ACKNOWLEDGEMENTS

This thesis is a combined work carried out at the University of Zambia and the Lund University in Sweden.

I would like to thank Professor Bjorn Karlsson of Lund University as my external supervisor and for making a special recruitment visit to the University of Zambia. He initiated the research topic and gave guidance throughout the experimentation, preparation and completion of this thesis.

Special thanks go to Professor Arne Roos and Dr. Maria Brogren both of Uppsala University (Sweden) for introducing me to the Perkin Elmer Lambda 900 spectrophotometer instrument for the reflectance measurements. Memories are still fresh on the introductory lectures by Professor Arne Roos on optical techniques, a bridging theoretical course for all Post-Graduate students at Uppsala University.

I wish to thank all the academic staff of the Department of Physics of the University of Zambia for their continued support in pursuing my postgraduate study program. In particular, I would like to thank Professor Prem C. Jain as my local supervisor and for the fruitful discussions and guidance throughout

my thesis. The great assistance from the technical staff can not be over-emphasized. I single out Mr. Bellingtone Changwe who constantly assisted in instrumentation especially in electronics and computer management.

I extend my thanks to the personnel of Lund University for their hospitality during my regular visits there. I would like to single out Dr. Hakan Hakansson, the man behind all experimental techniques, the design and the fabrication of tailor-made apparatus and equipment. I can not forget Mr. Johan Nilsson (PhD student) who introduced me to ray-tracing through Matlab and ZEMAX Softwares.

My special thanks also go to Professor Tara C. Kandpal of Institute of Indian Technology (IIT), New Delhi for his guidance towards my research proposal writing. His contribution during the Renewable Energy Technologies courses at IIT, New Delhi, sponsored by the Ministry of Non-conventional Energy Sources, India, in 2003 can not be forgotten. This trip was sponsored by the International Science Programme of the Uppsala Univerity.

Finally but not the least, I wish to thank Professor Lennart Hasselgren, Director of the International Programme in the Physical Sciences (IPPS), Uppsala University, Sweden, for the financial support rendered for the

completion of this work. The former Deputy Director, Dr. Johan Wennerberg is acknowledged for being a dependable colleague and companion at the Ängstrom Laboratory of the Uppsala University. Sincere gratitude also goes to the staff of the International Science Programme (ISP). I single out Ms Mona Thorwaldsdotter, the Senior Administrative Assistant to the Director, who saw to it that I had enough money for food and all my living expenses whilst in Sweden or attending a conference outside Sweden.

TABLE OF CONTENTS

List of symbols and abbreviations

a	half width of exit aperture of CPC	[m]
A	half width of entrance aperture of CPC	[m]
A_f	amplification factor of instrument	[--]
A_a	entrance aperture area	[m^2]
A_{ab}	absorber area	[m^2]
A_m	active area of module cells	[m^2]
C	theoretical concentration ratio	[--]
C_g	geometrical concentration ratio	[--]
C_L	local concentration ratio or brightness factor	[--]
C_{opt}	optical concentration ratio	[--]
CIS	copper indium diselenide	[--]
CPC	compound parabolic concentrator	[--]
d	diameter of exit aperture of a concentrator	[m]
D	diameter of entrance aperture of a concentrator	[m]
DR	diffuse reflectance	[%]
DIR	diffuse integrated reflectance	[%]
f	focal length	[m]
f_0	fraction of the solar flux that hits the absorber directly	[--]
f_1	fraction of the solar flux that hit the absorber after	

	one reflection	[--]
f_2	fraction of the solar flux that hit the absorber after two reflections	[--]
FF	fill-factor	[--]
$G(\lambda)$	wavelength dependent solar spectral irradiance	[W/m^2]
H	height of concentrator	[m]
H_b	incident beam radiation	[W/m^2]
$HH{:}MM$	solar time	[hr]
HG	horizontal groove orientation	[--]
ΔH_{bp}	projected beam irradiance in time interval Δt	[kWh/m^2]
$\hat{i}$	incident unit vector	[--]
I_i	total solar radiation incident on horizontal surface	[W/m^2]
I_{ext}	extraterrestrial solar radiation	[W/m^2]
I_{cpc}	solar radiation within CPC	[W/m^2]
I_m	maximum current	[A]
I_s	intensity of sample beam	[--]
I_{sc}	short-circuit current	[A]
I_{sc}^{conc}	short-circuit current under concentration	[A]
I_{sc}^{ref}	reference short-circuit current	[A]
I_{soc}	solar constant	[W/m^2]

I_N	solar intensity incident on area A_m	[W/m^2]
I_r	total solar radiation reflected on a surface	[W/m^2]
I_T	intensity of total solar radiation on horizontal surface	[W/m^2]
I_{TC}	total solar radiation reaching the absorber inside the CPC	[W/m^2]
I_t	total solar radiation on a tilted surface	[W/m^2]
I_b	beam or direct solar radiation on horizontal surface	[W/m^2]
I_d	diffuse radiation on horizontal surface	[W/m^2]
L_{st}	standard meridian (longitude) for actual time zone, East negative	[°]
L_{loc}	local meridian (longitude) of a location, East negative	[°]
n	day of the year	[--]
$\hat{n}$	normal unit vector	[m]
$<n>$	average number of reflections	[--]
N	number of sunshine hours	[hr]
P_m	maximum power	[W]
PSH	peak sun hours	[hr]
$\hat{r}$	reflection unit vector	[--]
R_{br}	conversion factor from beam radiation on horizontal surface to beam radiation on tilted surface	[--]
R_b	reflectance of reference sample coated with $BaSO_4$	[--]
R_{bn}	bulk resistance of the n-type material	[Ω]

R_{bp}	bulk resistance of the p-type material	[Ω]
R_{cn}	contact resistance in the n-type material	[Ω]
R_{cp}	contact resistance in the p-type material	[Ω]
R_{eff}	effective specular reflectance of the reflector	[%]
R_m	weighted wavelength dependent reflectance	[%]
R_s	series resistance	[Ω]
R_{sh}	shunt resistance	[Ω]
R_{sample}	reflectance of actual sample	[%]
$R(\lambda)$	wavelength dependent property of material	[%]
S_o	signal reading with a reference in place	[--]
S_r	signal reading with an actual sample in place	[--]
SR	specular reflectance	[%]
SIR	specular integrated reflectance	[%]
T	equilibrium temperature of the black body	[K]
T_a	ambient temperature	[K]
T_{ab}	absorber temperature	[K]
T_c	cell temperature	[K]
TR	total reflectance	[%]
TIR	total integrated reflectance	[%]
T_s	Temperature of the Sun	[K]

V_m	maximum voltage	[V]
VG	vertical groove orientation	[--]
V_{oc}	open-circuit voltage	[V]

GREEK SYMBOLS

α	altitude of the Sun or solar height or elevation	[°]
α_m	absorptance of the module cell	[--]
β	surface tilt to the horizontal	[°]
δ	declination angle of the Sun	[°]
θ	angle of incidence on a given surface	[°]
θ_c	acceptance half angle	[°]
θ_p	projection angle in the North-South plane	[°]
θ_z	zenith angle of the Sun	[°]
γ_s	solar azimuth angle, South zero, East positive	[°]
γ	orientation or azimuth of the surface normal	[°]
γ_i	intercept factor or flux concentration ratio	[--]
η	overall efficiency	[--]
η_o	optical efficiency	[--]
η_{th}	thermal efficiency	[--]
η_e	electrical efficiency	[--]

σ	Stefan-Boltzmann constant	[W/m^2/K]
ω	hour angle, noon zero, morning negative	[°]
ω_s	sunset / sunrise hour angle	[°]
ε	angle between sun vector and its projection on N-S plane	[°]
ϕ	geographic latitude of a place, North positive	[°]
ϕ_a	angle subtended by axis parabola of a symmetric CPC with the absorber normal	[°]
ρ	albedo of the earth	[--]

Chapter 1

HYPOTHESES AND OBJECTIVES

The World's energy demand has been increasing mainly due to the increase in population, industrialization, agricultural production and the general increase in the standard of living. The global challenge is to produce enough energy at relatively low cost and with minimum environmental damage. The World's energy today comes mainly from the burning of fossil fuels such as coal, oil and gas which are exhaustible and cause serious environmental hazards. Nuclear power plants have radioactive waste disposal problem. Hydroelectric power is probably the cheapest energy source but the creation of large water reservoirs (dams) for large water heads forces migration of inhabitants and the subsequent changes in the general ecosystem.

To meet this energy demand, there is need to use alternative energy sources called renewables such as solar energy, biomass, wind energy, geothermal, tidal and wave energy. The most promising renewable energy source is probably solar energy. The only major setback is that solar energy is not evenly distributed over the earth's surface; it is highly intermittent and needs to be converted into useful energy. Similarly, other renewable energy sources are highly site specific and scantly distributed.

The Sun is the ultimate source of solar energy whose average surface temperature is about 5762K. The core of the Sun is at a temperature of several millions of degrees Celsius and acts as a blackbody, emitting radiation in all directions. The amount of radiation received per unit area by a surface perpendicular to the sun's rays outside the earth's atmosphere is 1367W/m^2 called the solar constant[1]. However, the amount of solar radiation reaching the earth's surface after attenuation through reflection, absorption and scattering averages about 1000W/m^2 at noon on a clear day. This energy is in the form of electromagnetic radiation which could be converted into heat energy and as well as light energy.

Despite the abundance of silicon and the maturity of solar cell technology, the cost of solar cell modules dominates the total cost on the solar system. Concentrating photovoltaic systems use less amount of silicon material by simply increasing the amount of radiation through concentration. However, the use of highly specular reflective materials causes hot-spot formation due to increase in temperature[2]. The addition of active cooling mechanisms on the solar cell module reduces the temperature but has an added cost to the total cost of the system. In low concentrating photovoltaic systems, string solar cells are used to reduce the amount of solar material and simply increase solar

radiation by using relatively low-cost diffuse reflector materials. The overall cost reduction comes in by replacing the most expensive solar cells with less expensive materials as booster reflectors[2].

The study attempts to test the following hypotheses:

(i) Optimal tilt of a solar photovoltaic module will improve its output.

(ii) The use of semi-diffuse and/or specular reflectors will solve the problem of uneven illumination on photovoltaic modules in low concentrating compound parabolic concentrators.

(iii) The use of semi-diffuse and/or specular reflectors will improve the fill-factor of photovoltaic modules in low concentrating compound parabolic concentrators.

The central aim of this thesis was to study the performance of the photovoltaic systems under low concentration using low-cost diffuse reflectors. The specific objectives of this thesis were to

(i) estimate the collectable global (total) energy on a tilted surface located in Lusaka,

(ii) estimate the projected beam energy for Lusaka using Winsun software,

(iii) compare the integrated reflectance of structured aluminium samples using the integrating sphere,

(iv) compare the performance of a symmetrical CPC with different reflector materials and estimate their effective specular reflectance,

(v) test the Copper Indium diselenide (CIS) module under low concentration and monitor the fill-factor changes under structured reflectors,

(vi) test the performance of a large parabolic reflector and estimate its optical efficiency,

(vii) compare the degradation effects of some commercial reflectors to environmental conditions.

To achieve these objectives, we estimate the solar resource available on a tilted surface at low latitudes in chapter 2. In chapter 3, we make a brief review of the historical perspective of solar concentrator technology and their subsequent parameters. We survey in chapter 4 the characteristics of solar materials used in concentrator geometry and in particular the reflectance measurements of specular and diffuse materials. We take a general overview of the performance characteristics of a photovoltaic system in chapter 5. In chapter 6, we present the major instruments, apparatus, techniques and the proposed models used in the thesis. In chapter 7 we give the major findings and plausible scientific

explanations to the results. In chapter 8 we outline the main conclusions and recommendations for future work.

Chapter 2

SOLAR RESOURCE

2.1 Introduction

The operation of a photovoltaic system at a given geographic location requires a detailed characterization of the solar resource available at the site. The annual insolation over the surface of the earth varies by a factor of 3 from a maximum of about 2500kWh/m^2/year in dry desert areas[3,4] to an average of about 800kWh/m^2/year in Canada and Northern Scandinavian countries[3,4]. The total annual solar power available on the surface of the earth exceeds the total human power consumption by roughly a factor of 1,500[3,4]. Calculated per person, the average solar power available is 3MW, while the average power use varies from 100W in least developed countries to 10kW in USA[3,4]. These figures provide a global potential of solar energy, however, the technical and economic potentials are regionally dependent upon the solar energy availability, energy infrastructure, population density, geographical conditions, financing schemes and not least, the political environment of a region or country.

The factors that affect solar radiation on a receiver surface on earth include the geographical location, the receiver inclination and orientation, the time of the

day, the time of the year, and the atmospheric conditions[1]. In this chapter, we focus on the type of receiver and its orientation in solar energy collection. Suffice to mention that tracked systems collect more solar energy than stationary ones, and surfaces tilted towards the equator intercept more of solar radiation than horizontal collectors[5].

2.2 Earth – Sun Geometry

The position of the Sun in the sky may be located by its altitude α and azimuth γ_s. The solar altitude is defined as the angle between the Sun's rays and the horizontal plane while solar azimuth is the angle between the projected Sun's rays on a horizontal plane and the South direction. The Sun's azimuth due South is 0^o and North is 180^o as shown in figure 2.1. As the Sun sweeps across the sky from East to West, its altitude (solar height) increases and becomes a maximum at solar noon, and decreases to zero at sunset. Thus, the differences in the amount of solar radiation received on earth during any time of the day of the year are due to the variation in the altitude and azimuth angles.

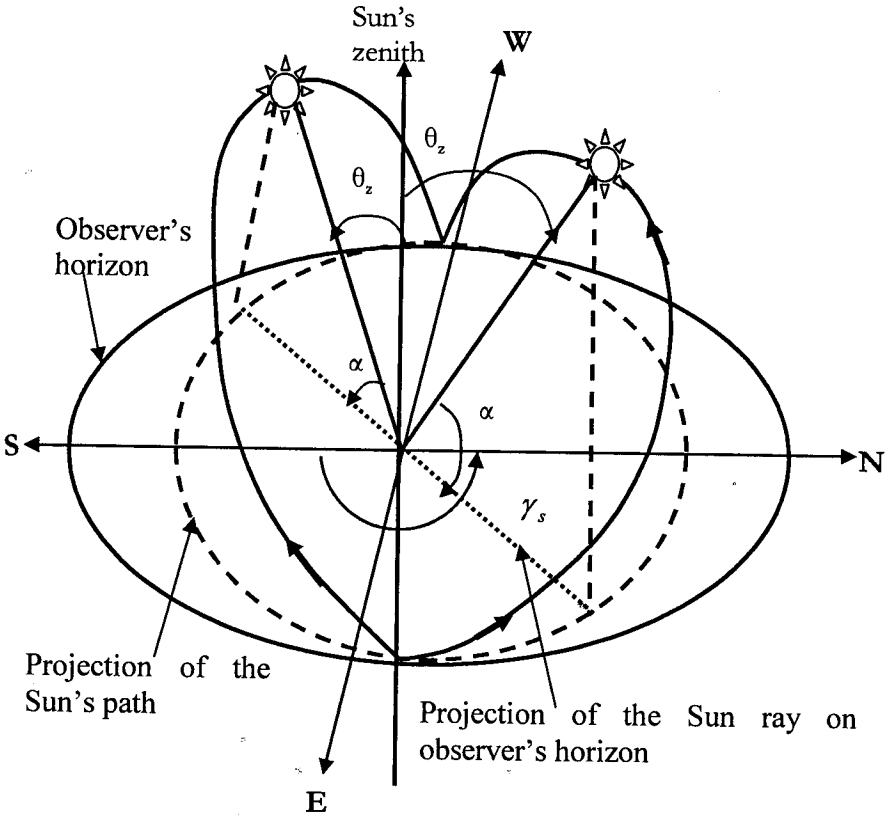

Figure 2.1: The apparent motion of the Sun for an observer in the southern hemisphere[6].

The trigonometric relationship between the Sun (centre of the solar disk) and a horizontal surface on earth is given by[1,6,7]

$$\sin\alpha = \sin\delta\sin\phi + \cos\delta\cos\phi\cos\omega = \cos\theta_z. \qquad 2.1$$

The declination of the Sun δ, is the angular displacement of the Sun from the equatorial plane, θ_z is the zenith angle in degrees, defined as the angular position of the Sun with the vertical, ω is the hour angle in degrees, defined as

the angle with which the earth should rotate to bring the observer's meridian under the Sun, and ϕ is the geographic latitude of a place in degrees. The corresponding solar azimuth angle may be obtained from[6,7]

$$\cos\gamma_s = \frac{\sin\alpha\sin\phi - \sin\delta}{\cos\alpha\cos\phi}. \qquad 2.2$$

2.3 North Projected Solar Height Angles

A general rule of thumb has been to orient a collector at a tilt equal to the latitude and zero azimuth. However, quantitative analysis of the total beam energy received on a collector may be understood from the projected solar radiation on the North-South vertical plane. This entails evaluating the projected solar height angle (θ_p) on the North-South plane. The Sun ray vector may be projected either on the horizontal plane or on the vertical North-South plane as shown in figure 2.2. The horizontal projected ray vector may be further resolved into two perpendicular components to define the horizontal and vertical azimuth as shown in figure 2.2.

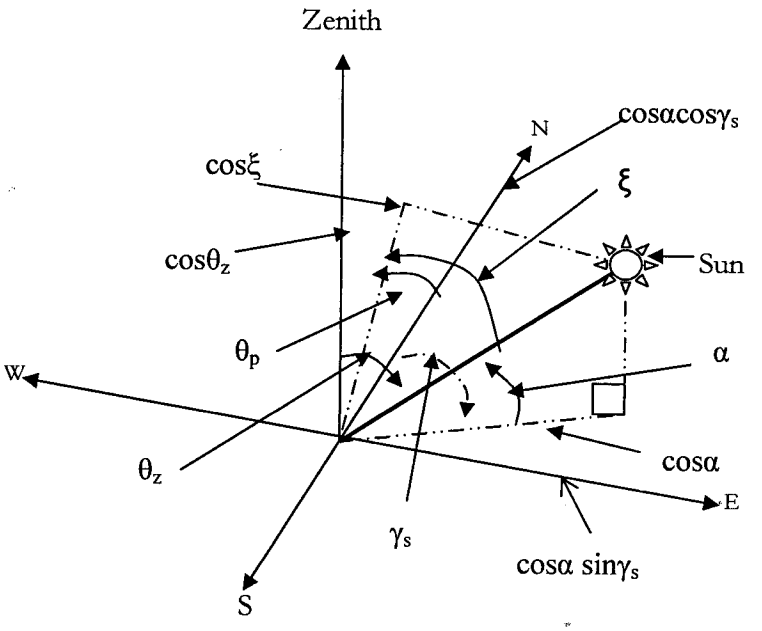

Figure 2.2: Projections of the solar vector on the horizontal plane (observer's horizon) and on the vertical North-South plane.

From figure 2.2, it is easy to show that

$$\sin\varepsilon = -\cos\alpha \sin\gamma_s \qquad \text{and} \qquad 2.3$$

$$\cos\varepsilon \cos\theta_p = \cos\alpha \cos\gamma_s, \qquad 2.4$$

where ε is the angle subtended by the Sun ray vector and its projection on the North-South vertical plane. From which, the projected solar height angle (θ_p) may be calculated from

$$\cos\theta_p = \frac{\cos\alpha \cos\gamma_s}{\sqrt{1-\sin^2\varepsilon}}. \qquad 2.5$$

The right hand side of equations 2.3 and 2.4 are known from $\cos\delta\sin\omega$ and $\cos\phi\sin\delta - \sin\phi\cos\delta\cos\omega$ respectively[8,9,10]. It is also easy to show that

$$\tan\theta_p = \frac{\tan\alpha}{\cos\gamma_s}. \qquad 2.6$$

The projected angle of incidence ($90 - \theta_p$) which defines the amount of solar radiation accepted or rejected by a 2D stationary concentrator may be expressed as in equation 2.7 and must be less than the acceptance half angle.

$$\tan\theta_i = \frac{\cos\gamma_s}{\tan\alpha}. \qquad 2.7$$

2.4 Solar Time

Solar noon is the time of the day when the Sun crosses the observer's meridian. The difference in hours between solar time and standard time (clock time) is[1,7]

$$Solar\ time - Standard\ time = (L_{st} - L_{loc})/15 + E/60, \qquad 2.8$$

where L_{st} is the standard meridian for the local time zone in degrees, East negative (Lusaka = -30°), L_{loc} is the longitude of the location in degrees (Lusaka = -28°), and E is the equation of time (in minutes) and may be expressed as[1,7]

$$E = 229.2(0.000075 + 0.001868\cos B - 0.032077\sin B - 0.014615\cos 2B - 0.04089\sin 2B), \qquad 2.9$$

where $B = (n\text{-}1)\ 360/365$ and n is the day of the year.

Since the earth rotates 15 degrees every hour, the hour angle in degrees may be calculated from

$$\omega = 15\left[(HH - 12) + \frac{MM}{60}\right], \qquad 2.10$$

$HH{:}MM$ is the solar time, HH hours and MM minutes.

2.5 Extraterrestrial Solar Radiation

The Sun behaves almost like a blackbody radiating energy in all directions. The amount of solar radiation outside the earth's atmosphere is called the extraterrestrial solar radiation and may be estimated as[7]

$$I_{ext} = I_{soc}\left[1.0 + 0.033\cos\left(\frac{360n}{365}\right)\right], \qquad 2.11$$

where n is the day of the year and I_{soc} is the solar constant.

2.6 Terrestrial Solar Radiation

Before reaching the earth's surface, solar radiation is attenuated by absorption, scattering and reflection. The absorption is mainly due to the presence of ozone, oxygen, nitrogen, carbon dioxide, carbon monoxide, and water vapour in the atmosphere. The scattering is due to air molecules, dust particles, water

droplets, and other small particles. The reflection is due to clouds and large particles in the atmosphere. The spectral attenuation of the atmosphere is shown in figure 2.3[11].

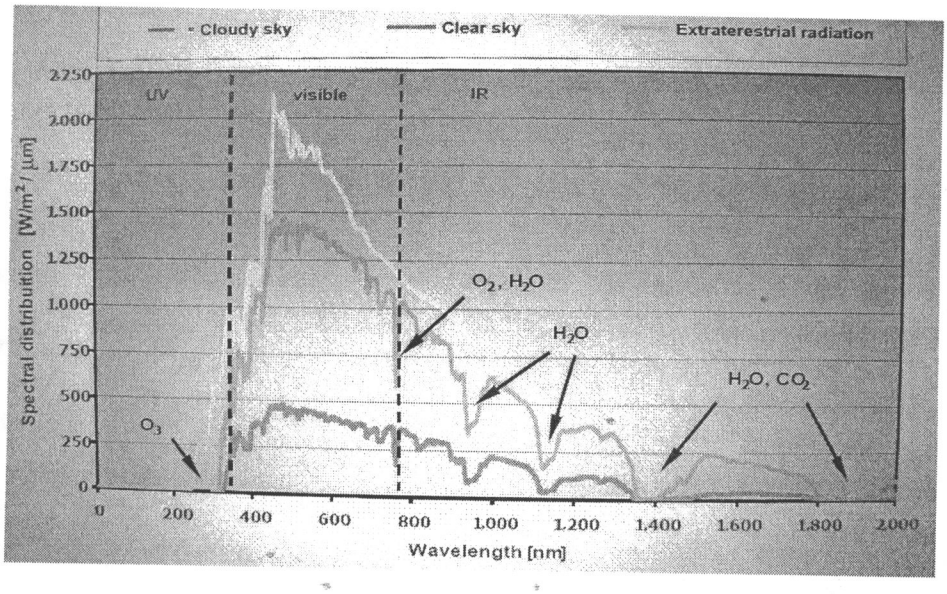

Figure 2.3 Spectral distribution of solar radiation for cloudy sky, clear sky and extraterrestrial sky [11].

The atmospheric attenuation of radiation is determined by the air mass. The air mass is defined as the ratio of the optical thickness of the atmosphere through which beam radiation passes to the optical thickness if the Sun were at zenith[7,12,13] as shown in figure 2.4

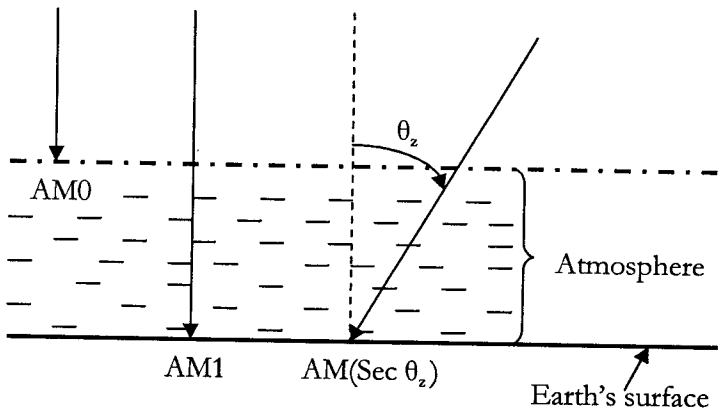

Figure 2.4: Different air masses traversed as the Sun rays penetrate the earth's atmosphere at different angles.

The angle of incidence θ_i of the Sun rays on an inclined plane is given by[1,6]

$$\cos\theta_i = (\cos\phi\cos\beta + \sin\phi\sin\beta\cos\gamma)\cos\delta\cos\omega + \cos\delta\sin\omega\sin\beta\sin\gamma + \sin\delta(\sin\phi\cos\beta - \cos\phi\sin\beta\cos\gamma). \qquad 2.12$$

β is the angle of tilt of surface to the horizontal. Clearly, for a horizontal surface facing south, ($\gamma = 0, \beta = 0, \theta_i = \theta_z$) equation 2.12 reduces to the usual equation 2.1. Similarly, for a surface facing north, γ = 180, equation 2.12 reduces to the familiar equation 2.13.

$$\cos\theta_i = \sin\delta\sin(\phi + \beta) + \cos\delta\cos(\phi' + \beta)\cos\omega \qquad 2.13$$

The sunset hour angle ω_s on a tilted surface may be obtained from equation 2.13 by replacing θ_i by 90° and ω by ω_s as

$$\omega_s = \cos^{-1}(-\tan(\phi+\beta)\tan\delta). \qquad 2.14$$

The total number of sunshine hours N may be expressed as

$$N = \frac{2\omega_s}{15}. \qquad 2.15$$

2.7 Available Solar Radiation on a Tilted Surface

The total solar radiation incident on a tilted surface consists of beam radiation I_b, diffuse radiation I_d, and the reflected radiation I_r. Usually, solar radiation is measured on a horizontal surface and converted into radiations on a tilted surface. Equation 2.16, converts solar radiations on a horizontal surface to that on a tilted surface and was proposed by Jordan and Liu (1961)[14] and used by Garg and Prakash (2000)[15]. Thus, the global radiation on a tilted surface I_t is calculated from the measured values of the global radiation I_h and diffuse radiation I_d on a horizontal surface as

$$I_t = I_h\left[\left(1-\frac{I_d}{I_h}\right)R_{br} + \frac{I_d}{I_h}\left(\frac{1+\cos\beta}{2}\right) + \rho\left(\frac{1-\cos\beta}{2}\right)\right] \qquad 2.16$$

$$\text{where } R_{br} = \frac{\cos(\phi+\beta)\cos\delta\sin\omega' + \frac{\pi}{180}\omega'\sin(\phi+\beta)\sin\delta}{\cos\phi\cos\delta\sin\omega + \frac{\pi}{180}\omega\sin\phi\sin\delta}. \qquad 2.17$$

$$\text{And } \omega' = \min[\cos^{-1}(-\tan\phi\tan\delta), \cos^{-1}(-\tan(\phi+\beta)\tan\delta] \qquad 2.18$$

R_{br} is the conversion factor for converting beam radiation on horizontal surface to beam radiation on a tilted surface and ρ is the albedo.

2.8 Peak Sun Hours (PSH)

The term peak sun hours (PSH) or equivalent hours of full sunlight (EHFS), expresses the incident solar energy on a unit area and is defined as the number of hours of incident sunlight at a place if the sunlight intensity were at its constant value of $1kW/m^2$. The area under the curve of the incident solar radiation in W/m^2 as a function of time of the day in hours gives the total solar energy received by the unit surface on that particular day. The concept of peak sun hour is used in sizing solar photovoltaic systems[5]. The approximate energy output from a photovoltaic module at a place could be computed from the peak sun hours at that place and the rating of the module. Two widely separated places with the same latitude but with different longitudes could have the same value of sunshine hours but different PSH values[5].

Chapter 3

SOLAR CONCENTRATORS

3.1 Introduction

A device that is capable of concentrating solar energy incident over a relatively large surface onto a smaller surface is called a Solar Concentrator. Concentration is achieved by the use of suitable reflecting or refracting elements which increases the flux on the absorber surface as compared to that on the concentrator aperture. Ideally, the concentrating system should track the Sun so that the Sun rays always remain focused onto the absorber. Thus, a solar concentrator system will consist mainly of an absorber/receiver with or without a glazing, a focusing device and a tracking device. Solar concentrators can be used both for thermal and photovoltaic applications.

Solar concentrators for thermal applications have advantages such as[16,17,18]

(i) achieving a thermodynamic match between the temperature level and the task in question for high temperature operation,

(ii) reducing cost by replacing an expensive large receiver area with less expensive reflecting or refracting elements.

Besides being an optical system with optical losses, solar concentrators have a problem of non-uniform illumination on absorbers which become prominent

especially for high concentrations[19,20,21]. The problems of non-uniform illumination cause hot spot formation on the absorber and lead to the decrease in the efficiency of the system. In this thesis, we address the problem of non-uniform illumination by using structured diffuse reflective elements in low concentrating systems. Diffuse reflectors with grooves parallel to the plane of the module have the possibility of improving the fill factor of the module as they are capable of scattering the solar flux at larger angles.

3.2 Classification of Solar Concentrators

Solar concentrators maybe classified as tracking type or static type[15,16]. A concentrator may be mounted on a single-axis or on a double-axis tracker and be moved continuously or intermittently to follow the sun. Concentrators may also be classified on the basis of their optical components. Thus, they may be (i) reflecting or refracting (ii) imaging or non-imaging, and (iii) line focusing or point focusing type. The reflecting or refracting surface may be one piece or a composite surface; it may be a single stage or two stage system and may be symmetric or asymmetric. Figure 3.1 shows some of the low- concentrating solar concentrator systems that have been installed at high latitudes.

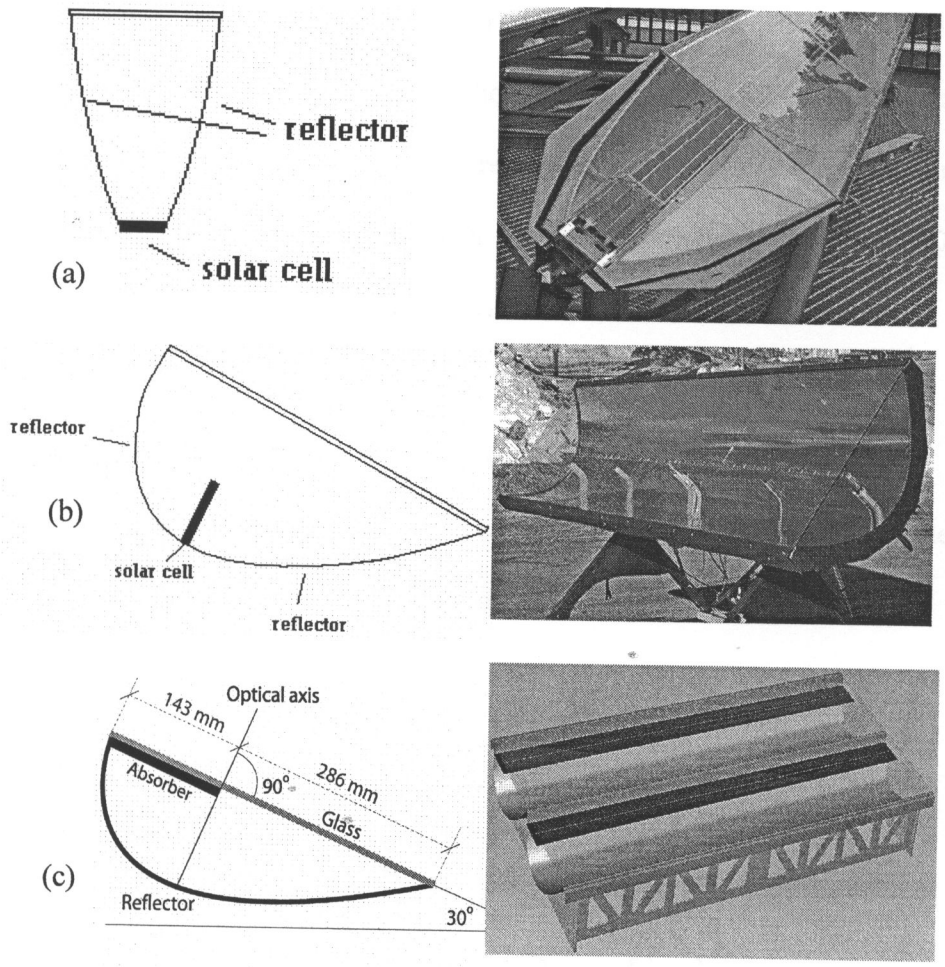

Figure 3.1: Solar concentrators (a) symmetric compound parabolic concentrator (CPC), (b) asymmetric maximum reflecting concentrator (MaReCo) and (c) asymmetric CPC, (courtesy of Bjorn Karlsson, 2007).

In practical situations, the concentration provided by existing solar concentrators may range from as low as 1.5 to 10 for static or intermittently tracked concentrators to as high as several thousands for perfectly tracked

systems[16]. Generally, solar concentrators with concentration ratios 1.5 to 10 are referred to as low concentrators as those shown in figure 3.1 and those with concentration ratios 10 to 100 are referred to as moderate or medium concentrators. Solar concentrators with concentration ratios greater than 100 are called high concentrators such as paraboloids[17].

3.3 Solar Concentrator Parameters

Figure 3.2 shows some parameters that characterize a CPC system. We further give some of the definitions of the parameters.

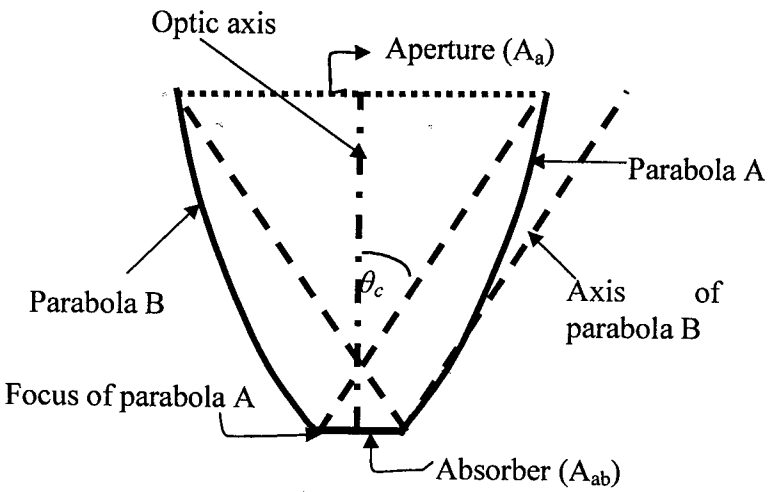

Figure 3.2: Some characteristic parameters of a compound parabolic concentrator geometry.

The opening of the concentrator which intercepts the incident solar flux is called the aperture area (A_a). The total area of the absorber surface that receives the concentrated solar flux and delivers the useful energy to the system is called the absorber area (A_{ab}). The geometrical concentration ratio (C_g) is the ratio of the aperture area to the area of the absorber and is given by

$$C_g = \frac{A_a}{A_{ab}}. \qquad 3.1$$

The local concentration ratio (C_L) is the ratio of the solar radiation at any point on the absorber surface to the incident radiation at the aperture of the solar concentrator. It is also known as the brightness concentration factor and is a more meaningful term to describe the non-uniformity of illumination. The local concentration ratio may be calculated from the measurements of the flux distribution apparatus described in section 6.6.3 or from the ray tracing techniques described in section 6.6.4.

The acceptance angle $(2\theta_c)$ is is the limiting angle over which incident ray path may deviate from normal to the aperture plane and still reach the absorber/receiver. A concentrator with large acceptance angle needs only seasonal adjustment in a year while a concentrator with small acceptance angle must be moved continuously to track the Sun. The optical efficiency (η_o) is the

ratio of the energy absorbed by the absorber to the energy incident on the concentrator aperture. It includes the effect of reflector/refractor surface, shape and reflection/refraction losses, tracking accuracy, shading, receiver-cover transmittance and the absorptance of the absorber. The thermal efficiency (η_{th}) is the ratio of the useful energy delivered to the system to the energy incident at the concentrating aperture. In a thermal conversion system, a working fluid is used to extract energy from the absorber. The thermal performance of a solar concentrator is described by its thermal efficiency.

The electrical efficiency (η_e) is the electrical performance of a solar concentrator is described by its electrical efficiency which is defined as the ratio of the maximum power to the total solar power received by the absorber.

$$\eta_e = \frac{P_m}{I_N A_{ab}} . \qquad 3.2$$

3.4 Collection of Solar Irradiation by Solar Concentrators

In chapter one we mentioned that solar radiation was scattered by aerosols, dust particles, ozone and water vapour molecules in the earth's atmosphere. Since diffuse radiation comes from all directions, some of it falls beyond the acceptance angle of the concentrator and is lost. If the diffuse radiation is assumed to be isotropic, it can be shown[16,19] that the amount of solar radiation

reaching the absorber or solar module inside the CPC of concentration ratio C is given by[15]

$$I_{TC} = I_{cpc}\left[1 + R_{eff}^{\langle n \rangle}\right] \qquad 3.3$$

where R_{eff} is the specular reflectance of the reflector used, <n> is the average number of reflections within the CPC and the solar radiation within the CPC is given by[15]

$$I_{cpc} = I_t - (1 - \frac{1}{C})I_d . \qquad 3.4$$

Where I_t is the total solar radiation falling on the CPC aperture and I_d is the diffuse radiation falling on the CPC aperture.

3.5 Static and Tracked Solar Concentrators

Most stand alone photovoltaic systems have their modules fixed at an angle equal to the latitude of the location. However, their structures may allow adjustments in the tilt angle as well as in the azimuth angle. Fixed tilt structures do not capture as much solar radiation as tracked systems[5]. In single axis tracking, the frame may rotate from East to West (vertical axis) or may rotate North-South on an East-West axis. In two axis tracking, the module frame has an additional rotation about the East-West axis and the module tilt angle changes daily as the sun moves. Although double axis trackers absorb more solar radiation than single axis trackers, they are rather complicated and

expensive. Figure 3.3 shows a hypothetical output from a fixed tilt, single axis tracking and from a double axis tracking system.

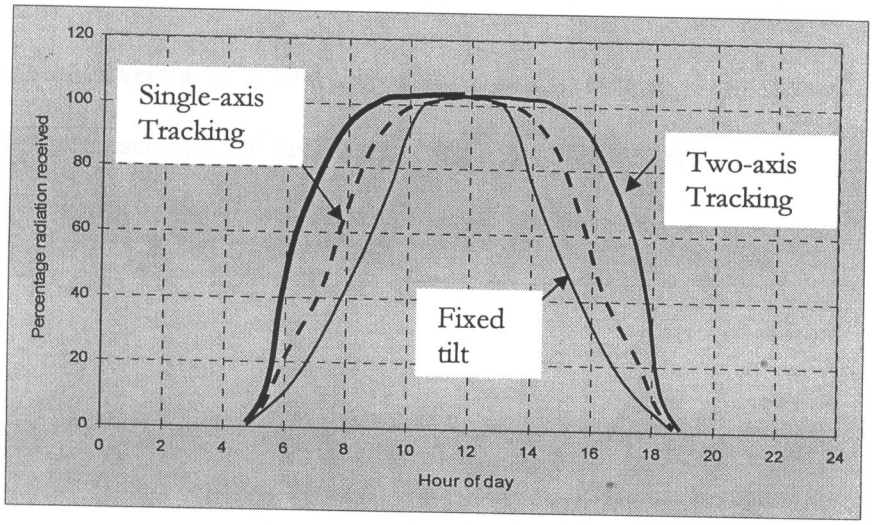

Figure 3.3: A hypothetical variation of daily solar radiation for fixed tilt, single axis tracked and double axis tracked modules (after T.Bhattacharya[5], 1998).

3.6 Vector Formulation of the Law of Reflection

Geometrical optics plays an important role in the design of almost all solar concentrator types. The major part of the design process involves following the paths of the Sun rays through a system of reflecting or refracting surfaces. This procedure is known as the ray-tracing. When light is reflected from a smooth surface it obeys the laws of reflection and when transmitted, the light

ray direction is changed according to the Snell's law. In order to formulate ray tracing procedure suitable for all cases, it is convenient to put the laws of reflection in vector form[16,20]. We denote the incident unit vector as $\hat{i}$, the normal unit vector as $\hat{n}$ and the reflected unit vector as $\hat{r}$. In figure 3.4, we make a representation of ray-tracing from a specular surface.

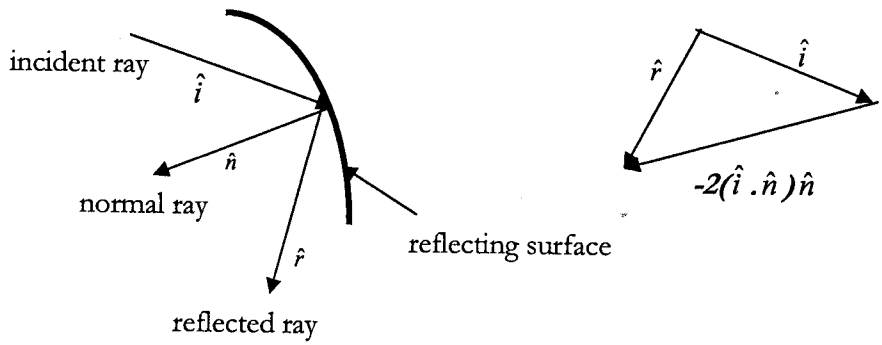

Figure 3.4: Vector formulation of reflection. (after Welford and Winston[20], 1989)

The law of reflection states that the angle of incidence equals the angle of reflection and may be written in vector form as

$$\hat{i}.\hat{n} = \hat{r}.\hat{n} \qquad 3.5$$

The second law of reflection states that the incident ray, the reflected ray, and the normal all lie in the same plane and may be written in vector form as

$$(\hat{i} \times \hat{r}) . \hat{n} = 0 \qquad 3.6$$

If any two of these vectors are given, the third one may be uniquely determined and the direction of the reflected ray may be written as[16,20]

$$\hat{r} = \hat{i} - 2(\hat{i} . \hat{n}) \hat{n} . \qquad 3.7$$

Thus, to ray trace through a reflecting surface, one needs to know the direction of the incoming ray, the point of incidence and the normal at the point of incidence using the known shape of the surface. Finally, the direction of the reflected ray may be calculated from equation 3.7. This process is repeated for any number of rays intercepting the concentrator as will be seen in section 6.6.4.

3.7 Compound Parabolic Concentrators (CPCs)

A compound parabolic concentrator is a non-imaging concentrator and has the highest permissible theoretical thermodynamic limit for a given acceptance angle. Since it has large angle of acceptance, it requires only intermittent adjustment towards the Sun. The first designs were proposed independently by Baranov and Winston in 1966. The present designs are well described in Welford and Winston's book[20]. A 2-D compound parabolic concentrator is shown in figure 3.5. It consists of two distinct parabolic segments placed such that the focus of one parabola is at the foot of the other. The slope of the

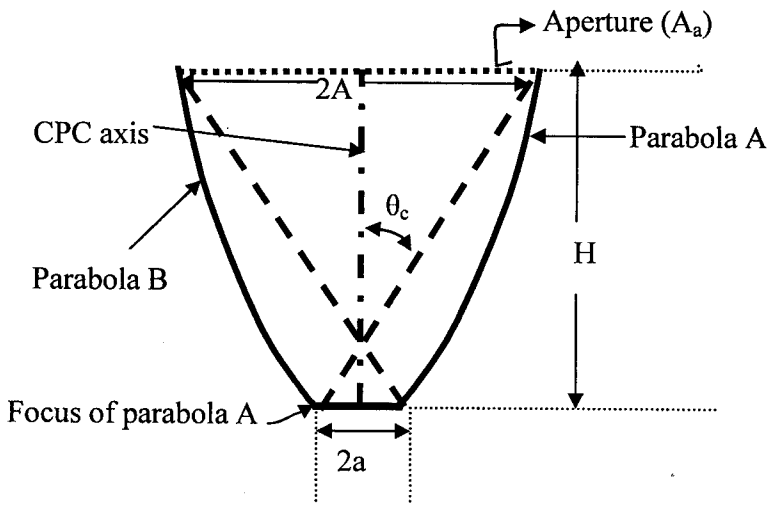

Figure 3.5: Schematic diagram of the compound parabolic concentrator geometry.

reflector surface at the aperture is parallel to the CPC axis. Thus, any ray within the acceptance angle end up at the focus of the parabola after reflection. From figure 3.5, it is easy to show that the height of the CPC may be given by[15]

$$H = \frac{A + a}{2\tan\theta_c}. \qquad 3.8$$

The theoretical concentration ratio of the CPC is given by[20]

$$C = \frac{A}{a} = \frac{1}{\sin\theta_c}. \qquad 3.9$$

Combining equations 3.8 and 3.9, the height of the CPC may be expressed as

$$H = \frac{A(1+\sin\theta_c)}{2\tan\theta_c}. \qquad 3.10$$

Equation 3.10 may be expressed as a ratio of the height H and exit aperture side a as[16]

$$\frac{H}{a} = \frac{1}{2}(C+1)\sqrt{C^2-1}. \qquad 3.11$$

For non-tracking solar concentrators with maximum concentration, one uses CPC troughs aligned in the East-West direction. At least 7 hours of operating time at solstices are possible with a maximum concentration factor of ten[16].

3.7.1 Angular Acceptance Characteristics of CPCs

The angular characteristics of a compound parabolic concentrator may be studied using the conventional ray-tracing procedures[16,20,21]. Figure 3.6 shows the angular acceptance of a compound parabolic concentrator. For a full CPC all rays incident on the aperture within the acceptance angle, $|\theta_i| < \theta_c$, reach the absorber, whereas all rays with $|\theta_i| > \theta_c$, bounce back and forth between the reflector sides and finally re-emerge through the aperture. In most applications, a CPC is truncated by cutting the upper part of the concentrator. The truncation process reduces both CPC material and the reflector material with very little changes in the optical performance[16].

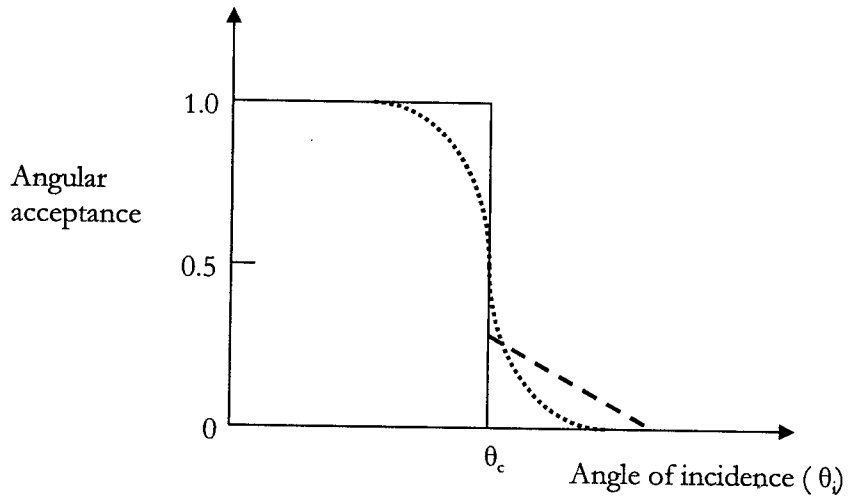

Figure 3.6: Shows fraction of incident radiation that reaches the absorber within an acceptance half angle of θ_c. A full CPC with perfect reflectors is shown by _____, a truncated CPC by _ _ _ _ _ and a CPC with optical losses by ....., (after A.Rabl[21], 1976a).

If a CPC is truncated, some rays outside the acceptance angle ($|\theta_i| > \theta_c$) could still reach the absorber. Figure 3.6 also shows the effect of angular acceptance as a function of truncation.

Chapter 4

SOLAR CONCENTRATOR MATERIALS

4.1 Introduction

In chapter three, we mentioned that a reflective solar concentrator consists mainly of a reflecting surface, a receiver (module cells), and a self supporting structure or a well adjusted tracking arrangement. In this section of the thesis, we concentrate on the long term degradation of reflector materials used in solar photovoltaic concentrators for low concentrations such as miro, rolled aluminium foil laminated on plastic, anodized aluminium, evaporated aluminum laminated on plastic, and evaporated aluminium laminated on steel. Although silver is an excellent reflector material, its cost and stability problems inhibit its usage. Aluminium has a solar reflectance of 92% as compared to 96% for silver. Aluminium has a characteristic high parallel band absorption at 826nm[22] and has long term stability when treated[23].

4.2 Materials for Reflective Solar Concentrators

Traditionally, solar concentrators with reflective elements have been designed and used for high temperature applications. This requires high quality mirrors with good specular reflectance[13]. The overall aim is to focus the Sun rays onto a point or a line. Other important reflector material considerations include the

effect of dust accumulation and other environmental factors, the stability of reflective metallization, the cleaning problems and the projected price of the entire concentrator structure. However, very little is known about the long term effect of such environmental factors of dust, sand, and miscellaneous contamination on reflective surfaces[16,24]. These effects would certainly vary with the type of material, duration of exposure, site location, type of coating (s) and the cleaning techniques involved.

The use of reflective elements in low concentrating systems has shown problems in large area applications for high reflectance[25], and outdoor durability[26]. Specular reflectors lower the fill-factor of the solar cell modules due to increased temperature. Diffuse reflectors[27] and Fresnel lens[28,29] have been tried in low concentrating systems so as to scatter solar flux and hence reduce the problem of non-even illumination. Thin film selective reflective coatings which reflect light of specific wavelength have been tried[30].

4.3 Properties of Reflective Solar Surfaces and Coatings

Besides being an abundant metal, aluminium is the 3rd most abundant element in the earth's crust after oxygen and silicon[31]. Aluminium has good mechanical properties, is relatively inexpensive and easy to recycle. Anodized aluminium shows longer life due to the Al_2O_3 layer which protects the metal

from further reaction[32]. Miro is a commercial name for a sheet of aluminium coated with $TiO_2/SnO_2/Al_2O_3$. Titanium oxide coat gives it a high reflectance in the visible compared with anodized aluminium but is rather weak environmentally.

Solar reflective materials must have the following requirements:

(i) They must reflect as much as possible the incident solar radiation onto the receiver. Photons with lower energy than the band gap of the solar cells material do not contribute to photoelectric conversion but only to the heating of solar cells.

(ii) They must maintain high reflectance (specular or diffuse) for the entire life of the system (20 to 25 years). Optical degradation results from soiling agents on the surface and some reaction of reflector surface with compounds in the atmosphere[23].

4.4 Diffuse and Specular Reflecting Materials

When an incident ray of light strikes a surface, its reflectance might be mirror-like (specular) or might scatter in all directions (diffuse). In the specular case, the incident polar angle is equal to the reflected polar angle, and the azimuth angles differ by 180°. In the diffuse case, the reflected radiation is distributed

uniformly in all directions. In practice however, the reflection from a surface is neither all specular nor all diffuse[1,33]. The two general cases along with the two limiting situations are shown in figure 4.2.

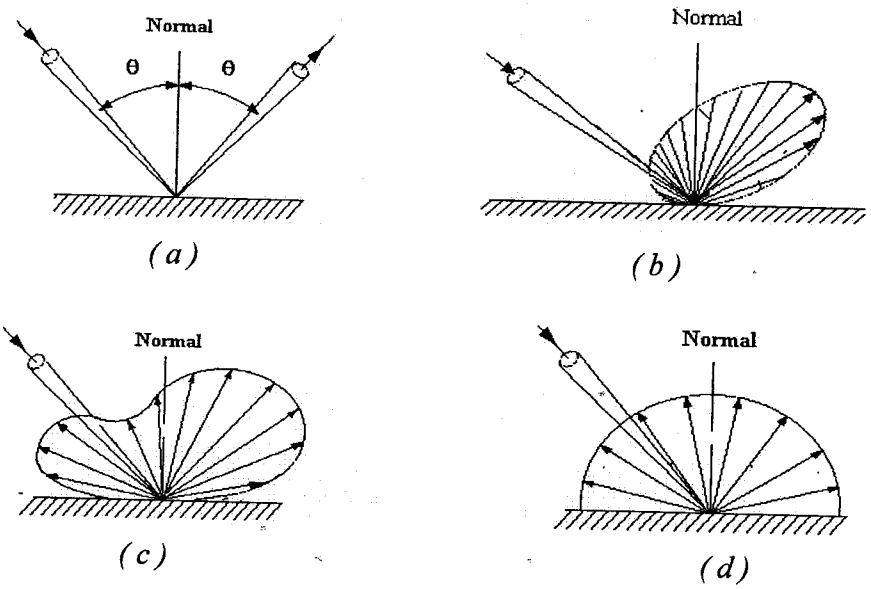

Figure 4.2: (a) specular reflection, (b) diffuse reflection with significant specular component, (c) general diffuse reflection, and (d) uniform diffuse reflection, (after Duffie and Beckman[1], 1991).

4.5 Measurements of Reflectance

The spectrophotometer measures light intensities with respect to the wavelength. In figure 4.3, we show a picture of the Perkin Elmer Lambda 900 that was used in reflectance measurements. A beam of light from the source, usually halogen lamp *(HL)* and deuteron lamp *(DL)* is reflected by focusing mirrors to the gratings. The chopper helps to remove the background contribution to the signal.

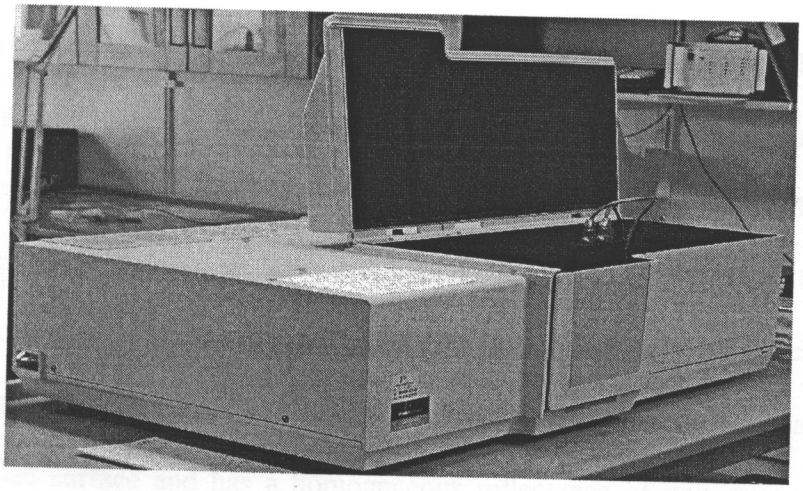

Figure 4.3: Picture of the Perkin Elmer Lambda 900 spectrophotometer at the Ångström Laboratory, Uppsala University, (Picture by Bengt Götesson, 2007).

This technique increases the signal to noise ratio but effectively reduces the contributions of stray light and the background. The grating reduces the white light to monochromatic light which is sent to the filter and transmits light only

in certain wavelength range to the detectors. Modern commercial spectrophotometer instruments are mostly double-beam.

4.5.1 The Integrating Sphere

It is hard to design an instrument that correctly and accurately measures either diffuse and specular reflectance or transmittance due to the inherent errors in the instruments and also due to some sample dependent errors[34,35,36]. An integrating sphere (also known as the Ulbricht-sphere) and a Total Integrating Sphere *TIS* (also known as the Oblentz sphere are the two commonly used instruments in optical measurements. The integrating sphere measures an average of the scattered light after it has been homogeneously scattered inside a white sphere coated with Barium sulphate ($BaS0_4$) or Teflon. Thus, light is repeatedly reflected inside the sphere and a homogeneous intensity is achieved which the detector then detects. A completely diffuse surface is called a lambertian surface and has a homogeneous reflectance of unit over a wide range of wavelengths. In the total integrating sphere *(TIS)*, the light from the sample is reflected by focusing mirrors onto a detector. This results into higher intensity and hence a detector must be sensitive to incident light from high angles of incidence. An integrating sphere shown in figure 4.4 is best used for isotropic scattering samples. A reference measurement is taken when the sample is replaced by a reference sample coated with $BaS0_4$.

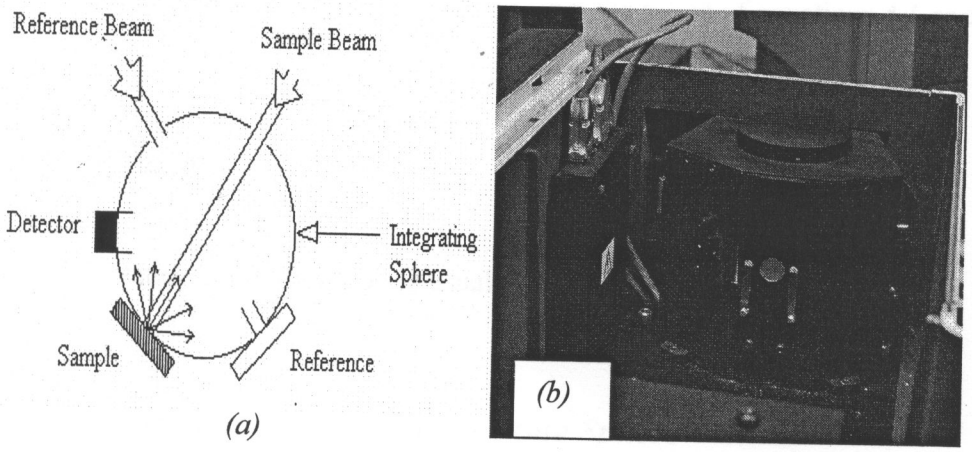

Figure 4.4: (a) Schematic arrangement of the integrating sphere in the reflectance measurement mode (courtesy T.B Chibuye[33] 2004) and (b) picture of the integrating sphere (picture by Bengt Götesson, 2007).

The reference reading is thus[35].

$$S_o = \left[\frac{I_s R_b}{I_r R_b}\right] A_f \qquad 4.1$$

Where I_s and I_r are the intensities of the sample and reference beams respectively. R_b is the reflectance of the reference $BaSO_4$ and the sphere wall and A_f is the amplification factor of the instrument. When the reference $BaSO_4$ is replaced by the actual sample, the signal reading becomes

$$S_r = \left[\frac{I_s R_{sample}}{I_r R_b}\right] A_f . \qquad 4.2$$

The reflectance of the sample is obtained from the ratios of equations 4.1 and 4.2 as

$$R_{sample} = \left(\frac{S_r}{S_o}\right) R_b . \qquad 4.3$$

The reflectance of the $BaS0_4$, R_b is usually known.

4.5.2 Signal Analysis in an Integrating Sphere

In figure 4.5, we show the behaviour of the reflected signal in the reflectance mode of the integrating sphere.

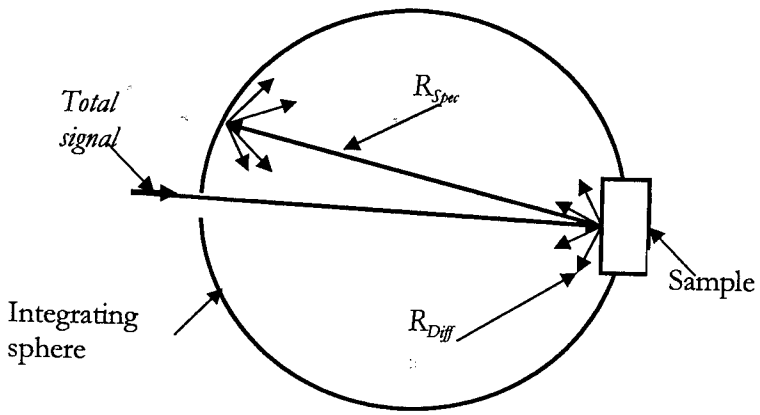

Figure 4.5: Schematic diagram of an integrating sphere showing the reflectance mode of the specular and diffuse reflection from a sample.

Generally, two signals are measured from an integrating sphere. The total reflectance is obtained when the specular reflectance hole is closed and the

diffuse reflectance is measured when the specular reflectance port is open. The total reflected signal R_{Total} comprise the diffuse reflectance (R_{Diff}) and the specular reflectance (R_{Spec}) written as

$$R_{Total} = R_{Diff} + R_{Spec}\ , \qquad 4.4$$

where $R_{Diff} = R_{ref} \times R_{Diff}(signal)$ and R_{ref} is the reference signal measured by the instrument.

Chapter 5

PHOTOVOLTAIC SYSTEMS

5.1 Introduction

Photovoltaic power generation is achieved through the use of solar cells made from suitable semi-conductor materials like silicon, germanium, gallium arsenide and copper indium diselenide. A group of solar cells form a module, a group of modules form an array and a group of arrays make a field. Solar cell modules are connected in series to increase the voltage and connected in parallel to increase the current. Silicon solar cells have shown efficiencies of about 18% and compounds of gallium[37] have efficiencies of about 27%. Efficiencies as high as 50% have been reported[38] for more advanced systems. The efficiency of the silicon solar cell decreases by about 0.5% per degree rise in temperature[38]. In a module string, it is the solar cell with the lowest junction current that determines the power output of the module. Hence, only identical solar cells need be connected together to produce a module with high efficiency.

5.2 The Photovoltaic Effect and Solar Cell Transport

Semiconductor materials such as silicon (Si), gallium arsenide (GaAs) and cadmium telluride (CdTe) are efficient absorbers of Sun's energy. Most commercially available photovoltaic devices today are fabricated from silicon. Silicon, with band-gap of 1.12eV (intrinsic) can effectively use only the wavelengths range of about 400-1100nm[39,40]. It has been shown[41,42] that silicon with this band-gap energy is not optimal. When a small amount of phosphorus (group V) is doped with silicon, a region of excess electrons called n-type is formed and when doped with boron (group III), a region deficient of free electrons (holes) called the p-type is formed. When the p-type and the n-type regions are joined together, we form a p-n junction as shown in figure 5.1. The energy required to raise a charge carrier from the valence band with energy E_V to the conduction band at energy E_C is called the band-gap energy E_G. The doping process effectively reduces the amount of energy required to raise an electron from the valence band to the conduction band due to the presence of donor states below the conduction band and the presence of acceptor states above the valence band.

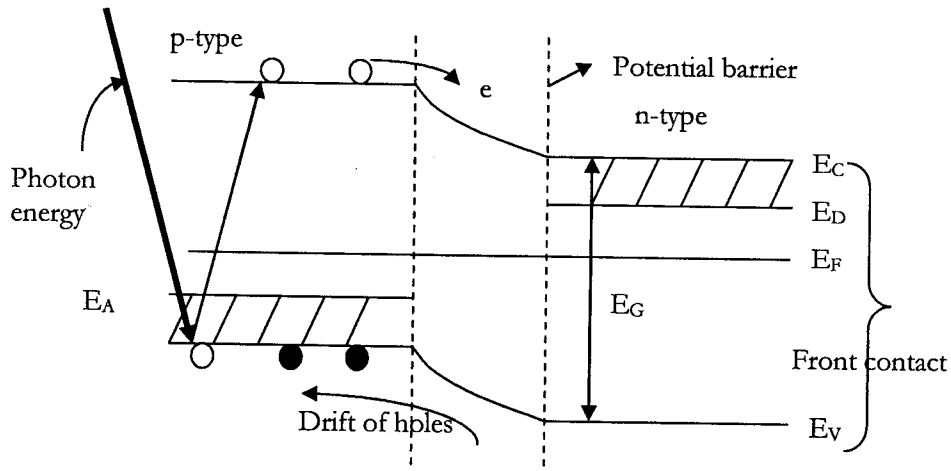

Figure 5.1: Photo-current is generated when a photon of sufficient energy creates electron-hole pairs in a semi-conductor material.

A lot of research has been done to explore materials with band-gap energies comparable to the solar spectrum[40,41,43]. Semi-conductor materials such as GaAs and CdTe with band-gaps nearer to 1.5eV, have higher theoretical efficiencies than silicon with intrinsic band-gap energy of 1.12eV[44] because they are direct band-gap semi-conductors. Thus, a photon alone creates an electron-hole pair unlike in silicon where an extra phonon is required to create an electron-hole pair. When photons of suitable energy (band-gap energy) fall onto the semi-conductor, electron-hole pairs are created. If the electron-hole pairs are formed near to the p-n junction, the charge carriers are separated by the presence of the internal electric field. The electrons drift into the conduction band (n-side) where they are the majority carriers and holes are

swept into the valence band where they are also majority carriers. If the concentration of electrons in the n-type is increased, the concentration of holes in the p-type also increases. Thus, an electrical voltage builds up. If the n-type and p-type are biased or connected say by an ohmic resistor, electrons flow through the connection to constitute a current. This current will continue as long as the incident light is available.

5.3 The Equivalent Solar Cell Circuit

The photon generated current I_L (photocurrent) is linearly dependent upon the light flux falling on the solar cell and is a measure of the short circuit current I_{sc}. It is easy from figure 5.2 and using Kirchhoff's junction law to see that the overall cell current I may be written as

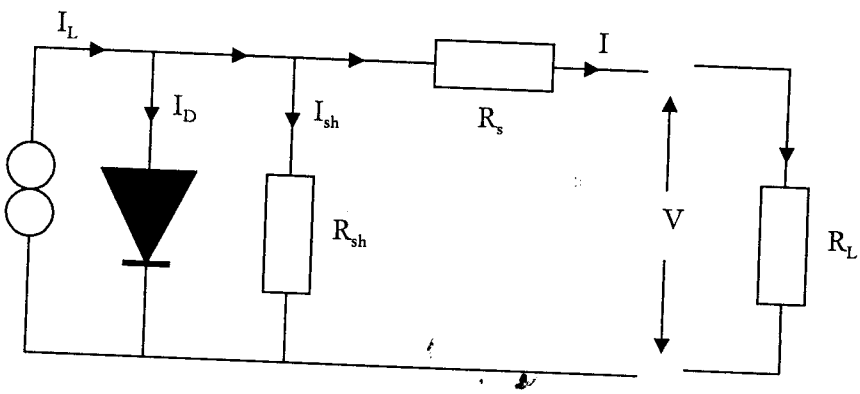

Figure 5.2: The equivalent solar cell circuit

$$I = I_L - I_D - I_{sh}\ , \qquad 5.1$$

where,

$$I_D = I_o\left(\exp\left(\frac{q(V + IR_s)}{BkT}\right) - 1\right), \qquad 5.2$$

is the diode current characteristics, B is the ideality factor, k is the Boltzmann constant, T is the absolute temperature, q is the electronic charge, I_o is the dark or diode saturation current and V is the applied voltage. In the short-circuit mode, the load resistance (R_L = 0) is zero and the output voltage is also zero. This means that no current flows through the diode (I_D = 0) and hence all the generated current flows to the output. Thus

$$I = I_L = I_{sc}. \qquad 5.3$$

However, for an infinitely large load resistance (open circuit mode), the output current (I = 0) is zero and the entire generated current flows though the internal diode. The open circuit voltage may be obtained from equation 5.2 above as[44,45]

$$V_{oc} = \frac{BkT}{q}\ln\left(\frac{I_L}{I_o} + 1\right). \qquad 5.4$$

We observe from equation 5.4 that the open circuit voltage is temperature dependent and the dependence of the open circuit voltage on temperature is shown in figure 5.3.

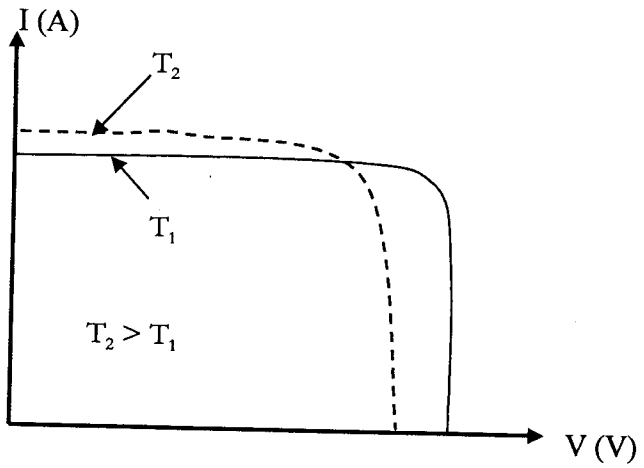

Figure 5.3: Effect of temperature on the module output. (after S.R Wenham[44], 1994)

5.4 Characteristic Resistances of Solar Cell Modules

The electric current generated in the semiconductor flows through the contacts at the front and at the rear of the solar cell. The solar cell is covered by a thin layer of dielectric material and the anti-reflecting coating to reduce reflections from the top surface. The overall series resistance of the cell R_s is composed mainly of the bulk p-type and n-type materials (R_{bp} and R_{bn}), and that of the contact resistance of the p-type and n-type materials (R_{cp} and R_{cn}) respectively. We may write for the overall series resistance as[13]

$$R_s = R_{cp} + R_{cn} + R_{bp} + R_{bn}. \qquad 5.5$$

The value of the series resistance must be as low as possible (R_s = 0, theoretically) as shown in figure 5.4.

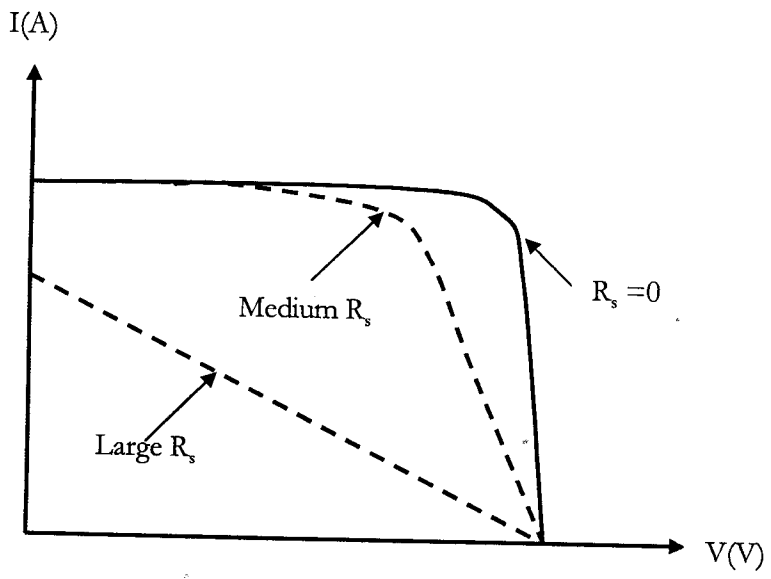

Figure 5.4: The effect of series resistance on the fill factor, (after S.R Wenham[44], 1994).

The other characteristic resistance of the solar cell is the shunt resistance R_{sh}. This is due to the leakage current at the junction and is dependent upon the junction fabrication technologies. The value of the shunt resistance needs to be very high ($R_{sh} = \infty$, theoretically) as shown in figure 5.5. The overall effect of the characteristic resistances is to reduce the fill factor of the solar cell module.

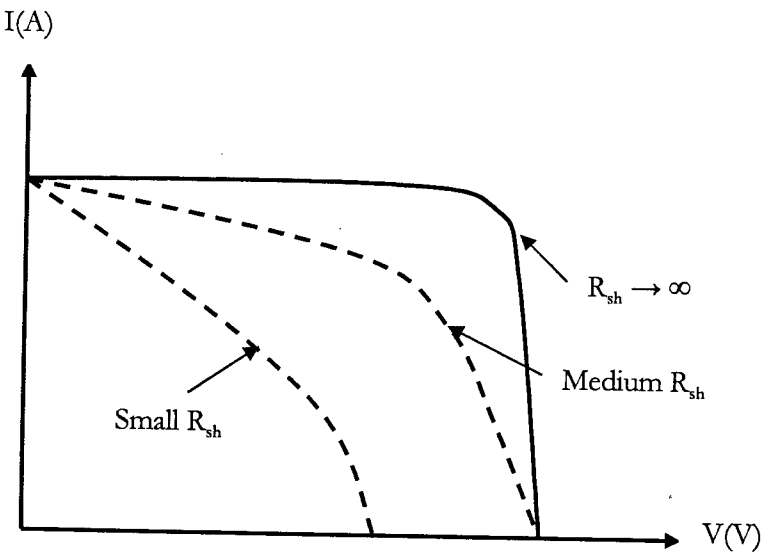

Figure 5.5: The effect of shunt resistance on the fill facto, (after S.R Wenham[44], 1994).

5.5 Fill Factor Dependence of Effective Series Resistance

It can be shown that there is always a potential drop across the module due to inherent series resistance of the module as shown in figure 5.6. The voltage drop is given by I_m x R_s and hence the corresponding fill factor may be written as

$$FF \approx \frac{I_m}{I_{sc}}\left[1 - \frac{I_m R_s}{V_{oc}}\right]. \qquad 5.6$$

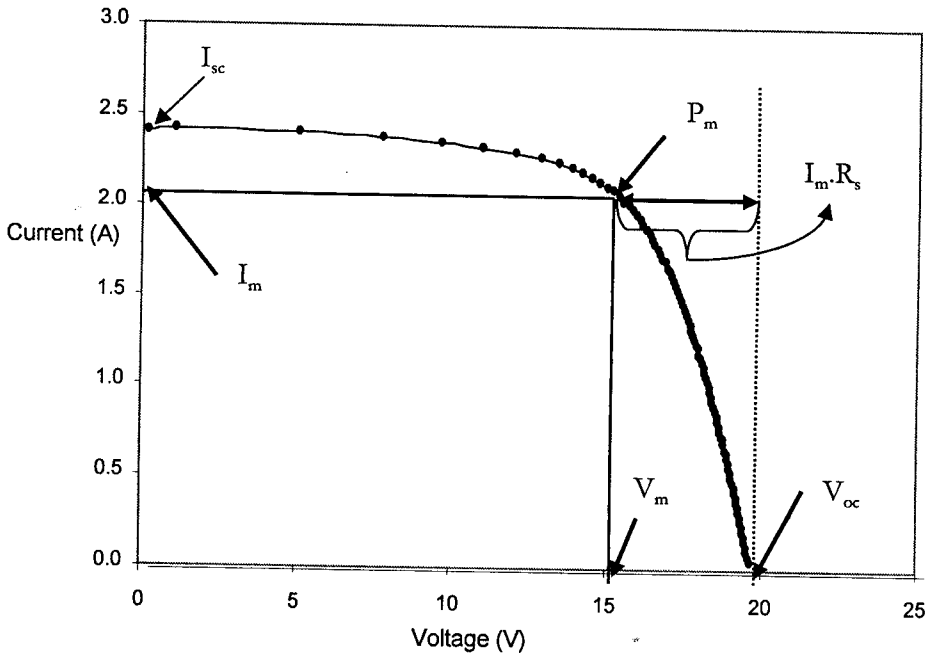

Figure 5.6: I-V curve for a 50W_p module (BP Solar model 140) with five output parameters.

To close approximation ($I_m \approx I_{sc}$ *c.f. figure 5.6*), the fill factor of a module may be approximated as

$$FF \approx 1 - r_s, \qquad 5.7$$

where $r_s = \frac{R_s}{R_{CR}}$ is the effective series resistance of the module, R_{CR} is the characteristic resistance equal to the ratio of the open circuit voltage and the short-circuit current[44].

5.6 Effect of Radiation Intensity on Module Output

The operating temperature of the solar cell above ambient is roughly proportional to the intensity of the incident radiation, provided that wind speed is not excessive[39] as shown in figure 5.7.

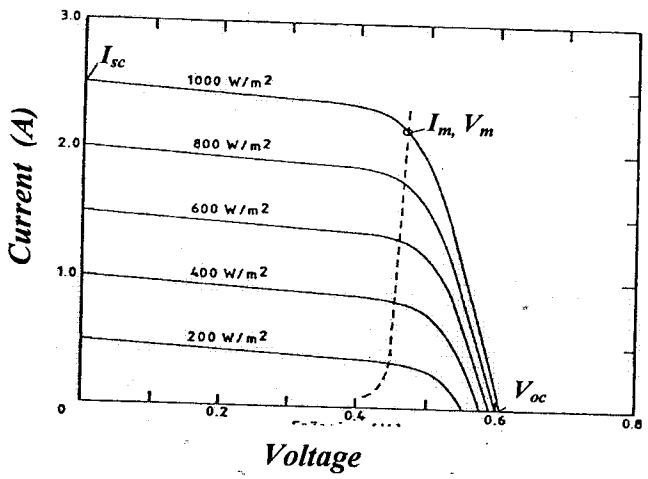

Figure 5.7: I-V characteristics for different levels of solar radiation intensities, (after Duffie and Beckman[1], 1991).

5.7 The Economics of Photovoltaic System

To be widely used, photovoltaic electricity must be competitive with those of conventional forms of electricity such as hydroelectricity[17,46]. In 1978, the total cost of photovoltaic system was in the range of 30 – 50 Euros per watt[47,48]. Today the price of hydroelectricity is about 6-7 cents per kilowatt-

hour and that of photovoltaic electricity is about 20-30 cents per kilowatt-hour; therefore the prices must come down by about a factor of 5 to compete favourably with bulk electricity market. Large scale solar electrical energy generation will become more competitive when the prices of photovoltaic cells reduce to 10 cents per kilo-watt-hour[46] and in the range of 6-8 cents per kilo-watt-hour for concentrator PV systems[17]. It is also projected that by 2020, the costs for concentrator systems are likely to drop to 6-7 cents per kilo-watt-hour[49].

The major challenge in solar concentrator systems is to efficiently reduce the costly solar cell material by using low cost reflecting or refracting elements. This could be achieved by finding an optical and ingenious collector design that could cost less than the solar cell area it replaces. Presently, the solar cell module cost dominates the photovoltaic system cost[17]. Since the reflector or lens material is often far less expensive than the semi-conductor material used in fabricating solar cells, the cost of module electricity could be greatly reduced.

Chapter 6

METHODOLOGIES AND EXPERIMENTAL TECHNIQUES

6.1 Introduction

The amount of solar radiation on a tilted surface depends upon the intensity of the solar radiation, the angle of tilt, the orientation of the surface, the type of collector used, the time of the day, the time of the year, and the geographical location of a place. In this chapter, we measure the collectable energy on a tilted surface and also investigate the performance of a photovoltaic system under low concentration by using structured aluminium reflectors. We further compare the effective reflectance of samples from short-circuit current measurements and ray-tracing. Finally, we study the performance of a large parabolic reflector in terms of its fill-factor profile and the associated degradation effects of six commercial reflectors to natural environment.

6.2 Collectable Energy on Tilted Surface

One way of increasing solar radiation on a collector is to tilt the collector towards the Sun. The annual collectable solar energy on a tilted surface for Lusaka was measured using solar sensor model Si-420TC shown in figure

6.2(a) during the period August 1st 2002 to December 31st 2003. The calibration factor of the instrument was 20mA to represent 1200 W/m^2. The sensor was mounted on an adjustable frame and tilted at 25° to the horizontal. The instantaneous solar radiations were recorded for the whole day at one second interval and averaged over thirty minutes by a data-logger program.

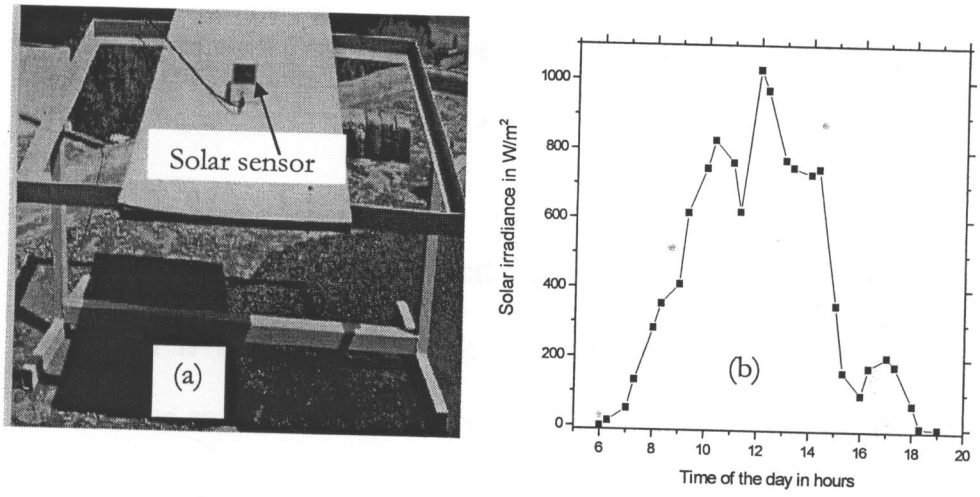

Figure 6.1: The solar *sensor (a) mounted at a fixed tilt of 25° to the horizontal and (b) a day's output for 4th February 2003. The area under the curve gives the total collectable energy on this particular day.*

The daily solar radiations were downloaded. Figure 6.1(b) shows a typical day's output for February 4, 2003. The daily data collection period lasted for

seventeen (17) months. The area under the irradiance-time graph gave the total solar energy received on a unit-area per day in $Whm^{-2}day^{-1}$.

The daily average in a month gave the monthly mean solar energy in $kWhm^{-2}day^{-1}$ and the peak sun hours (PSH) were computed from the ratio of the total area under the curve to the solar intensity of $1000W/m^2$. The monthly mean energies on a tilted surface were compared with National Aeronautics and Space Administration (NASA)[50] results.

6.3 Evaluation of the Projected Beam Solar Energy

Meteonorm is a meteorological database of the globally simulated solar radiations on any oriented surface based on more than 10 year averages. The simulation calculations were performed by TRNSYS (TRaNsient Systems Simulation) program developed at the Solar Energy Laboratory – University of Wisconsin, Madison[51]. However, in this thesis we used WINSUN program[52] which is an extraction from the TRNSYS program. If H_b (obtained from Meteonorm) is the incident beam radiation from the Sun onto a concentrator, the component of the solar radiation ΔH_{bp} incident from the North at a projected angular height θ_p above the horizontal during time interval Δt is given by[53]

$$\Delta H_{bp} = H_b \cos \varepsilon \Delta t . \qquad 6.1$$

The term $cos\,\varepsilon$, is obtained from equations 2.3 and 2.4 of chapter 2 and ε is the angle between the Sun ray vector and its projection on the North-South plane. The projected solar height angle θ_p is calculated from equation 2.5.

6.4 Simulated Output from Different Tracking Modes

Winsun software[52] was used to calculate the monthly global solar radiation for Lusaka station under different tracking modes of a solar collector based on the meteonorm database. We further simulated the yearly global solar radiations for the selected Zambian stations at different tracking modes. The different tracking modes were horizontal tilt (horizontal surface), latitude tilt, North-South tracking (East-West axis), East-West tracking (North-South axis), and two axis tracking. The selected Zambian stations, latitude in brackets, were Nakonde (9.3°), Kasama (10.2°), Mansa (11.2°), Mwinilunga (11.8°), Solwezi (12.2°), Ndola (13.0°), Chipata (13.6°), Mongu (15.2°), Lusaka (15.4°), Monze (16.2°), and Choma (16.8°).

6.5 Surface Reflectance of Rolled Aluminium Samples

6.5.1 Optical Properties

The Perkin Elmer Lambda 900 spectrophotometer at Ångström Laboratory in Uppsala, Sweden (Figure 4.3) was used for sample characterization. The

instrument was calibrated by scanning a reference sample each time a new set of measurements were made. The sample was put at the exit port of the integrating sphere. The total reflectance (*TR*) was measured when the specular port of the integrating sphere was closed and the diffuse reflectance *(DR)* was measured when the specular port was open. The specular reflectance *(SR)* component was obtained by subtracting diffuse from total reflectance. The analyzed samples are shown in figure 6.2.

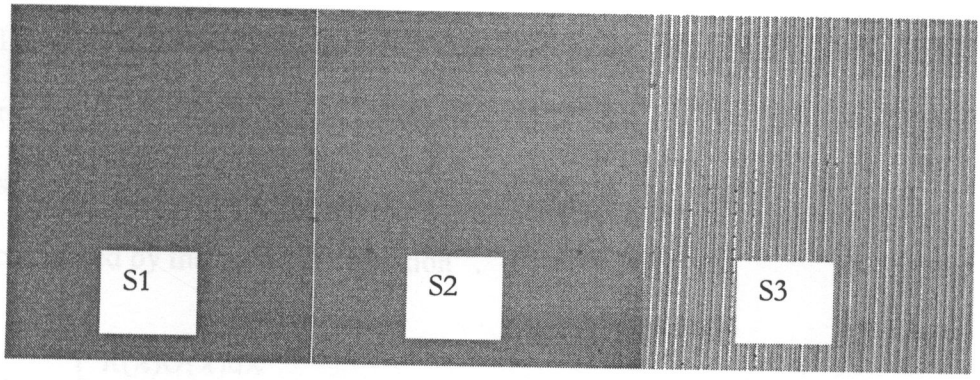

Figure 6.2: Different diffuse aluminium sheets. S1 is the diffuse aluminium with small rolling marks, S2 is a plane diffuse aluminium with no rolling marks, and S3 is the diffuse aluminium with large rolling marks.

Sample I (S1) was a diffuse aluminium sample with small rolling grooves on one side. Sample II (S2) was a plane aluminium sample (diffuse) without rolling grooves on both sides. Sample III (S3) was a diffuse aluminium

sample with large rolling grooves on one side. The samples were cleaned using ultrasonic bath in ethanol solution to remove any grease. The dust particles were removed by blowing in dry nitrogen gas. The total reflectance and the diffuse reflectance were measured at groove orientations of 45°, horizontal (90°) and vertical (0°) to the plane of the exit hole of the integrating sphere.

6.5.2 Computation of Weighted Spectral Reflectance

If $R(\lambda)$ is the wavelength-dependent property of a material such as responsivity, transmittance, reflectance, absorptance, and $G(\lambda)$ represents the solar spectral irradiance, the mean value R_m of the property $R(\lambda)$ may be calculated by the following equation[54].

$$R_m = \frac{\int_0^\infty R(\lambda)G(\lambda)d\lambda}{\int_0^\infty G(\lambda)d\lambda}. \qquad 6.2$$

Since the spectral property and the spectral irradiance are usually known at discrete values of the wavelength, the integration is performed as a summation, so that equation 6.2 becomes

$$R_m = \frac{\sum_{300nm}^{2500nm} R(\lambda)G(\lambda)\Delta\lambda}{\sum_{300nm}^{2500nm} G(\lambda)\Delta\lambda}. \qquad 6.3$$

Hence, the quantitative differences among samples were calculated in terms of their total integrated reflectance *(TIR)*, their diffuse integrated reflectance *(DIR)* and their specular integrated reflectance *(SIR)* using equation 6.3.

6.6 Effective Specular Reflectance and Ray-Tracing

6.6.1 Tailor-made CPC for Material Testing

The standard polar co-ordinate system proposed by Welford and Winston[20] was used in the design of the compound parabolic concentrator. The x and y co-ordinates were respectively derived from[20]

$$x = \frac{2f\sin(\phi_a - \theta_c)}{1-\cos\phi_a} - a, \qquad 6.4$$

$$y = \frac{2f\cos(\phi_a - \theta_c)}{1-\cos\phi_a}, \qquad 6.5$$

where $f = a(1+\sin\theta_c)$ is the focal length of the CPC, a (= $A_a/2$) is the half width of the exit aperture (50 mm in our case, half width of module) and θ_c is the acceptance half angle of the CPC (15° in our case, local latitude).

Figure 6.3 (b) shows the actual constructed Compound Parabolic Concentrator used for the current-voltage and flux distribution profile measurements. For the purposes of ray-tracing, an identical CPC was generated from the standard parabola equation

$$y = \frac{x^2}{4f} - f \,. \qquad 6.6$$

The initial x-value of the CPC in the rotated x'-y' co-ordinate system was $2a$ and the initial y-value was determined when $x' = 2a$. The x-value at the top of the CPC was $\frac{2f}{1-\cos 2\theta_c}$ and the top y-value was obtained by substituting in equation 6.6.

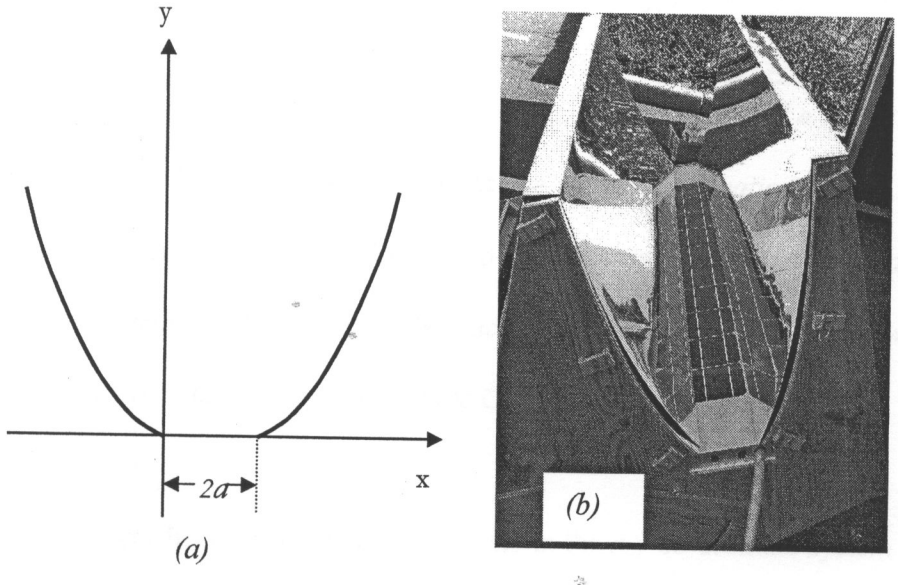

Figure 6.3: (a) The CPC designed from polar co-ordinates into the x-y co-ordinates system and *(b) the actual constructed CPC geometry.*

The new CPC in the rotated x'-y' co-ordinate system was transformed through an angle θ_c to bring it into the x-y co-ordinate system as shown in figure 6.4(a).

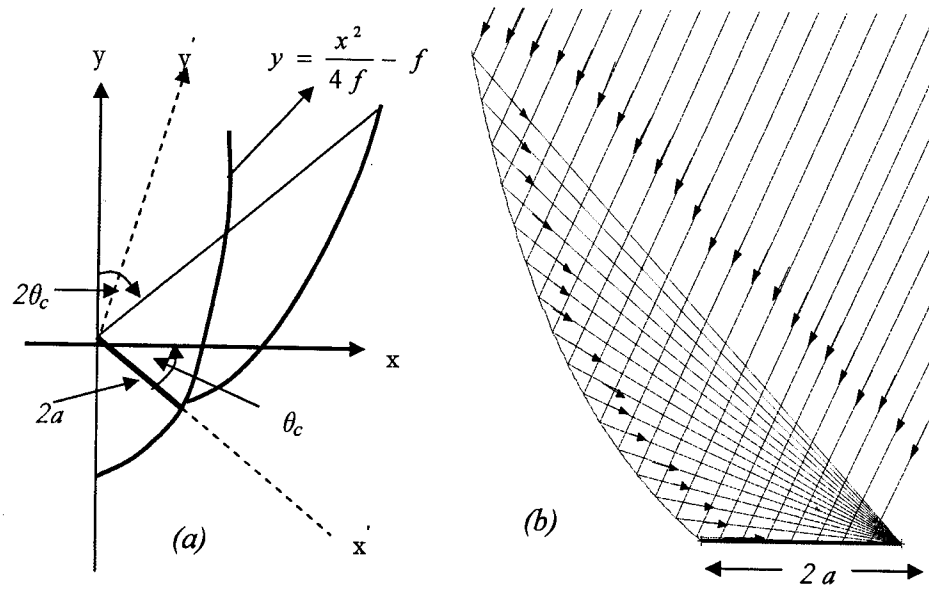

Figure 6.4 (a) Design of the CPC from the parabola equation in the x'-y' system and transformed into the x-y co-ordinate system, (b) a ray-traced portion of a truncated CPC at the half acceptance angle. (only 23 rays were sent through the entrance aperture of the CPC for clarity).

Rays were sent from the known co-ordinates in the *x-y* co-ordinate system but hit the intersection with the parabola in the *x'-y'* system and finally transformed back into the *x-y* co-ordinate system. The final and truncated symmetric CPC had an exit aperture 2a = 100mm and an entrance aperture of 358mm as shown in figure 6.3 (b). The theoretical maximum concentration ratio was $C = 3.86$.

6.6.2 Current-Voltage Measurements through a Relay

An Operational Amplifier (Op-Amp) was used to compare the voltage across an electronic load connected to the solar cell module and a control voltage from the data logger. When the voltage over the electronic load was higher than required, the current through the power transistor increased and caused reduction on the voltage over the electronic load and finally the measuring point on the I-V curve shifts towards lower voltage. The schematic drawing of the electronic load is shown in figure 6.5. The logger produced excitation voltages up to 2.5V to measure high voltages by using a potential divider (1:10). Lower voltages were measured by moving the potential divider towards smaller voltage values. The current was measured by a four terminal shunt resistance of 0.01Ω as shown in the figure. The tolerance of the resistor was ± 1% so that the voltage drop across the two conducting wires did not affect the voltage across the other two wires. The maximum power was about 2W and allowed a 14A continuous current through the resistor. During short-circuit measurements; the reduction in the resistance was achieved by using a relay. When the relay closed, most of the current went through the switch. The internal resistance was further reduced by shortening the connecting wires between the relay and the shunt resistance.

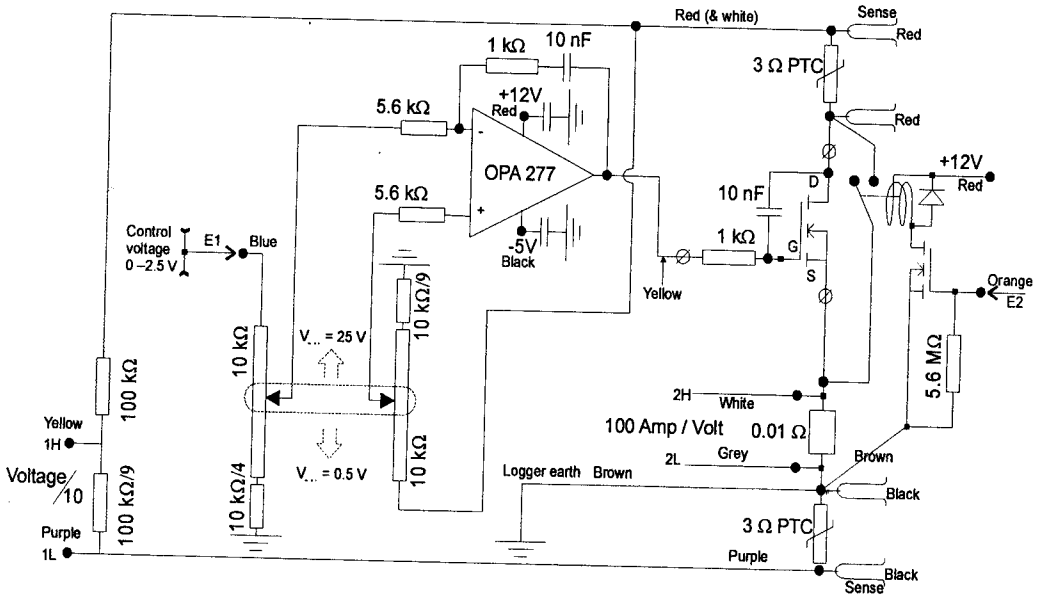

Figure 6.5: Schematic circuit of an electronic load for I-V curve measurement, (courtesy of Johan Nilsson[55], 2005).

6.6.3 Flux Distribution Profile Measurements

The flux distribution apparatus[55] measures the amount of solar flux on the base of the CPC. It was made and used at the Lund University laboratory and later carried to the Physics Department of the University of Zambia. It consists of a 12V d.c motor connected to a potentiometer and attached to the central wiper with a photo-diode as shown in figure 6.6. The actual set-up of the flux

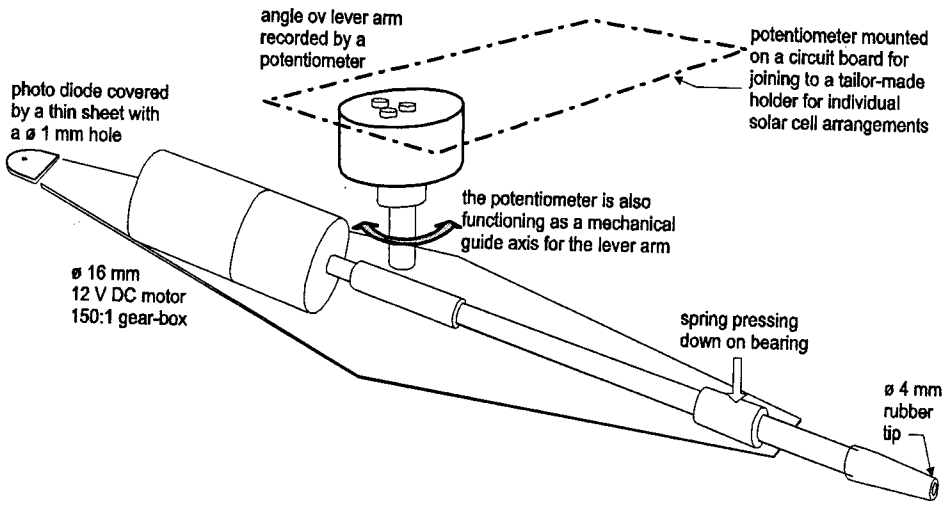

Figure 6.6: Schematic arrangement of the flux distribution apparatus constructed at Lund University.

distribution apparatus is shown in figure 6.7. The motor was calibrated to convert its angular rotations into linear motion across the width of the module. The photo-diode, the solarimeter and the reference diode were all connected to the data-logger. The data-logger was programmed to record 240 data points in one minute. The good resolution on each reading was achieved by using a 1mm diameter photo-diode (arrow in figure 6.7). The reflector material used as the base in the CPC was anodized aluminium (Al_2O_3) and simply replaced the miro ($TiO_2/SnO_2/Al$) and the aluminium foil in the flux distribution measurements. The local concentration ratio (C_L) was measured as function of

the module width. The simulated results from commercial Zemax Software[56] and the experimental short-circuit current results were compared.

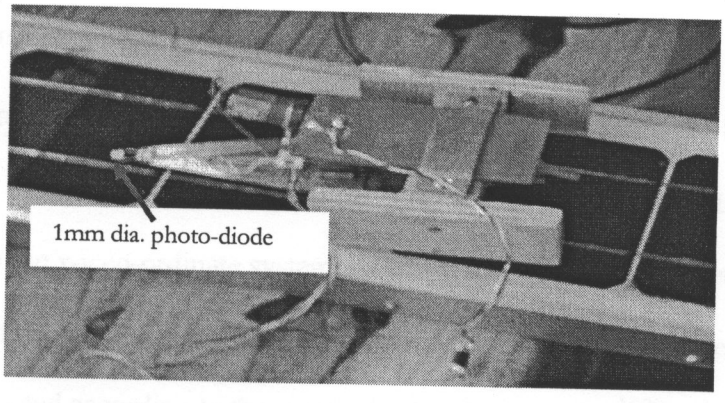

Figure 6.7: Set-up of the flux distribution profile apparatus on the module inside the CPC.

6.6.4 Ray-Tracing Techniques

The purpose of ray-tracing is to analyze the optical characteristics of an optical system in terms of the rays that are intercepted by the entrance aperture and those that reach the exit aperture of the CPC. Since the incoming flux are represented by finite number of equally spaced rays in geometrical optics, we define the local concentration ratio (C_L) as the ratio of flux density reaching the absorber to those intercepted by the entrance aperture of the CPC. Rays were sent from known points on the *x-y* co-ordinate system and found their

intersection on the x'-y' co-ordinate system through a transformation equation (anticlockwise) given by

$$x' = x\cos\theta_c - y\sin\theta_c$$

$$y' = x\sin\theta_c + y\cos\theta_c . \qquad 6.7$$

The intersection was found from solving the equation of a straight line and the equation of a parabola. The co-ordinates of the intersection were transformed back into the x-y co-ordinate system. At this stage, we checked whether the ray hit the reflector or hit the absorber or missed. If the ray hit the reflector, it had to be reflected according to the standard reflection equation[16,20] as

$$\hat{r} = \hat{i} - 2(\hat{i}\,.\,\hat{n})\,\hat{n} . \qquad 6.8$$

The process was repeated by sending a large number of rays into the CPC and finally took statistics of rays that hit the absorber directly or after reflection and those that missed. From the statistics, the effective specular reflectance R_{eff} was calculated from the proposed equation 6.9. Note that equation 6.9 was tested only at normal incidence.

$$\frac{C_L}{C_g} = f_0 + f_1 R_{eff} + f_2 R_{eff}^{\ 2} + \ldots\ldots , \qquad 6.9$$

where f_0 was the fraction of the solar flux that hit the absorber directly, f_1 was the fraction of the solar flux that hit the absorber after a single reflection, f_2 was the fraction of the solar flux that hit the absorber after second reflection and R_{eff} was the effective specular reflectance of the reflector used. The left-

hand side of equation 6.9 was obtained from the flux distribution measurements.

6.7 Testing of Copper Indium Selenide (CIS) Modules under Low Concentration

6.7.1 CPC Specifications

The truncated CPC with a half acceptance angle of 15° was constructed as in section 6.6.1 above. The length and the height of the truncated CPC were 60cm and 58.8cm respectively. The exit and entrance aperture width of CPC were 15cm (total width of the CIS module) and 50.2cm respectively, giving the geometrical concentration ratio of 3.35. The CPC was made long enough to minimize edge effects as shown in figure 6.8. The length and the width of the CIS module were 30cm and 15cm respectively. The total area of the CIS module was $0.045m^2$ and the active area of the module was $0.036m^2$. Two reflector materials (a) specular and (b) diffuse (Fig. 6.8) were inserted alternately in the CPC and a series of I-V curves were obtained in each case.

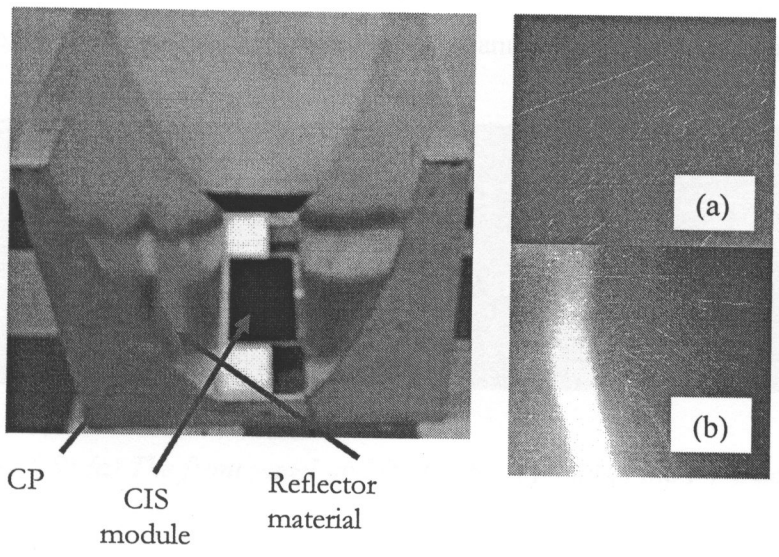

Figure 6.8: CIS module inside the CPC. (a) specular and (b) diffuse reflector materials used in the CPC.

6.7.2 Current-Voltage (I-V) Tracker Instrument

A current-voltage tracker instrument was obtained from Vattenfall, Sweden, through the financial assistance of the International Science Program (ISP) of the Uppsala University. It consists mainly of a power supply, an I-V plotter, and data-logger components. It was powered by a 9V dc and the physical features are shown in figure 6.9. The two red terminals were connected to the positive terminal of the module and the two black terminals were connected to the negative terminal of the module. The instrument recorded one hundred data points of current and voltage in three to four seconds and these

instantaneous measurements were downloaded onto the computer through the HyperTerminal software provided by the manufacturer. The short-circuit

(a) (b)

Figure 6.9: (a) The front panel and (b) the back panel of the I-V tracker.

current I_{sc}, the open-circuit voltage V_{oc}, the maximum power P_m, the current I_m and the voltage V_m at maximum power point respectively were extracted from each I-V curve. Finally the fill-factor *(FF)* was evaluated from equation 6.10.

$$FF = \frac{P_m}{I_{sc}V_{oc}}. \qquad 6.10$$

The efficiency of the solar cell module could be also calculated from

$$\eta_e = \frac{I_{sc}V_{oc}FF}{I_N A_m}, \qquad 6.11$$

where I_N is the instantaneous solar radiation incident on the solar cell module of active area A_m. Hence, for each type of material, specular and diffuse, I-V curves were obtained at each angle of incidence.

6.7.3 Optical Properties of Specular and Diffuse Reflectors

The optical properties of the diffuse (rolled aluminium foil) and specular (evaporated aluminium, laminated on plastic) reflectors were obtained from the Perkin Elmer spectrophotometer lambda 900 at Ångström laboratory. In particular, the total reflectance and the diffuse reflectance for the diffuse material were obtained from the instrument and the specular reflectance was obtained by subtraction. The same was done for the specular material and for the horizontal grooves *(HG)* and for the vertical grooves *(VG)* of the diffuse material. The total integrated reflectance *(TIR)*, diffuse integrated reflectance *(DIR)* and specular integrated reflectance *(SIR)* were all calculated from equation 6.3.

6.8 Construction and Testing of a Large Parabolic Reflector

6.8.1 Construction Procedures

A parabola is a locus of points in a plane that are equidistant from a given fixed point called the focus F and a fixed line called the directrix D[57] shown in figure 6.10. If the focus does not lie on the directrix, then we may choose a co-ordinate system that result in a simple equation for the parabola. If the distance between F and D is $2f$, we may assign F co-ordinates as (0, f) and the equation of D as $y = -f$. Hence, a point P will lie on the parabola if and only if the distances PF and PQ are equal. Thus, from figure 6.10 we have

$$PF = \sqrt{x^2 + (y-f)^2} \quad \text{and} \quad PQ = \sqrt{(y+f)^2}\,. \qquad 6.12$$

Simplification of the above expressions gives

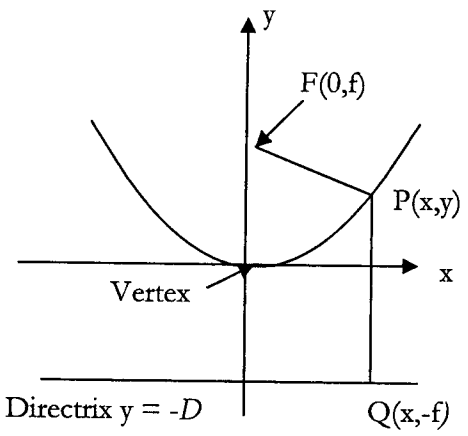

Figure 6.10: Co-ordinates of a parabola equidistant from a point F and a directrix D.

$$x^2 = 4fy. \qquad 6.13$$

The usual mathematical form of equation 6.13, whose vertex is at the origin, is

$$y = \frac{x^2}{4f}. \qquad 6.14$$

The focal length *f* of our large parabolic reflector was 40cm, the total extended length along the North-South direction was 200cm, and aperture length from the focus was 97.1cm. The parabolic reflector shown in figure 6.11 was constructed in Sweden. However, the bottom support and the rails were assembled at the metal workshop of the University of Zambia. The parabolic

reflector was manually tracked by turning the shaft clockwise or counterclockwise to bring the line focus to a desirable position on the solar cell module.

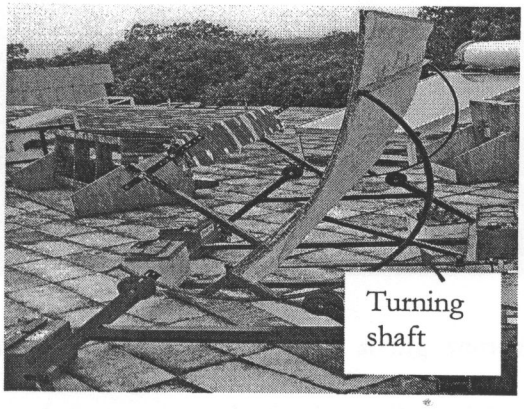

Figure 6.11: Picture of the parabolic reflector showing the eight cell module covered in protective polythene to avoid excess heating when not in use.

6.8.2 Short-Circuit Current and Fill-Factor Measurements

The short-circuit current of a photovoltaic module in a concentrated system depends only on the irradiance on the module at a constant temperature and is determined by the optical efficiency of the concentrator system[58,59,60]. The flux concentration ratio[61,62] was estimated from the high resistance solarimeter. The parabolic reflector was manually tracked along the North-South axis by means of a lever-arm shaft. The reflected rays formed a line focus which swept across the module as shown in figure 6.12. A current-voltage curve was

obtained at each position of the line focus using the standard I-V tracker instrument mentioned in section 6.7.2.

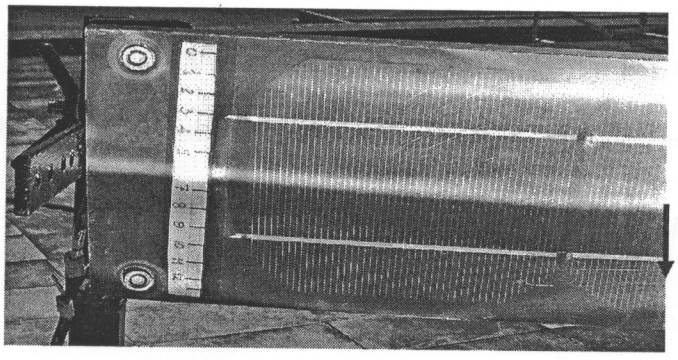

Figure 6.12: Part of the eight cell module string showing the line focus passing the 6cm mark from one end of solar cell module (line focus moved from top to bottom as indicated by an arrow).

Firstly, we had to estimate the concentration ratio and the optical efficiency of the large parabolic reflector. This was done by obtaining I-V curves when the solar cell module was outside the parabolic reflector and placed perpendicular to the sun rays (normal incidence). These were the reference measurements. The other I-V curves were obtained when the solar cell module was in focus with the reflected rays from the parabolic reflector (solar cell fully illuminated). The ratio of the short-circuit current under concentration to the short-circuit current without concentration was estimated from equation 6.15,

$$C_{opt} = \frac{I_{sc}^{conc}}{I_{sc}^{ref}}, \qquad 6.15$$

where I_{sc}^{conc} is the short-circuit current under concentration and I_{sc}^{ref} is the short-circuit current without concentration. The optical efficiency of the system may be calculated from equation 6.16, where C_g the geometrical concentration ratio of the concentrator system is defined as the ratio of the concentrator aperture area to the module area.

$$\eta_{opt} = \frac{C_{opt}}{C_g}. \qquad 6.16$$

The second set of measurements were for the distribution profiles of short-circuit current and fill factor as a function of the distance moved by the line focus across the width of the solar cell module. At each position of the line focus from 0cm to 12.5cm (width of solar cell), a series of I-V curves were obtained at 0.5cm intervals. A total of 26 data points each of which represented an I-V curve were plotted and similar I-V curves were also obtained when the line focus was moved from bottom to top. The two sets of results were compared.

6.8.3 The Effective Specular Reflectance Model

Since the theoretical optical efficiency of a CPC trough is well known[59], it is easy to show that effective specular reflectance ($R_{eff}^{<n>}$) of the reflector material

used on the large parabolic concentrator system may be obtained from equation 6.17.

$$I_{sc}^{conc} = \frac{I_{sc}^{ref}}{\gamma_i}\left[1 + C_g R_{eff}^{<n>}\right], \qquad 6.17$$

where $<n>$ is the average number of reflections (taken as unit for our system), and γ_i is the intercept factor defined as the ratio of the average intensity intercepted by the module inside the parabolic reflector to the average intensity intercepted by the reflector aperture. The intercept factor was obtained from the average intensities of irradiation on the module and on the parabolic reflector aperture using a solarimeter. Hence, the specular reflectance was calculated and compared with the spectrophotometer measurements.

6.9 Degradation Effects of Commercial Reflectors

6.9.1 Reflector Materials

An attempt was made to study the degradation effects of available commercial reflector materials used in solar concentrator systems. The main aim of the study was to identify a relatively durable reflector material(s) to withstand natural environmental conditions. In particular, we wanted to compare the specularity of the reflector materials before and after long-term exposure to natural environment. The six reflector materials were as follows:

Sample 1: Evaporated silver on aluminium, simply known as silver on aluminium.

Sample 2: Anodized aluminium; an oxide layer (Al_2O_3) forms on aluminium during anodization to improve the metal's corrosion resistance.

Sample 3: Miro; a commercially available thin film ($T_iO_2/S_iO_2/Al$) coated on aluminium sheet without surface protection.

Sample 4: Rolled aluminium; this is a lacquered rolled aluminium foil, laminated on plastic (polyethyleneterephthalate, PET) or mylar.

Sample 5: Evaporated aluminium on plastic and laminated on plastic.

Sample 6: Evaporated aluminium on steel.

6.9.2 Sample exposure

Each set of six materials measuring 6cm x 5cm were put into a transparent plastic box where only solar radiation was mainly received as shown in figure 6.13(a). The other set of six were exposed to the natural environment so that they experienced harsh conditions such as dust, humidity, contamination, etc as shown in figure 6.13(b). The third set of six were kept in an envelope as reference samples. The samples were initially exposed for about one year, thus from 22nd December 2005 to 31st December 2006. Typically, reflectance

measurements were to be done every after three months but the lambda 19 spectrophotometer at the home institution was broken down. Hence, the first

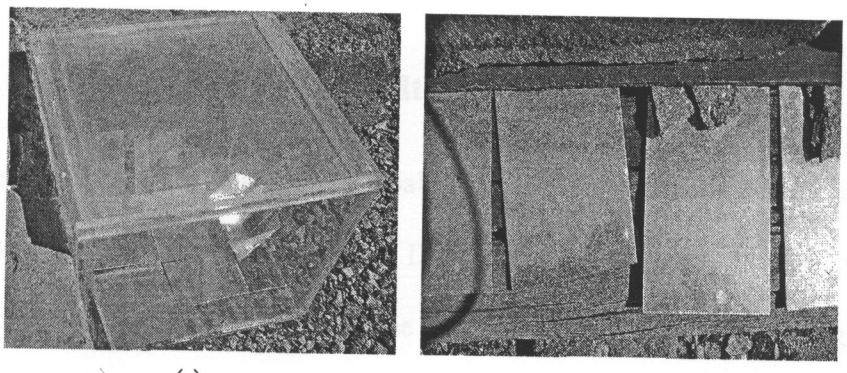

(a) (b)

Figure 6.13: (a) Samples kept into a transparent plastic box, dust collection on top of the box is evident, (b) part of the exposed samples to the natural environment, more collection of dust particles is seen.

round of measurements was done in Uppsala (Sweden) from 21st to 27th February 2007. The analyzed samples were re-exposed for another ten months in Lusaka from 23rd June 2007 to 21st April 2008. The second round of analysis of the samples was done in Uppsala from 25th to 30th April 2008 in Sweden. Thus, all the reflectance measurements were done on the Perkin Elmer spectrophotometer lambda 900 at Ångström laboratory of the Uppsala University in Sweden. The analysis of the reflectance results was done using the usual equation 6.3 and is presented in section 7.8.1.

Chapter 7

EXPERIMENTAL RESULTS AND DISCUSSION

7.1 Collectable Energy on Tilted Surface

Table 7.1 shows the measured global radiations on a horizontal surface I_h (column 2) from the Meteorological Department[63] in Lusaka, the measured global radiations on a tilted surface I_t (column 3), the calculated global radiations on horizontal surface I_h (column 4) from NASA[50] and the calculated global solar radiation on a tilted surface I_t (column 5) also from NASA. The peak-sun hours (PSH) on a tilted surface are shown in column 6 of table 7.1, and were estimated from the measured solar radiation on tilted surface shown in column 3. The peak-sun hour parameter can be used to estimate the energy output from a photovoltaic module oriented at an optimal tilt. For example, if the optimum tilt angle for the month of April is 25° and the peak-sun hours is 6.1hrs, the harvestable energy from a 50Wp module would be 305Wh/m^2 per day or 1.098MJ/m^2 per day.

Table 7.1: Measured global solar radiations on a horizontal surface I_h ($kWhm^{-2}day^{-1}$) and measured global solar radiations on a tilted surface I_t ($kWhm^{-2}day^{-1}$) and the corresponding peak-sun hours for each month.

Month	I_h (Met. Dept)	I_t Tilt 25° (Measured)	I_h (NASA[50])	I_t (NASA[50]) Tilt 30°	*PSH* (hrs)
Jan	4.94	5.11	5.07	4.76	5.1
Feb	4.36	4.53	5.09	4.51	4.5
Mar	5.11	4.69	5.37	5.13	4.7
Apr	4.89	6.06	5.69	6.07	6.1
May	4.94	6.22	5.05	5.93	6.2
Jun	4.72	5.25	4.92	6.11	5.2
Jul	4.72	5.67	5.14	6.26	5.7
Aug	5.58	6.03	5.87	6.60	6.0
Sep	5.92	5.94	6.67	6.70	5.9
Oct	5.89	5.81	6.80	6.10	5.8
Nov	5.39	5.58	6.08	5.67	5.6
Dec	4.94	4.61	4.99	4.72	4.6

7.2 North Projected Beam Irradiations for Lusaka

In figure 7.1, we show a typical annual cumulative time as a function of the North projection angle θ_p[61,64]. Thus, in the angular interval between 46° and 60° (around winter solstice) the Sun spends about 873hrs/yr and so is the period between 91° and 105° (around summer solstice). However, during the period between 68° and 83° (equinoxes) the Sun spends about 446hrs/yr. It may be concluded that the Sun spends more time at its winter and summer solstices as compared to the equinoxes. Note that figure 7.1 is typical of any other location on the globe.

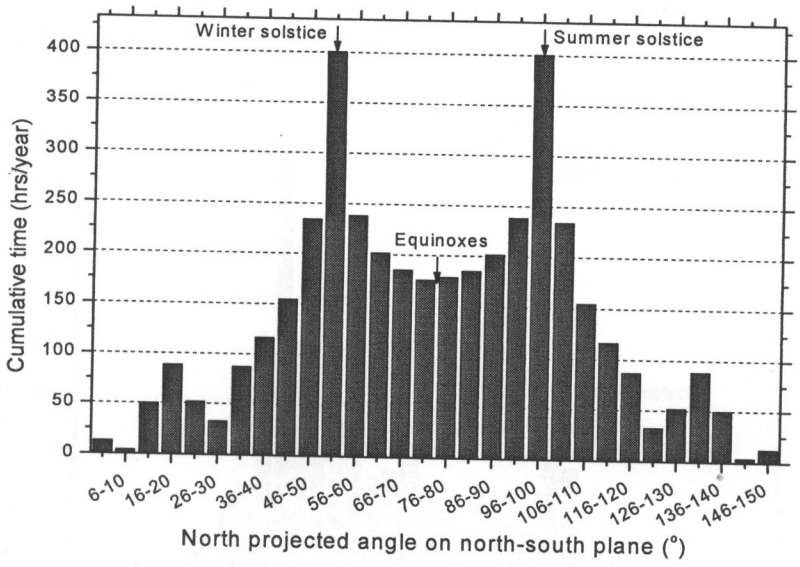

Figure 7.1: The cumulative time distribution as a function of the North projection angle for Lusaka at 5 degree angular interval.

In figure 7.2 we show the yearly beam energy for Lusaka projected in the North-South vertical plane as a function of the North projection angle θ_p[64]. From the figure, we see that most of the beam irradiation occurs during the winter months of May, June and July. The winter peak (June 23rd) has a yearly collectable beam energy of about 170kWh/m^2/yr in the angular interval 51-53°. The summer peak (December 23rd) has a contribution of about 76kWh/m^2/yr of the North projected beam energy in the angular interval 96-98°. During the equinoxes, (March 21st and September 21st) the contributions

of the North projected beam energy in the angular intervals 75-77° and 72-74° are about 59 and 47kWh/m^2/yr respectively.

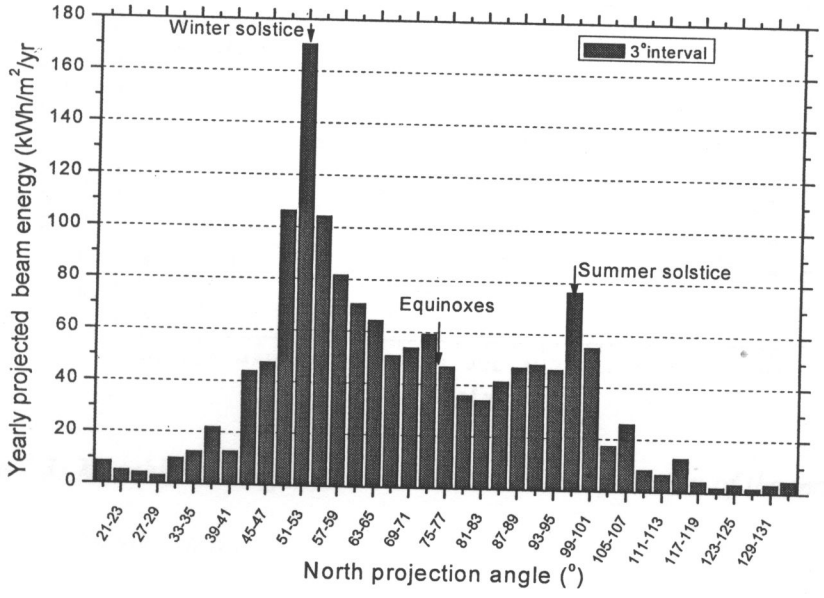

Figure 7.2: The yearly North projection beam energy distribution as a function of North projection angle for Lusaka at 3° angular interval.

7.3 Simulated Results from Different Tracking Modes

Figure 7.3 shows the simulated monthly output from different tracking modes for Lusaka station. We see that double axis tracking gives larger outputs as expected than the other tracking modes. The results were typical of the other stations.

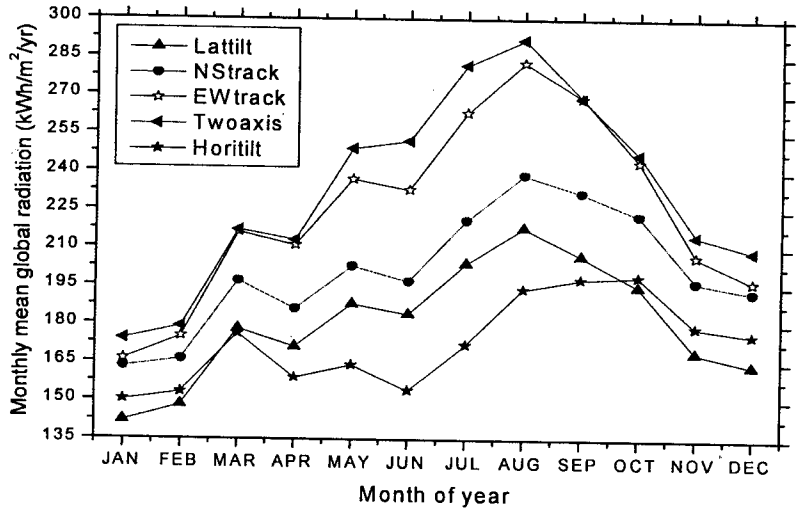

Figure 7.3: Monthly mean global solar radiation as a function of the month of the year for Lusaka station.

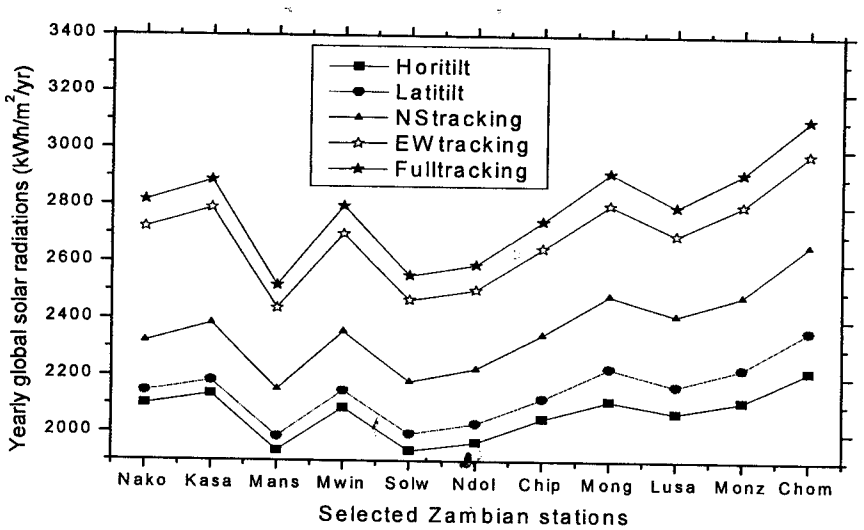

Figure 7.4: Comparison of the yearly global solar radiation for the different tracking modes for the selected stations in Zambia.

In figure 7.4, we show the yearly simulated global solar radiation for the selected Zambian stations for the different tracking modes. The stations are arranged in increasing latitude.

7.4 Optical Properties of Structured Samples

7.4.1 Comparison of Reflectance on Grooved Samples

Figures 7.5(a) and (b) show results of total reflectance and diffuse reflectance respectively for sample I (small grooves) with grooves oriented at 45°, horizontal and vertical. Horizontal and 45° gave more total and diffuse reflectance.

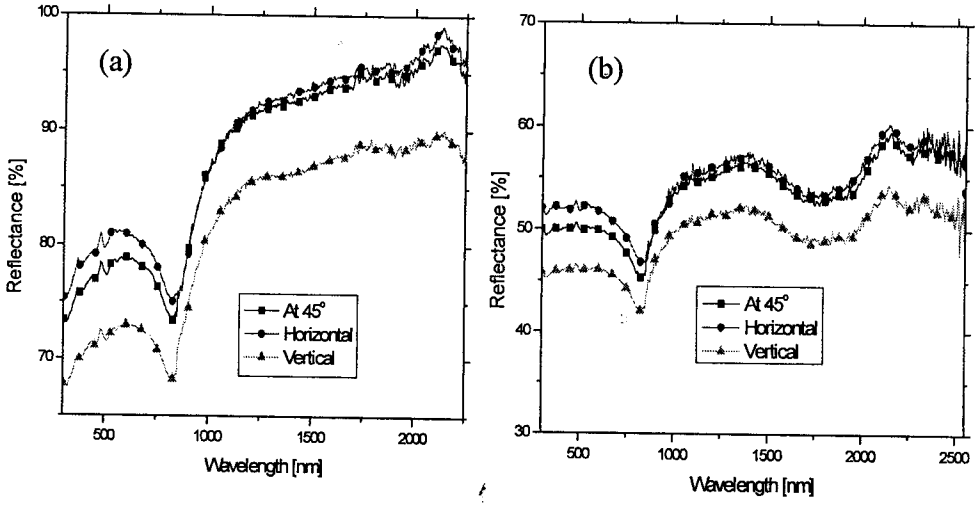

Fig. 7.5 : (a) Total reflectance, (b) diffuse reflectance curves for sample I.

In figures 7.5(c) and (d) we show the total and the diffuse reflectance measurements as a function of the wavelength for sample II (no grooves).

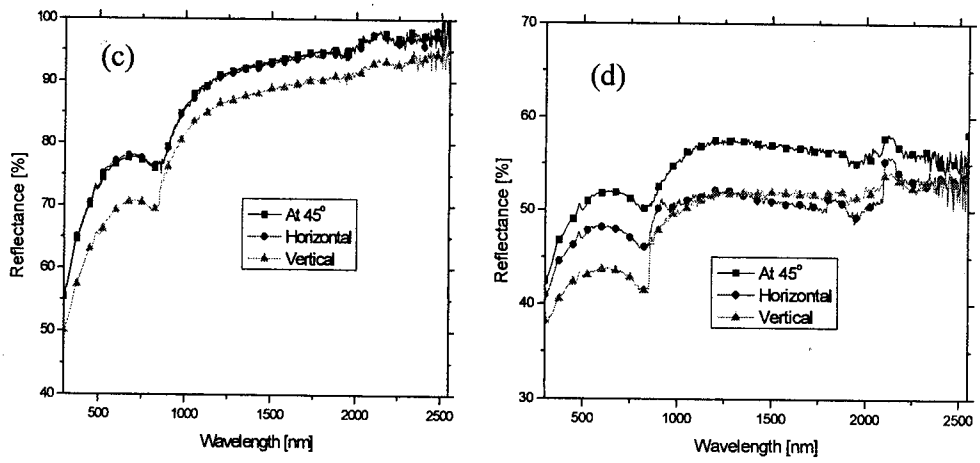

Fig. 7.5 : (c) Total reflectance, (d) diffuse reflectance curves for sample II.

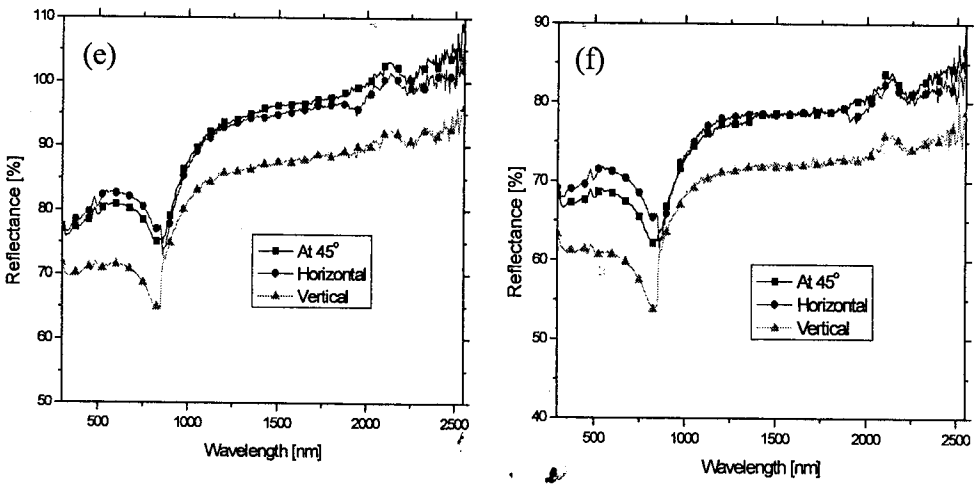

Fig. 7.5 : (e) Total reflectance, (f) diffuse reflectance curves for sample III.

The results for total and diffuse reflectance curves for sample III (large grooves) at different groove orientations are shown in figure 7.5(e) and (f) respectively.

7.4.2 Weighted Spectral Reflectance Results

Table 7.2 gives a quantitative summary of the total integrated reflectance *(TIR)* and the diffuse integrated reflectance *(DIR)* of the results in section 7.4.1 above as obtained from equation 6.2 of chapter 6.

Table 7.2: Comparison of the total integrated reflectance and diffuse integrated reflectance for different samples of aluminium.

Sample / Grooves orientation	Sample I (S1)	Sample II (S2)	Sample III (S3)
	Total Integrated Reflectance (TIR)		
At 45°	0.81	0.76	0.82
Horizontal	0.83	0.76	0.84
Vertical	0.77	0.76	0.75
	Diffuse Integrated Reflectance (DIR)		
At 45°	0.49	0.45	0.69
Horizontal	0.52	0.47	0.71
Vertical	0.49	0.45	0.63

It is clear from table 7.2 that sample II (S2) had no grooves because the same value of the total integrated reflectance *(TIR)* was obtained at all sample orientations. Furthermore, the rolling marks on samples I and III tend to enhance both total and diffuse reflectance. Furthermore, the larger the rolling marks the better the diffuse reflectance as seen from results of sample III. The general conclusion from table 7.2 is that the horizontal orientations of the rolling marks give larger scattering angle and hence, give a high probability of reaching the detector after a few reflections. The vertical orientations of the rolling marks give low scattering angle, and owing to the geometry of the sphere, some of the reflections leave the sphere through the reference port and the sample port, rendering a lower reflectance value. From symmetry considerations, the different orientations should yield the same reflectance value.

7.5 Effective Reflectance and Ray-Tracing Results

7.5.1 Solar Module Output from each Reflector Material

The dependence of open-circuit voltage and short-circuit current on the angle of incidence for each reflector material are shown in figure 7.6(a) and (b) respectively. The increase in the short-circuit current was a measure of the total irradiance on the cells. The anodized aluminium material gave high short-

circuit current because it was used as the base (part of the frame) reflector. The short-circuit current curves for Miro and aluminium foil had narrower angles

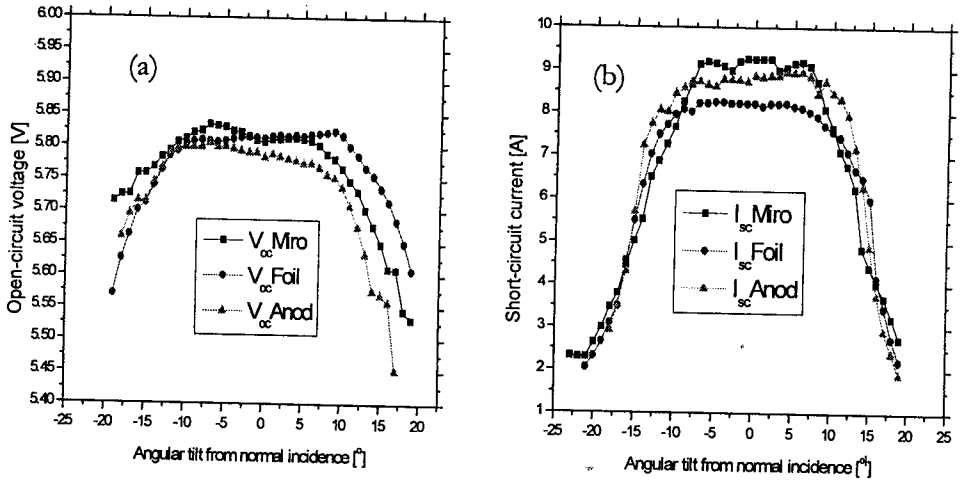

Fig. 7.6:(a) Dependence of open circuit voltage, (b) dependence of short circuit current on the angular tilt from normal incidence.

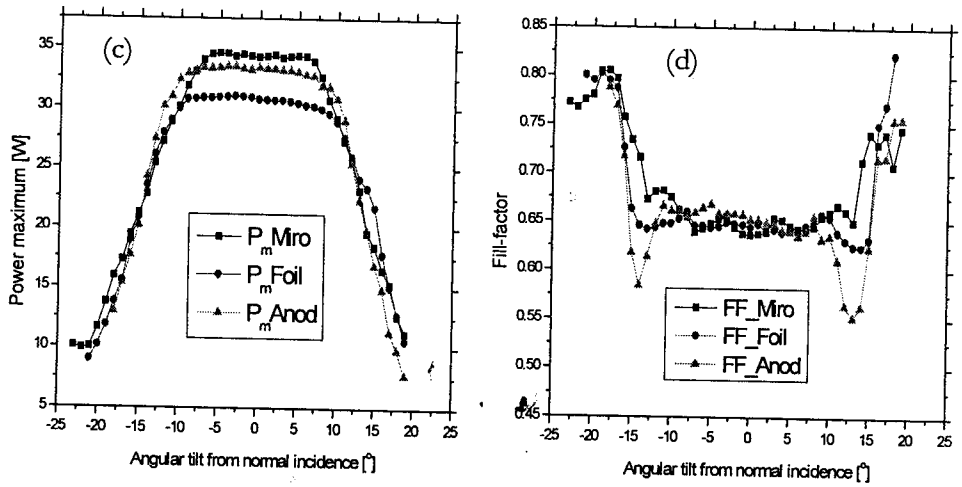

Fig. 7.6:(c) Dependence of maximum power, (d) dependence of fill factor on the angular tilt from normal incidence.

of acceptance because of the loose binding to the base reflector. The fall in short-circuit current at large angles of incidence were due to the reduction in solar radiation, optical imperfections and the presence of gaps between the module cells and the reflector. The dependence of maximum power and fill-factor for different reflectors as a function of angle of incidence are shown in figures 7.6(c) and 7.6(d) respectively. The fill factor for anodized aluminium reflector dropped drastically within 14 ± 2° because all the rays fell on the edge of the cells and hence increased the resistive losses. The fill factor values outside these angles of incidence (i.e $\geq 14^{o}$) increased due to decrease in the currents generated. However, there was general stability of the fill factor within ±10° of angular tilt for all the materials. At normal incidence (0°), the anodized reflector had higher fill factor followed by the aluminium foil reflector.

7.5.2 Effective Reflectance from Short-Circuit Current

The evaluation of the effective specular reflectance R_{eff} for each reflector material from short-circuit current measurements was performed from the proposed equation 7.1.

$$I_{sc}^{conc} = \left[1 + (C_g - 1)R_{eff}\right]\frac{I_b}{I_t} I_{sc}^{ref} + \left[\frac{1 + (C_g - 1)R_{eff}}{C_g}\right]\frac{I_d}{I_t} I_{sc}^{ref} \qquad 7.1$$

I_{sc}^{conc} is the measured short-circuit current under concentration, I_{sc}^{ref} is the reference short-circuit current measured when the module was placed on the entrance aperture of the CPC, I_b is the beam radiation, I_d is the diffuse radiation and I_t is the total radiation. The ratios of the beam radiation to the total $\left(\frac{I_b}{I_t}\right)$ and diffuse radiation to the total $\left(\frac{I_d}{I_t}\right)$ on a typical blue sky day were taken as 0.9 and 0.1 respectively[23]. The first term on the right gives the current contribution from beam radiation with losses and the second term gives the current contribution from diffuse radiation with losses. The measured values of the short-circuit current and the calculated values of the maximum power and fill factor are shown in table 7.3.

Table 7.3. Summary results for three reflector materials as measured within angular tilt of ±10°.

Material	I_{sc} *(A)*	I_{sc}/I_{sc}*(ref)*	P_m *(W)*	P_m/P_m*(ref)*	*FF*	R_{eff}
Miro	8.9	2.7	33.4	2.5	0.65	0.74
Foil	8.1	2.4	30.5	2.2	0.65	0.61
Anodized	8.7	2.6	32.9	2.4	0.65	0.69
Reference	3.3	1.0	13.6	1.0	0.72	

Although the fill factor of the three reflector materials was the same, their power increased by a factor of 2 as seen in table 7.3. However, rolled foil could have done better due to presence of rolling marks for even illumination.

7.5.3 Effective Reflectance from Flux Distribution Results

The simulated and the experimental flux distribution results for anodized aluminium reflector were in good agreement as shown in figure 7.7(a). The curve for the measured (Meas_Anod) shows a narrow width due to the non-ideal constructed CPC and losses due to truncation. The non-identical peaks

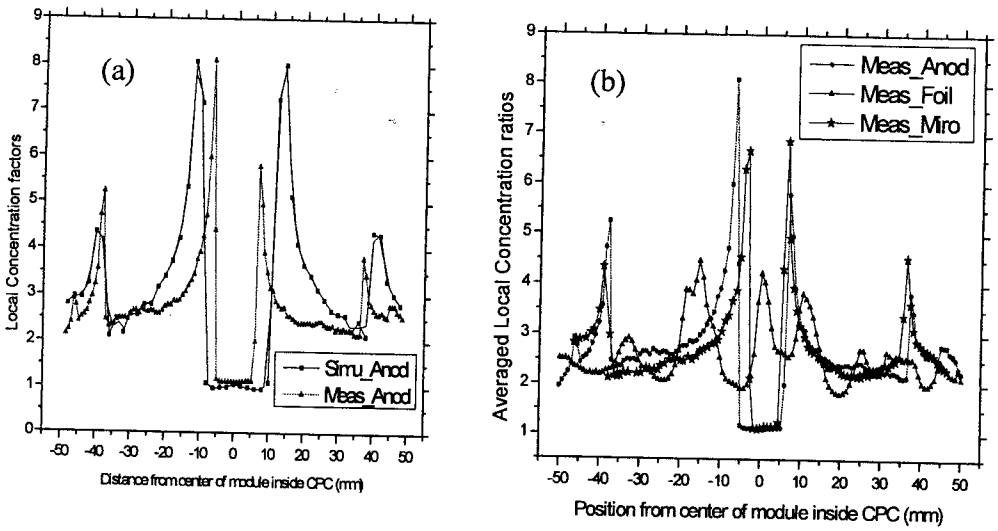

Fig.7.7:(a) Simulated concentration, (b) measured concentration from the center of the module.

also confirm the uneven geometry of the CPC. The local concentration factors as a function of position from the centre of the module for the three reflector materials is shown in figure 7.7(b). The concentration ratio curves for anodized and miro are identical because of being highly specular but the width for miro is smaller due to slight change in the shape of CPC when inserting the reflector. The corresponding curve for rolled foil was far from ideal because of loose fitting inside the CPC and as a result there were multiple reflections and interference within the CPC geometry. Table 7.4 compares the effective

Table 7.4 shows a summary of the local concentration ratios from flux measurements, the effective reflectance values from ray-tracing and the effective reflectance results from I-V measurements.

Reflector material	Loc. Conc. Ratio (Flux measurements)	Eff. Refl. (R_{eff}) (Flux and Ray-tracing)	Eff. Refl. (R_{eff}) (I-V plots)
Miro	2.72	0.73	0.74
Rolled Foil	2.59	0.68	0.61
Anodized Aluminium	2.70	0.72	0.69

specular reflectance as obtained from the flux distribution and current-voltage measurements. The effective reflectance values from I-V measurements are

low because they show the results of the worst cell in series. The effective reflectance from the flux distribution and ray-tracing and those from I-V measurements were in good agreement.

7.5.4 Qualitative Results from Ray-Tracing

Figure 7.8(a) and (c) show a simple grating with specific number of rays entering the CPC at normal incidence. Similarly, figure 7.8(b) and (d) show the same CPC results from ray-tracing as obtained from the Zemax software. We observe that at normal incidence (Fig. 7.8(a) and (b)), some rays reach the absorber directly and others hit the absorber after some reflection. In figures 7.8(c) and (d), the rays are incidence at the acceptance half angle of 15° and reach the focal point only after a single reflection as expected. The rays that reach the absorber directly are due to truncation of the CPC.

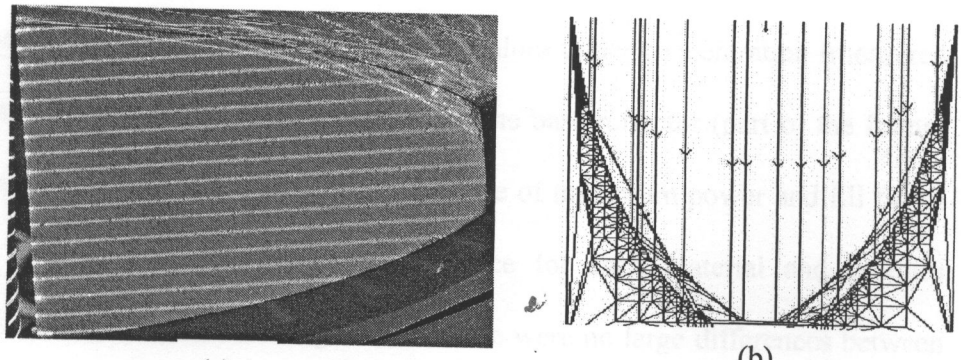

(a) (b)

Figure 7.8: (a) ray-tracing from a simple grating, and (b) ray-tracing from Zemax software at normal incidence.

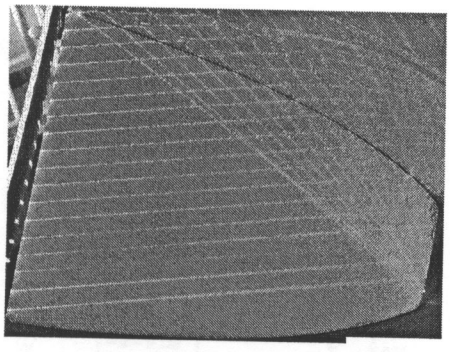

(c)

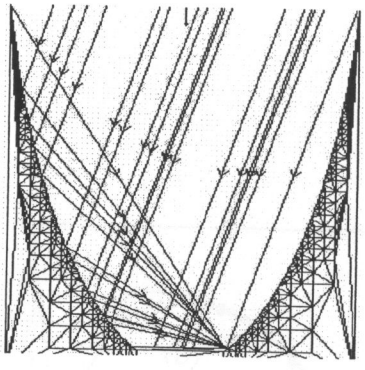

(d)

Figure 7.8: (c) ray-tracing from a simple grating, and (d) ray-tracing from Zemax software at 15° angle of incidence.

7.6 Performance of CIS Modules under Low Concentration

7.6.1: I-V Characteristics of CIS Modules

At normal incidence, the reference short-circuit current *Isc(ref)* and the reference open-circuit voltage *Voc(ref)* (measured outside CPC) were 0.187A and 25.77V respectively. However, the values under concentration (measured inside CPC) were 0.555A and 26.93V. The base reflector (part of the frame) was the specular material. The dependence of maximum power and fill factor as a function of the angle of incidence for each material and grooves orientations are shown in figure 7.9. There were no large differences between the maximum power measured at normal incidence as well as between ± 5°

from normal incidence since the illumination was almost constant in these angular intervals.

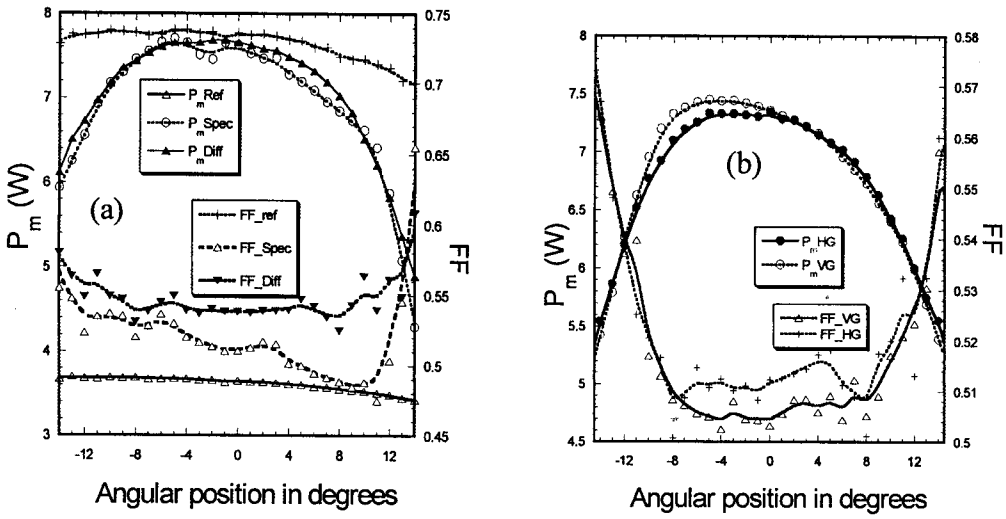

Figure 7.9 :(a) Maximum power and fill-factor for specular and diffuse materials, (b) Maximum power and fill-factor for the diffuse material with rolling marks.

However, the diffuse material gave a better fill-factor than specular material. The diffuse material with rolling grooves aligned parallel to the plane of the module also gave better fill factor as compared to the rolling grooves aligned perpendicular (vertical) to the plane of the module as seen in figure 7.9(b).

7.6.2 Optical Behaviour of Grooved Reflectors

Figure 7.10 shows the comparison of the optical measurement curves between specular and diffuse reflectors (a) and between diffuse reflector (b) with rolling marks horizontal *(HG)* and vertical *(VG)* as a function of wavelength in nm. We also show in table 7.5 the total integrated reflectance *(TIR)*, the diffuse integrated reflectance *(DIR)* and the specular integrated reflectance *(SIR)* for the specular *(Spec)*, the diffuse material with horizontal grooves *(Diff-HG)* and with vertical grooves *(Diff-VG)* as obtained from equation 6.3.

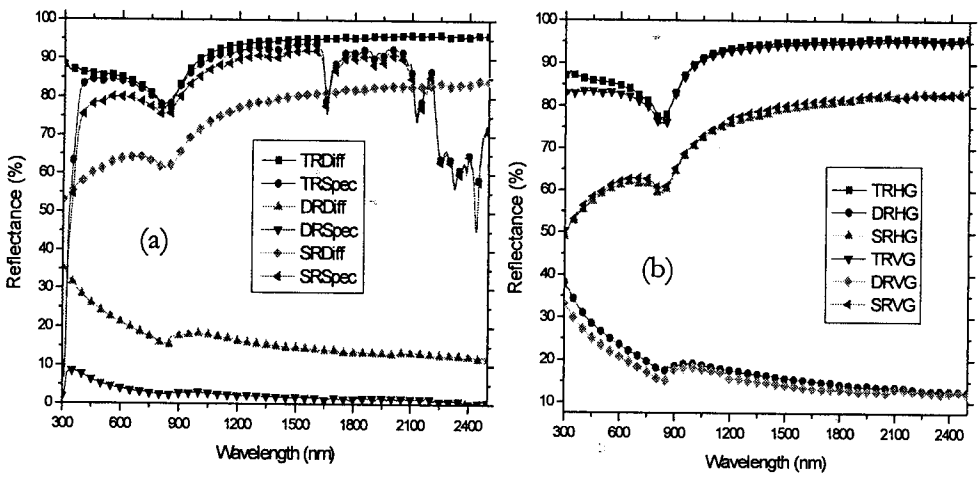

Figure 7.10: (a)Optical behaviour of diffuse and specular reflectors and (b) the optical behaviour of groove orientation of diffuse reflector.

Table 7.5: *Quantitative optical behaviour of reflectors materials in terms of their weighted integrated reflectance values.*

Material	TIR	DIR	SIR
Diff-VG	0.85	0.19	0.66
Diff-HG	0.86	0.22	0.64
Spec	0.84	0.04	0.80

7.7 Performance of the Large Parabolic Reflector

7.7.1 Effective Reflectance of the Reflector Material

The instantaneous short-circuit current outside and under concentration were plotted as shown in figure 7.11 and tabulated in table 7.6. The temperature

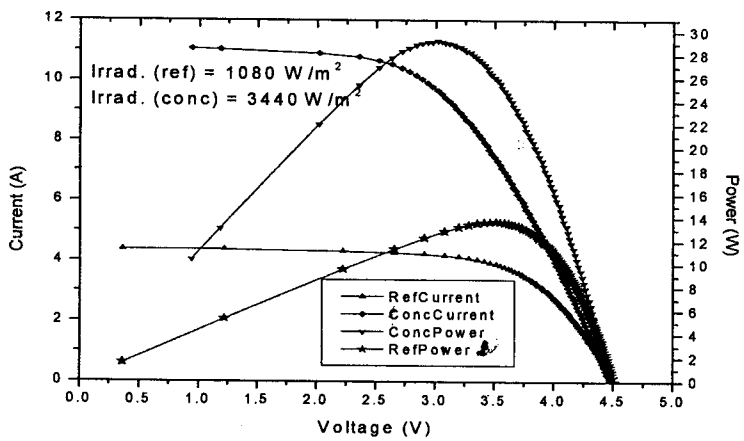

Figure 7.11: I-V and the power curves for reference (outside concentration) and under concentration for the 8-string cell module.

Table 7.6: Comparison of solar cell module parameters under concentration and outside concentration (C_g = 7.8 for the large reflector).

Parameters	Reference	Conc.	Opt. Conc. Ratio ($C_{Opt.}$)
V_{oc} (V)	4.51	4.47	
I_{sc} (A)	4.36	11.06	2.54 (with losses)
P_m (W)	13.71	29.22	2.13
Fill-Factor	0.69	0.59	
Irrad. (W/m^2)	1080	3440	γ_i = 3.18

effect was neglected since the I-V tracker instrument made a complete I-V curve within three seconds consisting of one hundred data points. Furthermore, the module was covered at all times unless during a measurement. However, even under such circumstances, the fill-factor dropped by about 14.5% and the overall increase in short-circuit current was by a factor of 2.53. The solar radiation measurements on the module surface inside the parabolic reflector and on the entrance aperture of the parabolic reflector increased by a factor of 3.18. Hence, the amount of radiation was proportional to the short-circuit current. The optical efficiency of the system was calculated from equation 6.16 as 0.32.

The short-circuit current and the fill-factor profiles as functions of the position of line focus across the solar cell module are shown in figure 7.12. We observe that the highest short-circuit current and maximum power were attained when 80% (10/12.5) of the total module area was under illumination. It is therefore advisable to operate the module string with most of its area illuminated.

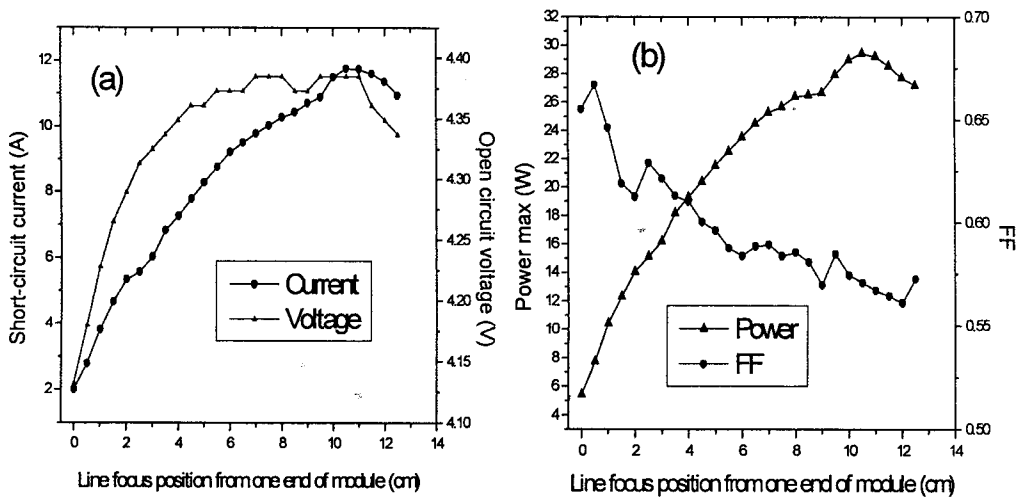

Figure 7.12: (a) Current and voltage as a function of the position of the line focus and (b) power and fill-factor as a function of the position of the line focus on the module.

The average effective specular reflectance R_{eff} for the reflector material was calculated from equation 5.8.6 as 0.80, consistent with the spectrophotometer measured value of 0.87[23]. The percentage error of about 8% was mainly due to

the imperfections in the large parabolic concentrator geometry and that the diffuse radiation in equation 7.16 was neglected.

7.8 Long-Term Degradation of Commercial Reflectors

7.8.1 The Reflectance Degradation Curves

In figure 7.13 we show the results of reflectance curves after one year's exposure. The term *TRRef* stands for total reflectance for the reference samples, *TRBx* stands for total reflectance for box samples and *TREx* stands for total reflectance for exposed samples. We also show the diffuse reflectance for the reference samples (*DRRef),* for the box samples (*DRBx)* and for the exposed samples (*DREx).* Furthermore, we show the specular reflectance for the reference samples (*SRRef),* for the boxed samples (*SRBx)* and for the exposed samples (*SREx).* The quantitative differences in terms of their weighted integrated reflectance after one year's exposure are shown in table 7.7.

In figure 7.14 we show summary results of reflectance curves after twenty two (22) months of sample exposure. The quantitative differences in terms of their weighted integrated reflectance after one year and ten months of exposure are shown in table 7.8. The relative cost of the commercial reflector materials are also given in table 7.9.

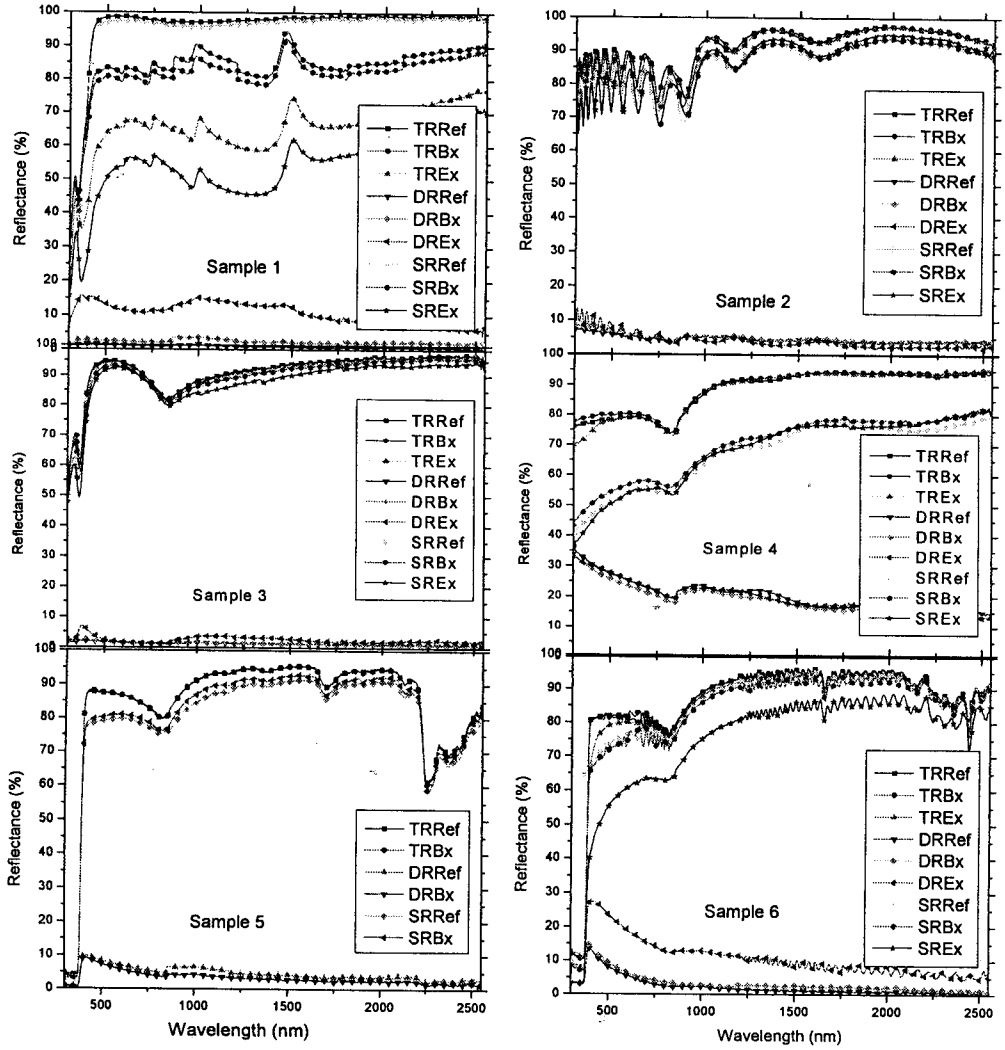

Figure 7.13: The reflectance curves as a function of wavelength for six samples after one year's exposure (Reference, Box and Exposed).

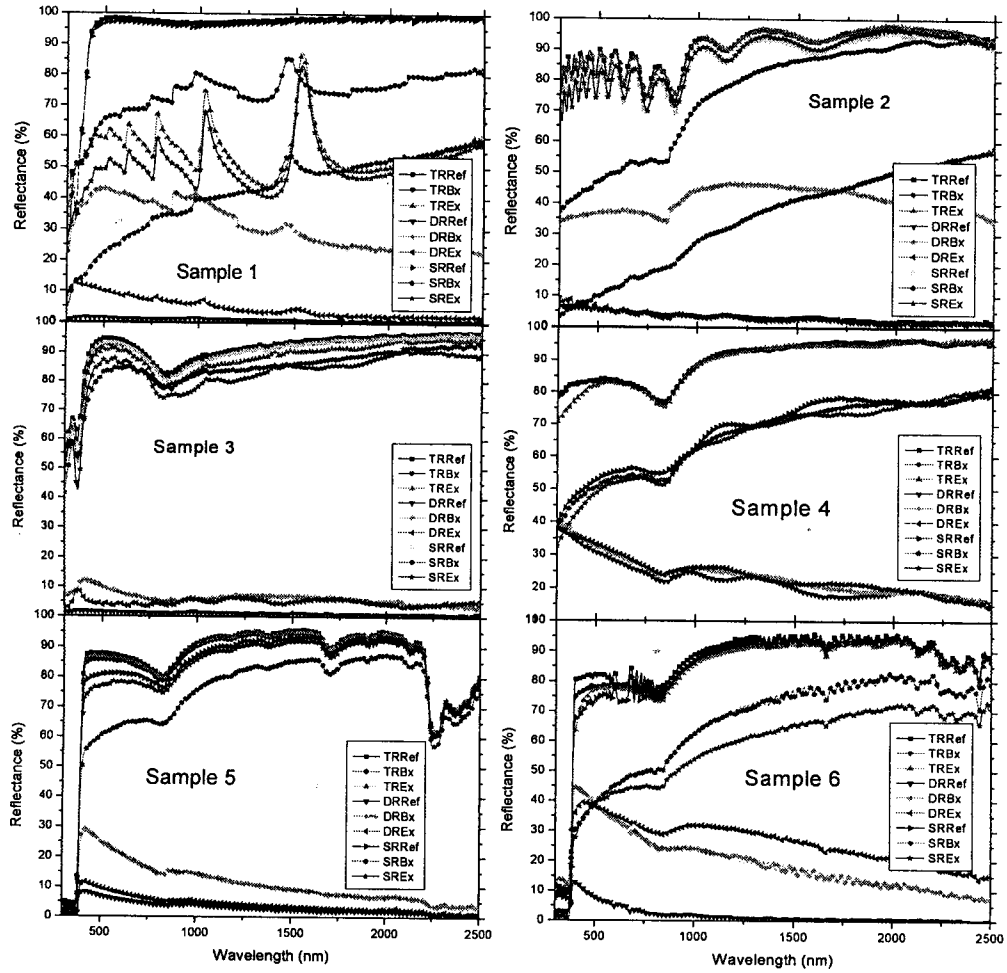

Figure 7.14: The reflectance curves as a function of wavelength for six samples after 22 months of exposure (Reference, Box and Exposed)

The total reflectance value for silver on aluminium sample was less after washing than before washing. The reason being that some of the silver deposed on aluminium were removed during cleaning. The other samples had the usual higher reflectance after cleaning than before cleaning. However, all

the results analyzed and reported were those for cleaned samples. In particular, 15% degradation was observed in total reflectance for samples kept in the box and about 34% degradation for samples exposed to natural environment after one year's exposure. However, 27% degradation was observed for samples in the box and about 40% degradation for exposed samples after twenty two months of sample exposure. The overall conclusion was that samples exposed to natural environment had more degradation effects than those kept in the box.

Table 7.7: Summary results for boxed and exposed samples as compared to the reference samples after one year's exposure.

	Total Reflectance			Diffuse Reflectance			Specular Reflectance		
Sample	Ref	Box	Exp	Ref	Box	Exp	Ref	Box	Exp
1	0.96	0.82	0.63	0.01	0.03	0.12	0.95	0.79	0.51
2	0.86	0.86	0.86	0.05	0.06	0.05	0.81	0.80	0.81
3	0.90	0.90	0.89	0.01	0.01	0.03	0.89	0.89	0.86
4	0.82	0.83	0.81	0.24	0.22	0.24	0.58	0.61	0.57
5	0.84	0.84	-	0.06	0.05	-	0.78	0.79	-
6	0.82	0.81	0.80	0.05	0.06	0.16	0.77	0.75	0.64

- Exposed sample 5 was blown off by wind twice but was replaced 23/04/06.

The anodized aluminium samples did not show much degradation effects either in the box or when exposed to natural environment. The 31% degradation for the box sample was due to soiling as it drastically changed its colour and was observed in the last ten months of exposure. The general observation was that anodized aluminium was a very stable sample for the period under review.

Table 7.8: Summary results for box and exposed samples as compared to the reference samples after 22 months exposure.

	Total Reflectance			Diffuse Reflectance			Specular Reflectance		
Sample	Ref	Box	Exp	Ref	Box	Exp	Ref	Box	Exp
1	0.96	0.70	0.58	0.01	0.38	0.07	0.95	0.32	0.51
2	0.86	0.59	0.86	0.04	0.39	0.04	0.82	0.20	0.82
3	0.90	0.89	0.85	0.01	0.07	0.04	0.89	0.82	0.81
4	0.85	0.85	0.84	0.26	0.28	0.28	0.59	0.57	0.56
5	0.84	0.83	0.84	0.05	0.17	0.06	0.79	0.66	0.78
6	0.81	0.79	0.78	0.04	0.28	0.32	0.77	0.51	0.46

Ref - Reference, *Box* - Box stored and *Exp* - Exposed to natural environment

The total reflectance for miro sample remained fairly the same for box samples but degraded by about 1% for those exposed to natural environment after one year's exposure and a further degradation of about 5% after twenty two months of exposure to the natural environment. The general observation was that miro samples were stable in the box but rather weak when exposed to the natural environment.

Table 7.9: The relative cost per square meter of the commercial reflectors (courtesy of Bjorn Karlsson, 2007).

Sample	Type of reflector	Cost per sq. meter (US$)
1	Silver on aluminium	30 - 40
2	Anodized aluminium	10 -20
3	Miro	30
4	Rolled aluminium foil, laminated on plastic	3 - 5
5	Evaporated aluminium on plastic, laminated on plastic	10
6	Evaporated aluminium on plastic, laminated on steel	40

The total reflectance for rolled aluminium samples remained fairly unchanged. The degradation of 1% was observed for exposed samples after twenty two months' sample exposure. However, the rolled aluminium sample results must be consistent with the same orientation of the grooves since horizontal orientation improves the reflectance. The general conclusion from this sample was that it was durable and relatively better diffuse. Although it was still specular, it could be preferred to be used in low concentration because of its relatively low-cost.

The total reflectance of the evaporated aluminium on plastic, laminated on plastic remained fairly constant for the period under review. The only problem was that it was about 25% more specular than sample number 4 (rolled aluminium). The general observations were that evaporated aluminum on plastic and laminated on plastic could be used as a reflector material but rather expensive.

The total reflectance of evaporated aluminium on steel also remained fairly constant especially for the samples in the box. There was an average degradation of about 4% for samples exposed to natural environment. The general observations were that evaporated aluminium on steel samples had high diffuse reflectance and low specular reflectance. This condition was ideal

for solar reflector materials. The biggest drawback is that it could only be used as a planar reflector because it is not easy to bend steel. Furthermore, the cost of steel per square meter is eight times more than the cost of rolled aluminium.

Chapter 8

CONCLUSIONS AND RECOMMENDATIONS FOR FUTURE WORK

8.1 CONCLUSIONS

The reflectance measurements in the integrating sphere for grooved aluminium samples show marked differences because of the preferential reflections from the grooves based on the sample orientations. The horizontal direction of the rolling marks to the plane of the exit port of the integrating sphere tend to give higher diffuse and total reflectance than vertical or oblique orientations of the rolling grooves due to large angle scattering of light within the integrating sphere and hence increase the probability of light reaching the detector after less number of reflections. The vertical grooves on the other hand tend to underestimate the performance of the integrating sphere and the sample beam reaches the detector after a large number of reflections. Furthermore, the detector (PbS_2) in the integrating sphere has a wider field of view (view angle) when flux scattering is from horizontal rolling marks as compared to a narrower field of view for vertical orientations of the rolling grooves.

Measurements of the fill-factor *(FF)* from the compound parabolic concentrator using diffuse and specular materials show that diffuse materials give higher fill-factor than specular materials. Furthermore, diffuse materials with rolling grooves aligned parallel to the plane of the module give higher fill-factor than rolling marks oriented perpendicular to the plane of the module. In particular, the overall percentage decrease in the fill-factor was about 28% for the parallel grooves and about 30% for the perpendicular grooves at normal incidence. However, the power output from the module increased by a factor of 2 both types of orientations. The smaller decrease in the fill-factor (larger fill-factor) for the parallel grooves was due to the fact that the solar flux was scattered at larger angles over the module surface and hence distributing the currents uniformly within the module. The spread in the solar flux over the module further reduced the resistive losses and therefore addressing the problem of hot-spot formation.

A compound parabolic concentrator system with a geometrical concentration ratio of 3.58, truncated 44% of its original height and half acceptance angle of 15° showed a short-circuit current increase of about 2.5 at normal incidence when anodized aluminium, miro and rolled aluminium foil were used as reflectors. This increase in short circuit current also increased the resistive losses in the module cells and hence decreased the fill factor by about 10% for

anodized aluminium, miro and rolled aluminium reflectors contrary to our expectations. The rolled aluminium reflector could have performed better due to the presence of the rolling marks which could have scattered the solar flux. The proper alignment of the grooves and the size of the rolling marks could have suppressed the performance of the rolled aluminium.

The percentage difference between the effective specular reflectance (R_{eff}) for miro, rolled aluminium and anodized aluminium reflectors as obtained from short-circuit current measurements and from ray-tracing analysis were 1%, 10% and 4% respectively. It could therefore be concluded that the experimental measurements were in good agreement with theory to within 10%.

The experimental results for the large parabolic concentrator showed that the effective specular reflectance (R_{eff}) for anodized aluminium was 0.80 as compared to the standard value of 0.87. The 8% difference was due to the poor geometry of the parabolic reflector and the optical (reflection) losses. However, the output power increased by 74% while the fill factor dropped only by about 4.2%. The optical efficiency of the system was about 32% and this value could have been improved if active or passive cooling mechanisms were employed on the string module.

The silver on aluminium sample showed the worst degradation effect to environmental factors as the coated silver peeled off with time. The evaporated aluminium on plastic and laminated on steel sample showed an increase in diffuse reflectance because of the ultraviolet radiation which reacted with the plastic layer. Anodized aluminium and miro reflector samples proved to be robust in that very little change in their reflectance was observed. The evaporated aluminium on plastic and laminated on plastic had performed better but remained relatively specular. However, rolled aluminium foil laminated on plastic could be the best candidate in low concentrating systems because of its long life and relatively low-cost material. Compared to rolled aluminium foil, miro is 10 times more expensive, anodized is 5 times more expensive, silver is 12 times more expensive, evaporated aluminium on steel is 13 times more expensive and evaporated aluminium on plastice is 3 times more expensive. Thus, the three best reflector materials ranked according to their resistance to environmental conditions are anodized aluminium, miro and rolled aluminium foil.

8.2 Recommendations for Future Work

- Although it was verified that the horizontal grooves could solve the problem of uneven illumination, there is need to optimize the groove sizes for optimal performance. The scattering of the solar flux as a function of groove height and groove separation ought to be analyzed further for optimal performance.

- Although polarized light tend to improve total reflectance of structured samples in the integrating sphere, both the polarizer and the analyzer need to be used in the study of total and diffuse reflectance from the orientations of the rolling marks. Interpretation of reflectance results needs to be understood.

- An automated performance of the large parabolic concentrator need to be carried out. Passive cooling mechanisms need to be incorporated such as aluminium cooling fins to decrease temperature gradients. Alternatively, re-design the parabolic concentrator for static conditions to reduce cost on tracking.

- Since the life of a solar concentrator system is about 20 to 25 years, the degradation effects of the reflector materials need to be tested for longer periods as compared to only twenty two months of study.

REFERENCES

1. Duffie J. A, and W. A. Beckman, 1991. *Solar Engineering of Thermal Processes,* 2nd edn. New York: Wiley-Inter-science.

2. Goma S., K. Yoshioka and T. Saitoh, 1997. *Effect of Concentration Distribution on Cell Performance for Low-Concentrators with a 3-D Lens.* Solar Energy Materials and Solar Cells, **47**, 339-344.

3. Goldemberg J. (ed.), 2000. *World Energy Assessment: Energy and the Challenge of Sustainability.* United Nations Development Programme (UNDP).

4. Wennerberg Johan, 2002. *Design and Stability of Cu(In,Ga)Se_2 – Based Solar Cell Modules*. Ph.D. Thesis, Uppsala University.

5. Bhattacharya Tapan, 1998. *Terrestrial Solar Photovoltaics.* New Delhi: Narosa Publishing House.

6. Muhammad Iqbal, 1983. *An Introduction to Solar Radiation*. Vancouver, Canada: Academic Press.

7. Tiwari G. N., 2002. *Solar Energy, Fundamentals, Design, Modeling and Applications*. New Delhi: Narosa Publishing House.

8. *http://en.wikipedia.org/wiki/Horizontal_coordinate_system* "Horizontal Coordinate System - Wikipedia, the free encyclopedia".

9. *http://www.keck.hawaii.edu/inst/KSDs/40/html/ksd40-55.4.html.*

10. *http://www.usc.edu/dept/architecture/mbs/tools/vrsolar/help/solar_concepts.html.*

11. Kininger Frank, 2003. *Photovoltaic Systems Technology SS2003.* University Kassel, Germany.

12. Twidell J. W. and A. D. Weir, 1986. *Renewable Energy Resources* (E & F. N. Spon, London).

13. Bube H. R. and Alan L. Fahrenbruch, 1983. *Fundamentals of Solar Cells, Photovoltaic Solar Energy Conversion.* Stanford University, California: Academic Press Inc.

14. Liu B. Y. H. and R. C. Jordan, 1961. *Daily Insolation on Surfaces Tilted toward the Equator.* ASHRAE Journal, **3**(18), 53-59.

15. Garg H.P. and J. Prakash, 2000. *Solar Energy, Fundamentals and Applications.* Revised Edition, New Delhi: Tata McGraw-Hill.

16. Mathur S. S. and T. C. Kandpal, 1984. *Solar Concentrators. Reviews of Renewable Energy Sources.* Vol. 2, Chapter 5, New Delhi: Wiley Eastern Ltd.

17. Swanson M. R., 2000. *The Promise of Concentrators, Progress in Photovoltaics: Research and Applications*, **8**, 93-111.

18. Donovan R. L., and R. Hunter, 1978. *Proceedings of the 13th Photovoltaic Specialists Conference.* New York. IEEE, pp. 1125.

19. Kreith F. and J. F. Kreider, 1980. *Principles of Solar Engineering.* New York, McGraw-Hill Book Co.

20. Welford W. T and R. Winston, 1989. *High Collection Non-imaging Optics.* Academic Press.

21. Rabl A., 1976a. *Comparison of Solar Concentrators.* Solar Energy, **18**, 93.

22. Mwamburi M., E. Wackelgard and A. Roos, 2000. *Preparation of Solar Selective SnOx:F Coated Aluminium Surfaces.* Thin Solid Films **374**, 1-9.

23. Brogren *et al.*, 2004. *Optical Properties, Durability, and System aspects of a New Aluminium Polymer Laminated Steel Reflector for Solar Concentrators.* Solar Energy Materials and Solar Cells, **82**, 387-412.

24. Garg H. P., 1982. *Treatise on Solar Energy.* John Wiley and Sons.

25. Perers B. and B. Karlsson, 1993. *External Reflectors for Large Collector Arrays, Simulation Model and Experimental Results.* Solar Energy **51**, (5), 327-337.

26. Nostell P., 2000. *Preparation and Optical Characterization of Antireflection Coatings and Reflector Materials for Solar Energy Systems.* PhD Thesis, Faculty of Science and Technology, Uppsala University.

27. Ronnelid M., B. Perers and B. Karlsson, 1996. *Construction and Testing of a Large Area CPC Collector and Comparison with a Flat-Plate Collector.* Solar Energy **57**, 177-184.

28. Saitoh T. and K. Yoshioka, 1998. *Preparation and Properties of Photovoltaic Static Concentrators.* Renewable Energy **15**, 566-571.

29. Luque A., G. Sala and J. C. Arboiro, 1998. *Electric and Thermal Model for Non-Uniformly Illuminated Concentration Cells.* Solar Energy Materials and Solar Cells, **51**, 269-290.

30. Mwamburi M., B. Karlsson, and R. T. Kivaisi, 1997. *Transparent Conductor Coated Aluminium reflectors for PV Applications, in North Sun* 97, Helsingfors, Finland.

31. Wedepohl K. H., 1995. *The Composition of the Continental Crust. Geochemica and Cosmochimica*; pp: 1217 - 1232

32. Nostell P., A. Roos and B. Karlsson, 1998. *Ageing of Silver Booster Reflector Materials.* Solar Energy Materials and Solar Cells, **54**, 235 – 246.

33. Chibuye B. Teddy, 2004. *A Comparative Study of Copper and Nickel – Pigmented Anodized Aluminium Coatings for Solar Energy Absorption.* Ph.D. Thesis, University of Zambia.

34. Roos A., 1993. *Use of an Integrating Sphere in Solar Energy Research.* Solar Energy Materials and Solar Cells, **30**, 77-94.

35. Roos A., 1994. *Measurement of Optical Reflectance and Transmittance.* Department of Technology, Uppsala University, Box 534, S-751 21 Uppsala, Sweden.

46. Grandin K. and A. Roos, 1994. *Evaluation of Correction Factors for Transmittance Measurements in Single Beam Integrating Spheres.* Applied Optics, **33**, 6098-6104.

37. Neville R. C., 1995. *Solar Energy Conversion: The Solar Cell.* 2nd Elsevier Science, Amsterdam, Netherlands.

38. Boyle G. (ed.), 1996. Renewable Energy: *Power for Sustainable Future.* Oxford University Press in association with Open-University, New York.

39. Green A. M., 1992. *Solar Cells – Operating Principles, Technology and System Applications.* University of New South Wales, Australia.

40. Möller J. Hans, 1993. *Semiconductors for Solar Cells.* Artech House, INC, Boston, London.

41. Sze S. M., 1985. *Semiconductor Devices, Physics and Technology.* AT&T Bell Laboratories, Murray Hill, New Jersey.

42. Luque Antonio, 1989. *Solar Cells and Optics for Photovoltaic Concentration.* Adam Hilger, pp. 318.

43. Stapleton Geoff, Lalith Gunaratne, and Peter J.M. Konings, 2002. *The Solar Entrepreneur's Handbook, Global Sustainable Energy Solutions Pty.* New South Wales, Australia.

44. Wenham S. R., M. A. Green and M. E. Watt, 1994. *Applied Photovoltaics. Centre for Photovoltaic Devices and Systems.* University of New South Wales.

45. Markvart T. (ed.), 2000. *Solar Electricity.* John Wiley & Sons, New York.

46. Stone L. Jack, 1993. *Photovoltaics - Unlimited Electrical Energy from the Sun.* Physics Today, September, 1993.

47. Sayigh A. A. M., 1991. *Photovoltaic and Solar Radiation, in Generating Electricity from the Sun.* F. C. Treble (ed.), BPCC Wheaton Ltd: Exeter.

48. Rever B., 2001. *Grid-tied Market for Photovoltaics. A New Source Emerges.* Renewable Energy World, **4**(4), 176 – 189.

49. DeMeo E.A and J.F Galdo, 1997. *Renewable Energy Technology Characterizations*. Topical Report, TR-109496, U.S. Department of Energy and EPRI.

50. *http://eosweb.larc.nasa.gov/sse September 1, 2003*. The NASA Langley Research Atmospheric Sciences Data Center.

51. *http://sel.me.wisc.edu/trnsys*

52. Perers B. and B. Karlsson, 2007. *Energy and Building Design*. Lund University, Faculty of Engineering (LTH), WINSUN Based on TRNSYS/TRNSED/PRESIM 14.2

53. Rönnelid M. and B. Karlsson, 1997. *Irradiation Distribution Diagram and their use for Estimating Collectable Energy*. Solar Energy, **61** (3), 191-201

54. ISO 9845-1, 1992. Solar Energy – *Reference Solar Spectral Irradiance at the Ground at Different Receiving Conditions*. Part 1: Direct normal and hemispherical solar irradiance for air mass 1.5, (E).

55. Nilsson Johan, 2005. *Optical Design and Characterization of Solar Concentrators for Photovoltaics*. Licentiate Thesis, Lund University.

56. ZEMAX version 3, 2005. *ZEMAX Development Corporation*. San Diego, California, USA.

57. Thomas B. G. and R. L. Finney, 1997. *Calculus and Analytical Geometry*. Narosa Publishing House, New Delhi.

58. Hatwaambo *et al.*, 2008. *Angular Characterization of Low Concentrating CPCs Using Structured Reflectors*. Solar Energy Materials and Solar Cells, **92**, 1347-1351.

59. Brogren M., P. Nostell and B. Karlsson, 2000. *Optical Efficiency of a PV-Thermal Hybrid CPC Module for High Latitudes*. Solar Energy, **69** (1-6), 173-185.

60. Wennerberg J., J. Kessler, J. Hedström, L. Stolt, B. Karlsson and M. Rönnelid, 2000. *Thin film PV modules for low concentrating systems*.

Solar Energy, **69** (Suppl.), 243-255.

61. Ronnelid Mats, 1998. *Optical Design of Stationary Solar Concentrators for High Latitudes*, Ph.D. Thesis, Uppsala University, pp. 13.

62. Bione J., O. C. Vilela and N. Fraidenraich, 2004. *Comparison of the Performance of PV Water Pumping Systems Driven by Fixed, Tracking and V-Trough Generators.* Solar Energy, **76**, 703-711

63. Meteorological Department, Ministry of Communications and Transport, Lusaka. (Private communication).

64. Hatwaambo *et al.*, 2009. *Projected Beam Irradiation at Low Latitudes Using Meteonorm Database*. Renewable Energy, **34**, 1394-1398.

Solar Energy Materials & Solar Cells 92 (2008) 1347–1351

Contents lists available at ScienceDirect

Solar Energy Materials & Solar Cells

journal homepage: www.elsevier.com/locate/solmat

Angular characterization of low concentrating PV–CPC using low-cost reflectors

Sylvester Hatwaambo [a,*], Hakan Hakansson [b], Johan Nilsson [b], Bjorn Karlsson [b]

[a] Department of Physics, University of Zambia, Box 32379, Lusaka 10101, Zambia
[b] Division of Energy and Building Design; Department of Architecture and Built Environment, Lund University, Box 118, SE-221 00 Lund, Sweden

ARTICLE INFO

Article history:
Received 14 June 2007
Accepted 19 May 2008
Available online 27 June 2008

Keywords:
Angular-tilt
Acceptance half angle
Low concentration
Energy flux

ABSTRACT

The most expensive component in a conventional solar photovoltaic (PV) system is the solar module cell. The module cost could be reduced if low-cost reflector materials are used to concentrate solar energy flux across a small module area. Three reflector materials were studied for fill-factor improvements in low concentrating system. These were anodized aluminium, rolled aluminium foil and miro reflectors. From the short-circuit current measurements within $\pm 10°$ from normal incidence, the effective specular reflectance was predicted for each reflector material. The effective specular reflectance was predicted from the flux distribution profile measurements and the ray-tracing results at normal incidence. The ray-tracing and the short-circuit current results were in good agreement within 10% but rather different from spectrophotometer measured results.

1. Introduction

Imaging and non-imaging concentrators are used to raise the amount of incident solar radiation over a relatively small area of the absorber. Increasing the concentration ratio also means increasing the temperature at which energy is delivered to the absorber. This is undesirable in low concentrating photovoltaic (PV) systems with conventional solar cells as the increase in temperature decreases the efficiency of the system. Low concentrating systems with low concentration ratios have received great attention since the birth of non-imaging optics in the late 1970s [1]. Non-imaging static concentrators have been fabricated and tested using converging (Fresnel) lenses as refractive elements [2–4].

Optical concentration ratios of 1.75 with acceptance angles of 30° have been reported for two-dimensional (2D) concentrators [2]. The problem of non-uniform illumination and the dependence of fill-factor on the series resistance of the solar cell have been highlighted in both 2-D and 3-D lenses [3].

On the other hand, non-imaging static concentrators with reflective elements for low concentration have been fabricated and tested for high latitudes [5–7]. Specular reflectors have shown to have a long life time but the problem of non-uniformity of illumination has been prominent [6]. Low cost partly diffuse reflectors have a great potential for overall cost reduction in PV-thermal hybrids provided the problem of non-uniform irradiance could be solved or greatly minimized [8,9].

1.1. Specific objectives

In this paper, we investigate the performance of a low-concentrator PV system with two highly specular materials (miro and anodized aluminium) and a diffuse material with rolling marks (rolled aluminium foil) used as reflective elements. The overall objective was to investigate how a reflector with low-angle anisotropic scattering in one direction and specular in the other can be characterized for use in low concentrators.

2. Method

2.1. The compound parabolic concentrator (CPC) geometry

A standard symmetrical CPC was constructed and truncated as shown in Fig. 1. The acceptance half angle, θ_c, and the geometrical concentration ratio, C_g, were 15° and 3.6°, respectively. The optical properties of the reflector materials in terms of their integrated specular reflectance were analyzed [10] from the Lambda 900 spectrophotometer at Uppsala University.

2.2. Current–Voltage curve measurements

The characteristic current–voltage (I–V) curves were measured using an electronic load instrument [11]. The voltage could be measured through a logging system of potentiometers, operational amplifiers and power transistors. Current up to 14 A could be measured through a four-terminal shunt resistance with low internal resistance (0.01 Ω).

* Corresponding author. Tel.: +260 211 293343; fax: +260 211 253952.
E-mail addresses: shatwamb@gmail.com, shatwaam@unza.zm (S. Hatwaambo).

0927-0248/$ - see front matter © 2008 Elsevier B.V. All rights reserved.
doi:10.1016/j.solmat.2008.05.008

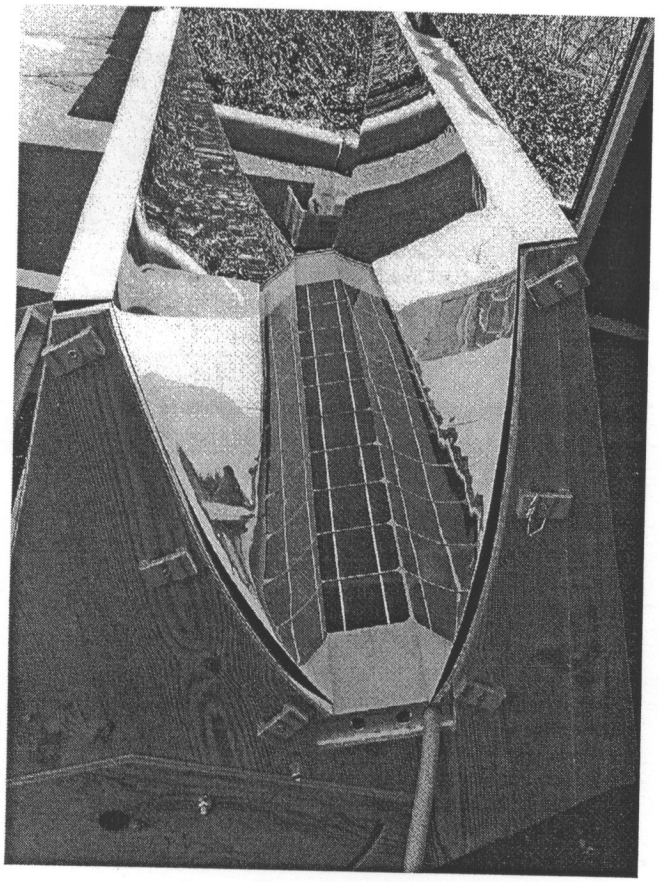

Fig. 1. The truncated compound parabolic concentrator showing removable reflectors and a 10-cell module string.

The CPC was manually tilted below and above normal incidence (0°) in 1° interval to ±20°. Angular tilts below normal incidence were taken as negative and those above normal incidence were taken as positive. At every angle of incidence, an *I–V* curve was plotted for each reflector material. The current values were compensated for irradiance at 950 W/m^2 and the voltage values were compensated for temperature increase on the module at 25 °C. From each plotted *I–V* curve, the short-circuit current I_{sc}, the open circuit voltage V_{oc}, the maximum current I_{max} and the maximum voltage V_{max} were extracted. Subsequently, the maximum power P_{max} and the fill-factor, FF, were calculated at each angle of incidence.

The effective specular reflectances (R_{eff}) for each material was estimated from the short-circuit current Eq. (1) at normal incidence.

$$I_{sc}^{conc} = [1 + (C_g - 1)R_{eff}]\frac{I_b}{I_t}I_{sc}^{ref} + \left[\frac{1 + (C_g - 1)R^{eff}}{C_g}\right]\frac{I_d}{I_t}I_{sc}^{ref} \quad (1)$$

The first expression on the right gives the current contribution from beam radiation with reflectance losses and the second expression accounts for the current contribution from diffuse radiation, again with losses. The parameter I_{sc}^{conc} is the short-circuit current measured under concentration, I_{sc}^{ref} is the short-circuit current measured on a reference module placed at the entrance aperture of the CPC, I_b is the beam radiation, I_d is the diffuse radiation and I_t is the total radiation. The parameter $C_g = 3.6$, is the geometrical concentration ratio of the used CPC. The ratio of the beam radiation to the total and the ratio of the diffuse radiation to the total on a typical blue-sky day are 0.9 and 0.1, respectively [12].

2.3. Flux distribution profile measurements

The flux distribution profile apparatus used in the measurements is shown in Fig. 2. The rotation of the motor rotates the potentiometer which in turn moves the wiper and the attached photo diode in the clockwise direction. A small hole of 1 mm diameter was used to increase the resolution of the photodiode measurements. The flux distribution profile measurements were averaged at four regular intervals along the length of the CPC to minimize errors due to non-linearity of the CPC geometry. The non-uniform illumination was compared for the three reflectors in terms of their local concentration ratios (C_L) from the flux distribution measurements. The local concentration ratio was obtained from the ratio of the flux density reaching the absorber to the flux density intercepted at the entrance aperture of the concentrator.

2.4. Ray-tracing techniques

The ray tracing was performed using a commercial Zemax software [11] and the Matlab programme [13]. If we denote the incident unit vector $\hat{i}$, the normal unit vector $\hat{n}$ and the reflected unit vector $\hat{r}$, we may make a representation of ray-tracing profile for a specular surface as shown in Fig. 3. If the incident ray is known, the reflected ray may be calculated [1] from the standard reflection equation (2).

$$\hat{r} = \hat{i} - 2(\hat{i}.\hat{n})\hat{n} \quad (2)$$

A known number of rays were sent through the aperture of the CPC and monitored the statistics of the fraction of rays that hit the absorber directly, f_0, and the fraction of those that hit the absorber after the first reflection, f_1, and the fraction of those that hit the absorber after the second reflection, f_2, etc. From these statistics, the effective specular reflectance (R_{eff}) for each reflector material was estimated from Eq. (3). Note that Eq. (3) was evaluated only at normal incidence as was the case for Eq. (1).

$$\frac{C_L}{C_g} = f_0 + f_1 R_{eff} + f_2 . R_{eff}^2 + \ldots \quad (3)$$

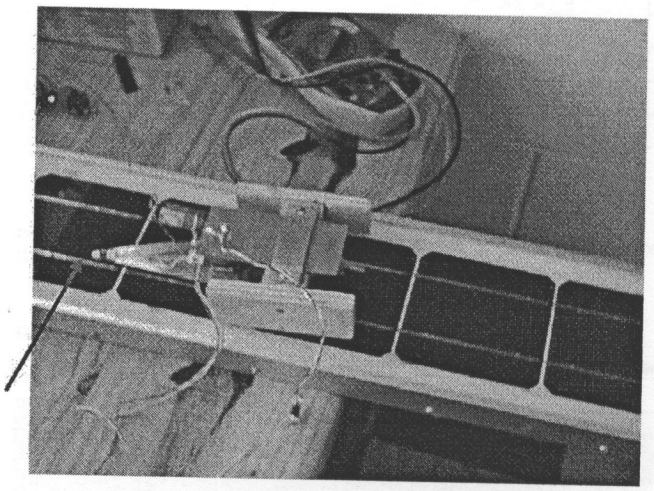

Fig. 2. Flux distribution profile apparatus resting on the 10-cell module string outside the CPC geometry.

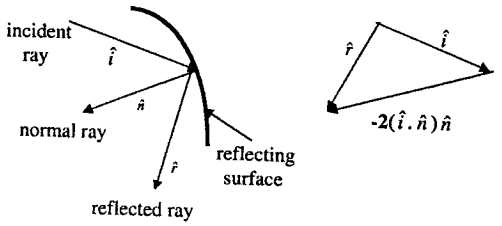

Fig. 3. Vector representation of light reflection for a specular surface (after Welford and Winston, 1978).

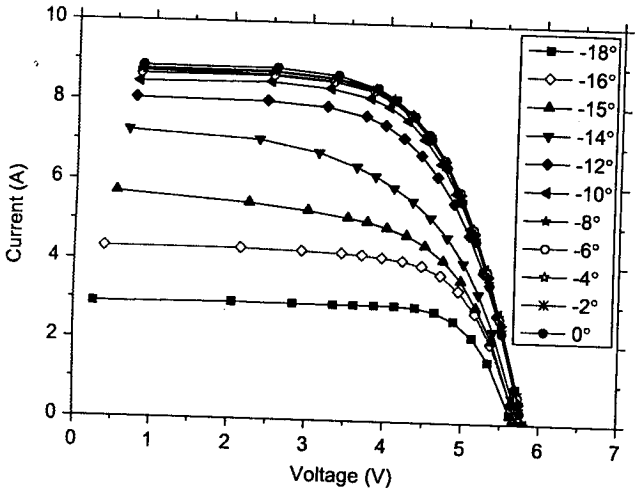

Fig. 4. *I–V* curves for anodized aluminium reflector at different angles of incidence.

3. Results and discussion

3.1. *I–V* characteristic curves

The characteristic current–voltage (*I–V*) curves were obtained at each angle of incidence for each reflector material. However, only the typical *I–V* curve for anodized aluminium which was used as a base reflector is shown in Fig. 4. Only even negative angles of incidence (below normal incidence) are plotted for clarity and an *I–V* curve for an angle of incidence of −15° is included for completeness.

The dependence of the short-circuit current as a function of angle of incidence are shown in Fig. 5 for the three materials. Similarly, the dependence of fill-factor as a function of angle of incidence is shown in Fig. 6 for the three materials. The power dependence of the angle incidence and voltage dependence of the angle of incidence were also evaluated. The increase in the short-circuit current was proportional to the irradiance on the cells as seen in Fig. 5. The short-circuit current curve for anodized material followed the ideal optical behaviour because it was used as the base reflector. The miro and the rolled foil short-circuit current curves show narrower angles of acceptance due to loose binding to the base reflector. The reduction in short-circuit current at angles of incidence less than the acceptance half angle were due to optical imperfections of the reflector.

The fill factor for each material seemed to be fairly constant within ±10° of tilt. The fill factor for the anodized reflector dropped sharply at ±14° (Fig. 6) because all the rays fell on the edge of the cells and hence increased resistive losses (used as base reflector). The increase in fill factor outside these angles of incidence was due to the decrease in current. The fill factors within ±10° of tilt for all the materials are shown in Table 1 column 6. In column 7 of Table 1 we show the estimated effective specular reflectance for each material as calculated from Eq. (1).

3.2. Flux distribution profile results

The simulated and the measured flux distribution results for anodized aluminium reflector are shown in Fig. 7. The two results are in good agreement. However, the curve for the measured values shows a narrower width due to imperfections of the CPC.

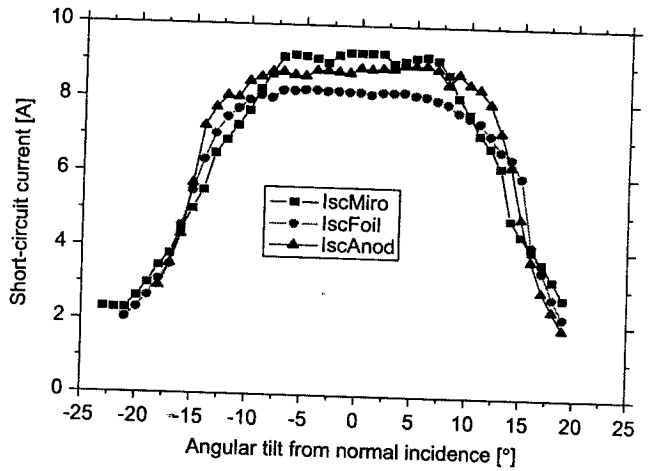

Fig. 5. The angular dependence of short-circuit current for the three different reflectors.

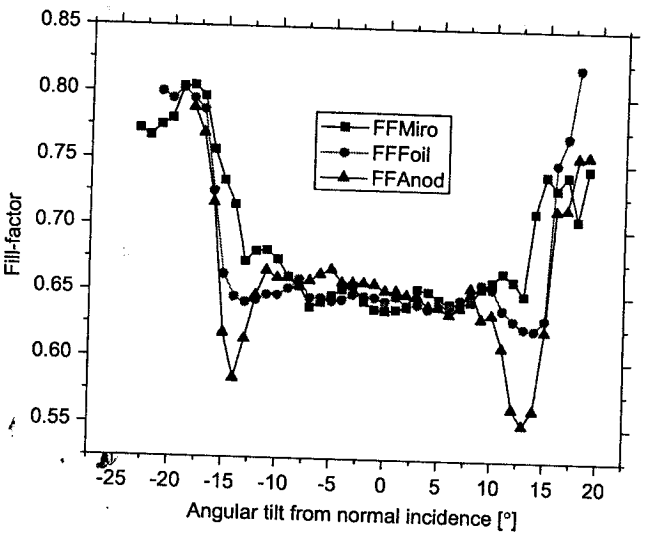

Fig. 6. The dependence of fill factor as a function of the angle of incidence for the three different reflectors.

Table 1
Summary results from short-circuit current measurements for different reflector materials within angular tilt of ±10°

Material	I_{sc} (A)	$I_{sc}/I_{sc\text{-}ref}$	P_m (W)	$P_m/P_{m\text{-}ref}$	FF	R_{eff}
Miro	8.9	2.7	33.4	2.5	0.65	0.74
Foil	8.1	2.4	30.5	2.2	0.65	0.61
Anodized	8.7	2.6	32.9	2.4	0.65	0.69
Reference	3.3	1.0	13.6	1.0	0.72	

The non-identical peaks also confirm the non-ideal geometry of the CPC.

The local concentration ratios (C_L) as a function of position are as shown in Fig. 8. The concentration ratio curves for anodized and miro reflectors are identical because of being highly specular but the width for miro is smaller due to slight change in the shape of the CPC when inserting the miro reflector. The corresponding rolled foil curve was far from ideal because it did not follow the shape of the CPC profile perfectly. The area under the concentration factor-position graph was a measure of the total solar intensity on the module and a summary of the normalized results are shown in Table 2 column 2. It may be observed that the high peaks for anodized and miro in Fig. 8 imply high local heating effects which were rather reduced for diffuse rolled aluminium.

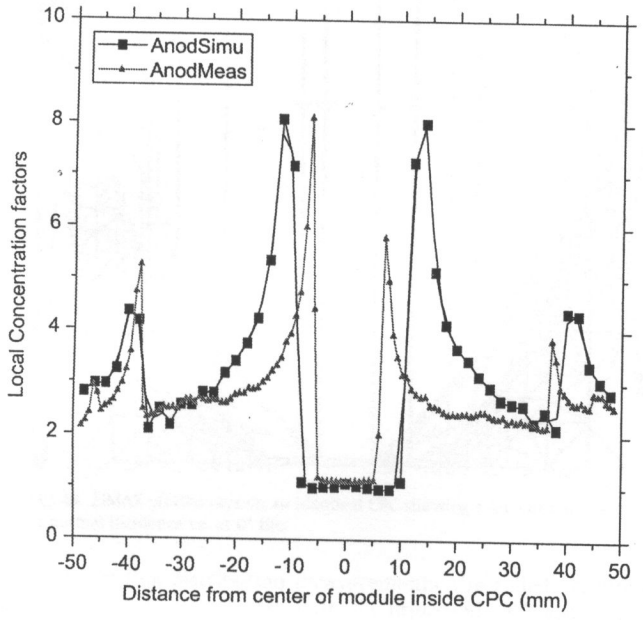

Fig. 7. Comparison of the simulated and measured data for the anodized aluminium reflector used as a base.

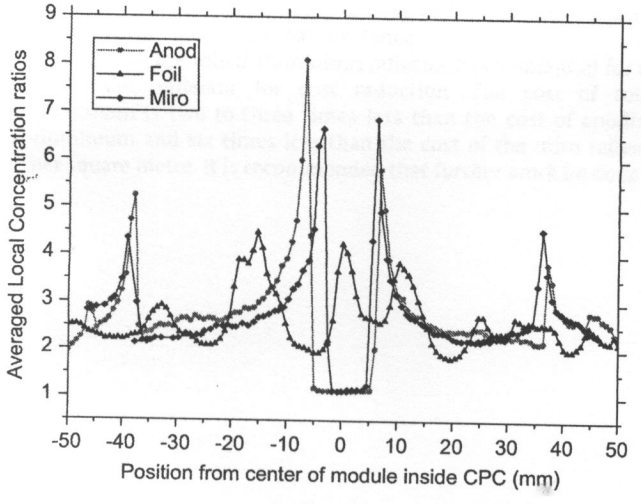

Fig. 8. Averaged local concentration ratios as a function of distance from centre of the module.

3.3. *The ray-tracing results*

Eq. (3) was used to calculate the effective specular reflectance R_{eff} at normal incidence and the results are shown in Table 2, column 3. In Fig. 9, the visual experimental outcome of the ray-traced rays at normal incidence from a simple grating apparatus is shown and in Fig. 10, a corresponding simulated outcome from the ZEMAX software also at normal incidence is shown. Although, few rays are shown in Figs. 9 and 10, more than 100 rays were used in the actual ray-tracing programme to give good statistical parameters in Eq. (3).

4. Conclusions

The CPC element with a geometrical concentration ratio of 3.6 has been analysed with different reflector materials. The short-circuit current increased within a factor of 2.4 and 2.7. The fill factors decreased from 0.72 for the reference module to 0.65 under concentration, giving a percentage decrease of about 10%. The decreased fill factor during concentration was a result of high and non-homogenous irradiance that increased the resistive losses during concentration. The rolled aluminium reflector did not perform as expected in the fill factor improvements although behaved relatively well with the flux distribution measurements.

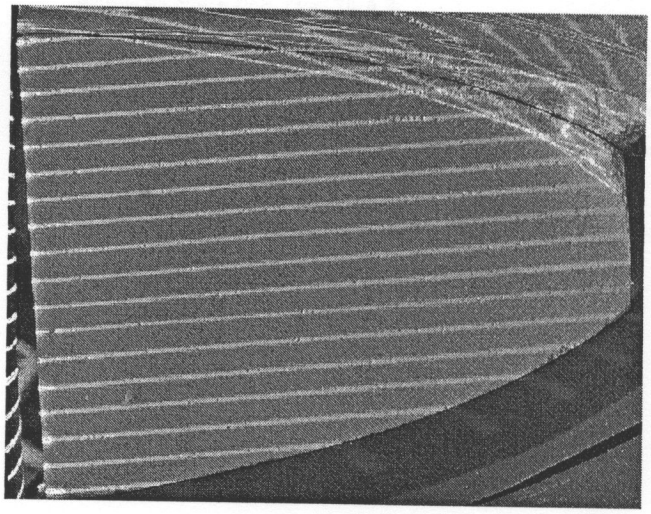

Fig. 9. Simple grating apparatus the rays at normal incidence i.e. at 0° tilt.

Table 2
The local concentration ratios, the effective specular reflectance, and the integrated specular reflectance (column 5) for the three reflector materials at normal incidence

Reflector material	C_L ratio (from flux measurements Fig. 8)	R_{eff} (from flux and ray-tracing equation (3)	R_{eff} (from I–V measurements equation (1)	Integrated specular reflectance
Miro	2.72	0.73	0.74	0.86
Rolled foil	2.59	0.68	0.61	0.55
Anodized aluminium	2.70	0.72	0.69	0.85

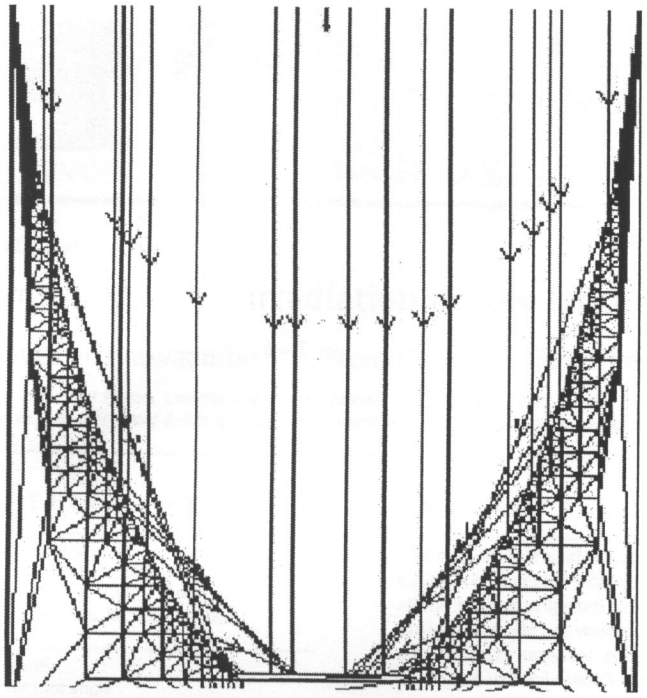

Fig. 10. ZIMAX plotted rays on an identical CPC showing a known number of rays at normal incidence i.e. at 0° tilt.

From the flux distribution measurements, the rolled aluminium could performance better with an improved CPC geometry. A concentrator geometry with a uniform intensity distribution would be desirable since the cell with the lowest irradiance limits the power output from a module.

The effective specular reflectance values from the short-circuit current and those from the ray-tracing techniques were comparable to within 10% at normal incidence.

However, the rolled aluminium reflector has a potential for use as PV–CPC reflector for cost reduction. The cost of rolled aluminium is two to three times less than the cost of anodized aluminium and six times less than the cost of the miro reflector per square metre. It is recommended that further work be done on different groove sizes and different groove orientations in improved geometries. It is expected that reflectors with grooves parallel to the trough would give stronger scattering across the module and better performance in terms of fill factor.

Acknowledgements

The corresponding author wishes to thank the International Science Programme (ISP) of Uppsala University for sponsoring this research work and for facilitating the acquisition of equipment/apparatus for the home laboratory. The Lund University is acknowledged for hosting the corresponding author during his research visit.

References

[1] W.T. Welford, R. Winston, The Optics of Non-Imaging Concentrators; Light and Solar Energy, Academic Press, New York, 1978.
[2] T. Saitoh, K. Yoshioka, Preparation and properties of photovoltaic static concentrators, Renewable Energy 15 (1998) 566.
[3] S. Goma, K. Yoshioka, T. Saitoh, Effect of concentration distribution on cell performance for low-concentrators with a three dimensional lens, Solar Energy Mater. Solar Cells 47 (1997) 339.
[4] A. Luque, G. Sala, J.C. Arboiro, Electric and thermal model for non-uniformly illuminated concentration cells, Solar Energy Mater. Solar Cells 51 (1998) 269.
[5] B. Perers, B. Karlsson, External reflectors for large solar collector arrays, simulation model and experimental results, Solar Energy 51 (5) (1993) 327.
[6] M. Ronnelid, B. Perers, B. Karlsson, Construction and testing of a large-area CPC collector and comparison with a flat-plate collector, Solar Energy 57 (1996) 177.
[7] B. Karlsson, A large bifacial photovoltaic-thermal low concentrating module. 17th PVSEC, Munich, Germany, 2001.
[8] M. Brogren, P. Nostell, B. Karlsson, Optical efficiency of a PV-thermal hybrid CPC module for high latitudes, Solar Energy 69 (6) (2001) 173.
[9] M. Brogren, B. Karlsson, H. Hakansson, Design and modeling of low-concentrating solar energy systems and investigation of irradiation distribution on modules in such systems, in 17th EUPVSEC. Munich, Germany, 2001.
[10] M. Brogren, Optical efficiency of low-concentrating solar energy systems with parabolic reflectors, Ph.D. Thesis from the Faculty of Science and Technology, Uppsala University, 2004. Paper VII, p. 9.
[11] J. Nilsson, Optical design and characterization of solar concentrators for photovoltaics, Division of Energy and Building Design, Department of Architecture and Built Environment, Lund University, Licentiate Thesis, 2005.
[12] M. Brogren, Optical efficiency of low-concentrating solar energy systems with parabolic reflectors, Ph.D. Thesis from the Faculty of Science and Technology, Uppsala University, 2004, p. 109.
[13] E. Part-Enander, A. Sjoberg, B. Melin, P. Isaksson, The MATLAB Handbook, third ed, Addison-Wesley, Longman Ltd., 1996.

Renewable Energy 34 (2009) 1394–1398

Contents lists available at ScienceDirect

Renewable Energy

journal homepage: www.elsevier.com/locate/renene

Data Bank

Projected beam irradiation at low latitudes using Meteonorm database

Sylvester Hatwaambo [a,*,1], Prem C. Jain [a,1], Bengt Perers [b,2], Bjorn Karlsson [b,2]

[a] Department of Physics, University of Zambia, P.O. Box 32379, Lusaka 10101, Zambia
[b] Division of Energy and Building Design, Department of Architecture and Built Environment, Lund University, P.O. Box 118, SE-221 00 Lund, Sweden

ARTICLE INFO

Article history:
Received 2 March 2008
Accepted 5 September 2008
Available online 26 October 2008

Keywords:
Acceptance angle
Projection solar height angle
Meteonorm
TRNSYS

ABSTRACT

The quantitative analysis of beam radiation received on a solar concentrator may be understood by evaluating the projected solar height angle or profile angle along the north–south vertical plane. This means that all the sunrays projected along the north–south vertical plane will be intercepted by a collector provided the projection angle lies within the acceptance angle. The Meteonorm method of calculating solar radiation on any arbitrary oriented surface uses the globally simulated meteorological databases. Meteonorm has become a valuable tool for estimating solar radiation where measured solar radiation data is missing or irregular. In this paper we present the projected beam solar radiation at low latitudes based on the standard Meteonorm calculations. The conclusion is that there is potential in using solar concentrators at these latitudes since the projected beam radiation is more during winter periods than in summer months. This conclusion is in conformity with the design principle of solar collectors for worst case conditions.

1. Introduction

TRNSYS (TRaNsient Systems Simulation) is a simulation program designed to make transient system simulation in which selected input parameters are computed and the output information may be viewed and/or plotted as required. TRNSED is an editor program for TRNSYS version 1.97 developed at the Solar Energy Laboratory – University of Wisconsin, Madison [1]. However, all the calculations in this paper were based on the WINSUN program version 14.2 developed at Lund University [2]. Meteonorm calculations are based on the 10-year averages and give maximum radiation values under clear sky conditions. According to Meteonorm, comparisons of the measured solar radiations for longer periods show a discrepancy of less than 2% for all weather stations but computational models show less inaccuracy than the variation in measured total radiation between one year and the other. The low latitude sites selected south of the equator were Lusaka 15.4° (Zambia), Kasama 10.2° (Zambia), Harare 17.8° (Zimbabwe), Maputo 25.9° (Mozambique) and Nairobi 1.3° (Kenya).

2. The projected solar height concept

The quantitative analysis of the total energy received on a solar collector may be understood from the projected solar radiation on the north–south vertical plane. The sun vector may be projected along the horizontal plane ($\cos\alpha$) or along the north–south vertical plane ($\cos\xi$) as shown in Fig. 1 below. For an east–west axis aligned solar collector, it is the component of the projected solar vector parallel to the north–south vertical plane that will be normal to the stationary concentrator trough and will contribute to the total energy inside the concentrator. Thus, the projected angle of incidence ($90-\theta_p$) defines the amount of solar radiation accepted or rejected by a 2D stationary concentrator [3–5]. The noon projected solar height angle is the projected solar height when the sun is on the local meridian and is evaluated from equation (7). Similarly, the noon projected angle of incidence is the projected angle of incidence when the sun is on the local meridian and equation (8) was used to compute the noon projected angles of incidence.

It has been shown [6–8] that the following expressions hold.

$$\sin\alpha = \sin\phi\sin\delta + \cos\phi\cos\delta\cos\omega \tag{1}$$

$$\cos\alpha\sin\gamma = \cos\delta\sin\omega \tag{2}$$

$$\cos\alpha\cos\gamma = \cos\phi\sin\delta - \sin\phi\cos\delta\cos\omega \tag{3}$$

From Fig. 1 above and using equations (2) and (3), we easily obtain

$$\tan\theta_p = \frac{\tan\alpha}{\cos\gamma} \tag{4}$$

The projected angle of incidence ($90-\theta_p$) defines the amount of the solar radiation accepted or rejected by a 2D stationary concentrator and may be expressed as

* Corresponding author. Tel./fax: +260 211 293343.
E-mail addresses: shatwaam@unza.zm, shatwamb@gmail.com (S. Hatwaambo).
[1] Tel.: +260 211 293343; fax: +260 211 253952.
[2] Tel.: +46 046 222 72 61; fax: +46 046 222 47 19.

0960-1481/$ – see front matter © 2008 Elsevier Ltd. All rights reserved.
doi:10.1016/j.renene.2008.09.011

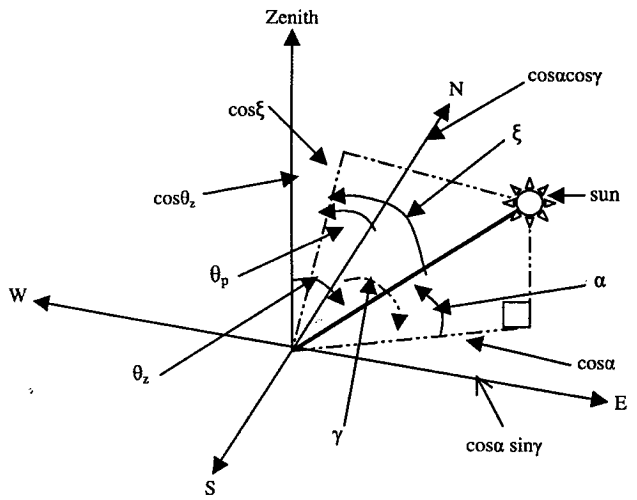

Fig. 1. Relative angles of the projected sunray vector on the horizontal plane and on the north–south vertical plane.

$$\tan\theta_i = \frac{\cos\gamma}{\tan\alpha} \tag{5}$$

It may also be shown from Fig. 1 that the projected component of the beam ray vector along the north–south vertical plane is $H_b \cos\varepsilon$, where H_b is the magnitude of the beam ray vector from the sun and that

$$\cos\varepsilon = \frac{\cos\alpha\cos\gamma}{\cos\theta_p} \tag{6}$$

3. Results

3.1. Evaluation of the standard solar heights

The standard solar height or solar elevations angles as a function of solar time for specific date(s) of the month [3] were obtained from equation (1) for Lusaka and are shown in Fig. 2 below.

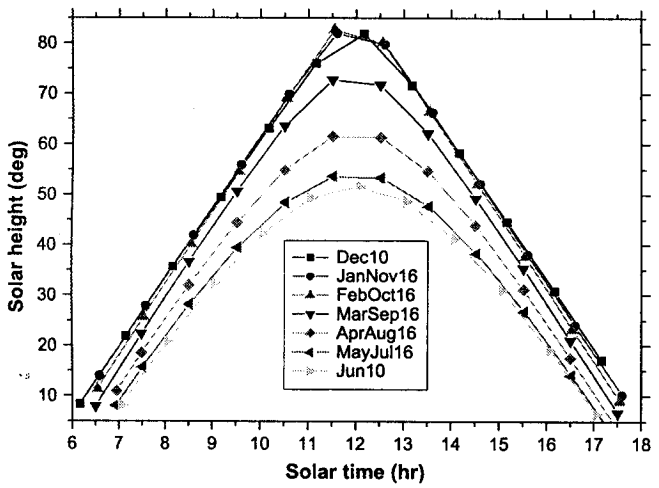

Fig. 2. Standard solar height angles as a function of solar time for Lusaka.

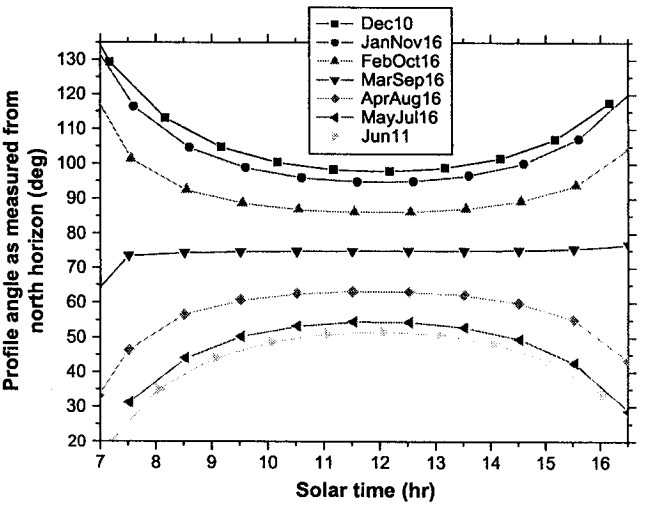

Fig. 3. Profile angles for Lusaka as a function of solar time measured from north horizon.

3.2. Evaluation of the projected solar height angles and the projected angles of incidence

The daily projected solar height angles as a function of solar time were evaluated for Lusaka site from equation (4) and results are shown in Fig. 3. The solar noon profile angles or the noon projected solar height angles were computed [9] from equation (7) and were in agreement with values obtained from equation (4). However, equation (7) could not be extrapolated for other times of the day.

$$\theta_{pn} = 90 + \phi - \delta \tag{7}$$

Similarly, the projected angles of incidence were calculated from equation (5) and results shown in Fig. 4. The noon projected angles of incidence in the southern hemisphere were computed [9] from equation (8) and were in good agreement with those computed from equation (5). The only limitation to equation (8) was that it could not be used for other times of the day. Note that the negative angles of incidence imply that the angles are located north of the local latitude and positive angles of incidence means south of the

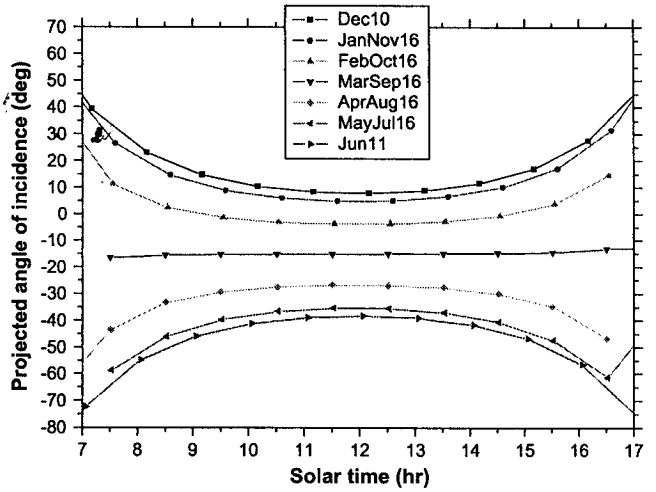

Fig. 4. Daily projected angles of incidence for Lusaka as a function of solar time.

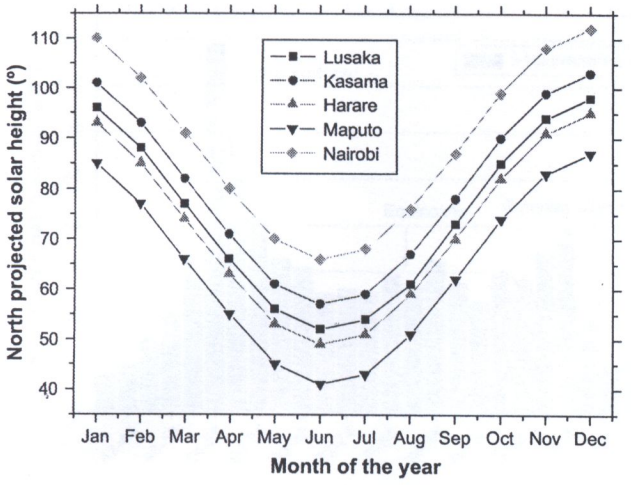

Fig. 5. Monthly noon projected solar height angles for the five sites.

local latitude. In Fig. 5, we show the noon profile angles for all the selected sites for each month [3]. These were calculated from equation (7).

$$\theta_{in} = -\phi + \delta \tag{8}$$

3.3. Evaluation of the standard solar irradiances for the five sites

The Meteonorm database version 5.1 and the TRNSED program obtained from Lund University, Sweden, were used to compute the standard (not projected) annual solar radiation collected on a latitude tilt of each site. The results are shown in Fig. 6 below. Maputo and Nairobi show relatively low beam irradiance probably because of the ocean influence. The global irradiances were equally low for Maputo and Nairobi. However, the diffuse irradiances were fairly the same for all the sites.

In Fig. 7, we show a comparison of the monthly beam solar radiation for the five sites. The monthly beam irradiances were high in the months of June, July, August and September for Lusaka, Kasama and Harare. The monthly beam irradiances were high in December, January, February and March for Nairobi. The monthly beam irradiances for Maputo seems to be evenly distributed except

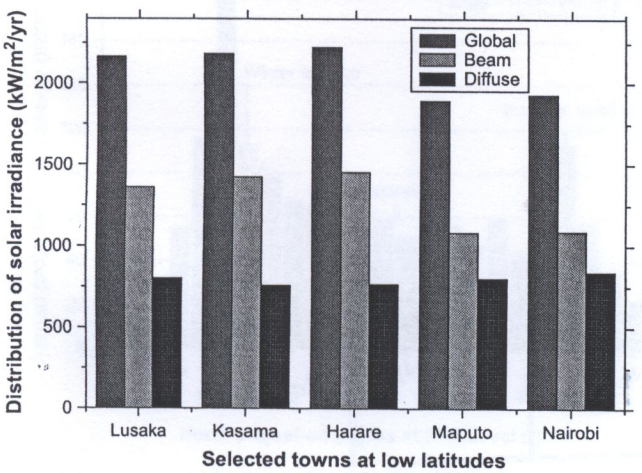

Fig. 6. The amount of solar irradiances at latitude tilt for the selected sites.

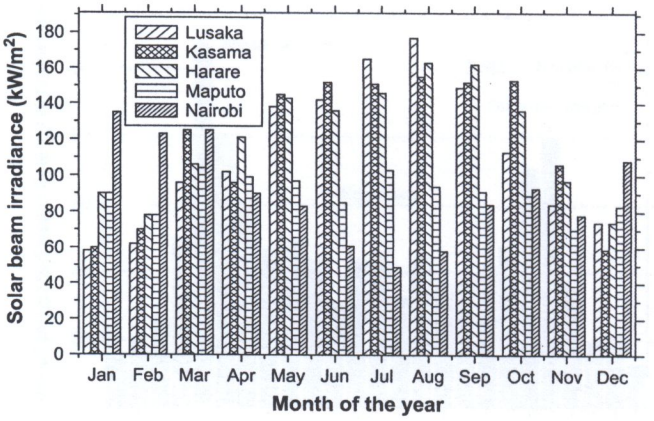

Fig. 7. Monthly average beam irradiances for the five sites.

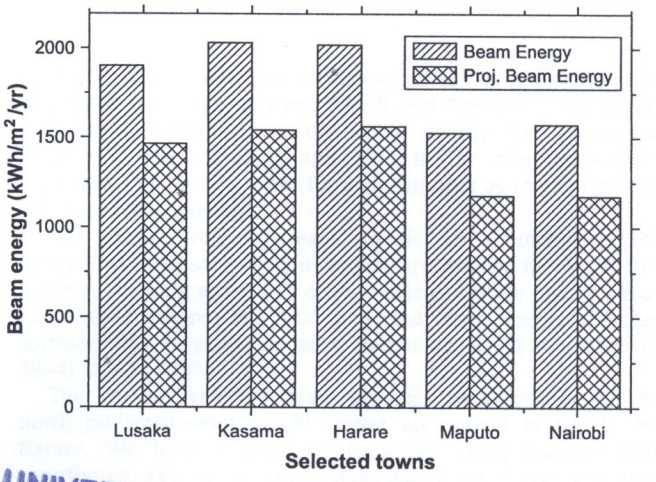

Fig. 8. The comparison of beam energy and the projected beam energy for five sites.

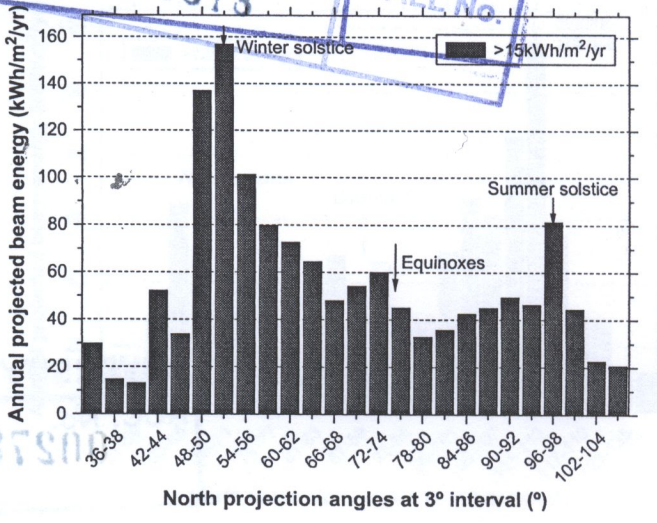

Fig. 9. Annual projected beam energy as a function of the projected solar height angles for Lusaka.

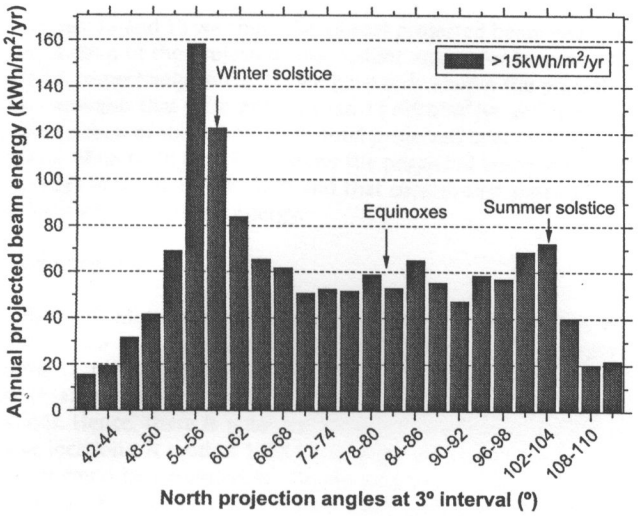

Fig. 10. Annual projected beam energy as a function of the projected solar height angles for Kasama.

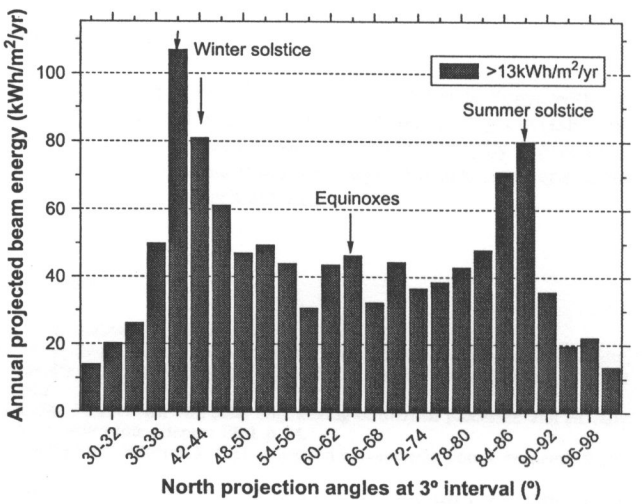

Fig. 12. Annual projected beam energy as a function of the projected solar height angles for Maputo.

for the months of June, July, August and September which show higher beam irradiances.

3.4. Comparison of the standard beam energy and the projected beam energy for the five locations

The standard beam energy normal to the surface and the projected beam energy in the north–south vertical plane are compared in Fig. 8 below. The projected beam energy was evaluated using equation (6).

3.5. Evaluation of the projected beam energy as a function of the projected solar height angles

The annual projected beam energy as a function of the north projected solar height angle was calculated from equations (4) and (6) using the WINSUN program. The results are shown in Fig. 9 for Lusaka. Only the projected beam energies that contributed more than 94% of the total beam energy were plotted in Fig. 9 and that corresponded to the projected solar heights in the range between 33–35 and 105–107°. This means that the contributions of the beam energy 33° below the horizon in the mornings and 107° in the afternoons were neglected. This makes sense for concentrators as the sun is very low above the horizon.

The annual projected beam energies as a function of the north projected solar height angles are shown in Fig. 10 for Kasama. We only show 93% of the projected beam energies that contributed towards the total projected beam energy and that corresponded to projected solar height angles in the range of 39–41 to 111–113°.

The annual projected beam energies as a function of the north projected solar height angles are shown in Fig. 11 for Harare. We have shown the projected beam energies that contributed 93% of the total projected beam energy and that corresponded to projected solar height angles in the range of 33–35 to 102–104°.

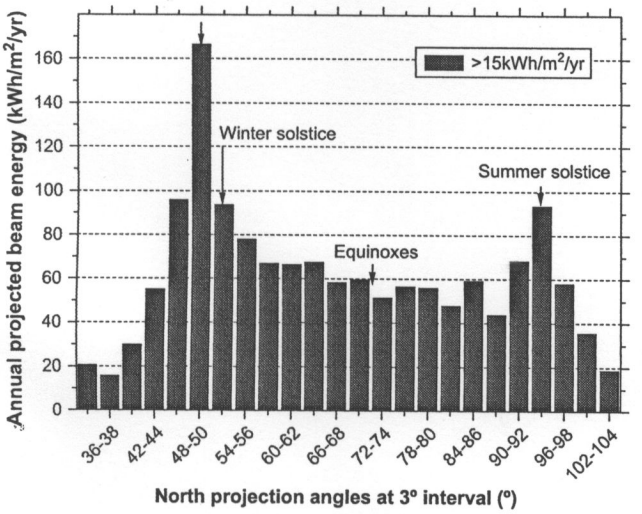

Fig. 11. Annual projected beam energy as a function of the projected solar height angles for Harare.

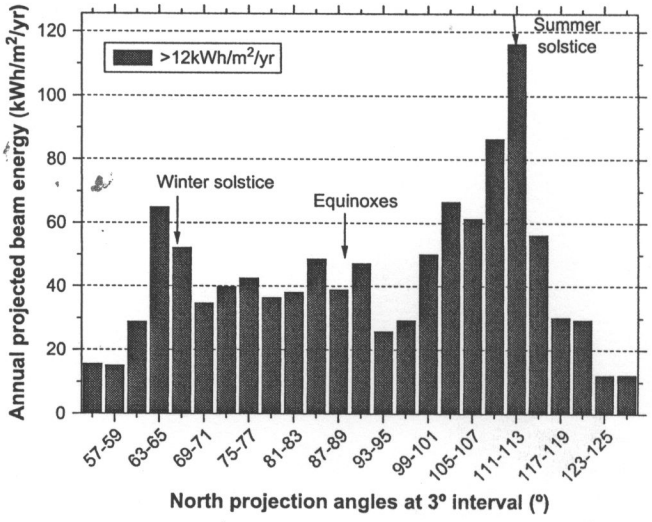

Fig. 13. Annual projected beam energy as a function of the projected solar height angles for Nairobi.

In Figs. 12 and 13 we show the annual projected beam energies as a function of the projected solar height angles for Maputo and Nairobi, respectively. In Fig. 12, we have only shown the projected beam energies that were greater than 13 kWh/m^2/yr and that had a contribution of about 94% of the total projected beam energy per year for Maputo. In Fig. 13, we show the projected beam energy in the range of 54–56 to 126–128° and that contributed about 92% of the total projected beam energy.

4. Conclusions

From the Meteonorm databases and WINSUN calculations, we have shown that the north projected beam energies are more during winter periods for all the selected sites except for Nairobi which shows more of the projected beam energy in summer periods. Hence, there is potential for using solar concentrators at these locations. A total of 1464 kWh/m^2/yr north projected beam energy could be harvested for Lusaka ($\phi = 15°$ south), 1542 kWh/m^2/yr for Kasama ($\phi = 10°$ south), 1563 kWh/m^2/yr for Harare ($\phi = 18°$ south), 1176 kWh/m^2/yr for Maputo ($\phi = 26°$ south) and 1173 for Nairobi ($\phi = 1.3°$ south).

Since the declination of the sun is defined at solar noon, the noon projection solar height angles in equation (7) and so the noon projected angles of incidence in equation (8) may not be extrapolated to off noon values.

Acknowledgements

Most of this work was done at Moi University in Kenya with the financial assistance of the International Science Program (ISP). The warm hospitality received at Moi University is highly appreciated. The University of Zambia is acknowledged for granting permission to visit Kenya for research activities.

References

[1] <http://sel.me.wisc.edu/trnsys>.
[2] Perers Bengt, Karlsson Bjorn. Energy and building design. Lund University, Faculty of Engineering (LTH); 2007. WINSUN Based on TRNSYS/TRNSED/PRESIM 14.2.
[3] Duffie JA, Beckman WA. Solar engineering of thermal processes. 2nd ed. New York: Wiley Interscience; 1991. p. 14.
[4] Welford WT, Winston R. High collection non-imaging optics. Academic Press; 1989.
[5] Rönnelid M, Karlsson B. Irradiation distribution diagram and their use for estimating collectable energy. Solar Energy 1997;61(3):191–201.
[6] Horizontal coordinate system – Wikipedia, the free encyclopia. Available from: <http://en.wikipedia.org/wiki/Horizontal_coordinate_system>.
[7] <http://www.usc.edu/dept/architecture/mbs/tools/vrsolar/help/solar_concepts.html>.
[8] Muhammad Iqbal. An introduction to solar radiation. The University of British Columbia; Academic Press; 1983. p. 15.
[9] Weinham SR, Green MA, Watt ME. Applied photovoltaics. Centre for Photovoltaics Devices and Systems; 1994. p. 11.